










## RESEARCH ARTICLE

# The intricacies of identifying equatorial waves

Peter Knippertz<sup>1</sup>  | Maria Gehne<sup>2</sup>  | George N. Kiladis<sup>2</sup> | Kazuyoshi Kikuchi<sup>3</sup> |  
Athul Rasheeda Satheesh<sup>1</sup> | Paul E. Roundy<sup>4</sup>  | Gui-Ying Yang<sup>5</sup>  |  
Nedjeljka Žagar<sup>6</sup>  | Juliana Dias<sup>2</sup> | Andreas H. Fink<sup>1</sup>  | John Methven<sup>7</sup>  |  
Andreas Schlueter<sup>8</sup>  | Frank Sielmann<sup>6</sup> | Matthew C. Wheeler<sup>9</sup> 

<sup>1</sup>Institute of Meteorology and Climate Research, Karlsruhe Institute of Technology, Karlsruhe, Germany

<sup>2</sup>NOAA Physical Sciences Laboratory, Boulder, Colorado

<sup>3</sup>International Pacific Research Center, School of Ocean and Earth Science and Technology, University of Hawaii at Manoa, Honolulu, Hawaii

<sup>4</sup>Department of Atmospheric and Environmental Sciences, State University of New York at Albany, Albany, New York

<sup>5</sup>National Centre for Atmospheric Science and University of Reading, Reading, UK

<sup>6</sup>Meteorological Institute, Universität Hamburg, Hamburg, Germany

<sup>7</sup>Department of Meteorology, University of Reading, Reading, UK

<sup>8</sup>Department of Computer Science, Stanford University, Stanford, California

<sup>9</sup>Bureau of Meteorology, Melbourne, Victoria, Australia

**Correspondence**

Peter Knippertz, Institute of Meteorology and Climate Research, Karlsruhe Institute of Technology, 76131 Karlsruhe, Germany. Email: [peter.knippertz@kit.edu](mailto:peter.knippertz@kit.edu)

**Funding information**

Deutsche Forschungsgemeinschaft, Grant/Award Number: SFB/TRR165; Schmidt Science Foundation, Grant/Award Number: Fellowship for Andreas Schlueter

**Abstract**

Equatorial waves (EWs) are synoptic- to planetary-scale propagating disturbances at low latitudes with periods from a few days to several weeks. Here, this term includes Kelvin waves, equatorial Rossby waves, mixed Rossby–gravity waves, and inertio-gravity waves, which are well described by linear wave theory, but it also other tropical disturbances such as easterly waves and the intraseasonal Madden–Julian Oscillation with more complex dynamics. EWs can couple with deep convection, leading to a substantial modulation of clouds and rainfall. EWs are amongst the dynamic features of the troposphere with the longest intrinsic predictability, and models are beginning to forecast them with an exploitable level of skill. Most of the methods developed to identify and objectively isolate EWs in observations and model fields rely on (or at least refer to) the adiabatic, frictionless linearized primitive equations on the sphere or the shallow-water system on the equatorial  $\beta$ -plane. Common ingredients to these methods are zonal wave-number–frequency filtering (Fourier or wavelet) and/or projections onto predefined empirical or theoretical dynamical patterns. This paper gives an overview of six different methods to isolate EWs and their structures, discusses the underlying assumptions, evaluates the applicability to different problems, and provides a systematic comparison based on a case study (February 20–May 20, 2009) and a climatological analysis (2001–2018). In addition, the influence of different input fields (e.g., winds, geopotential, outgoing long-wave radiation, rainfall) is investigated. Based on the results, we generally recommend employing a combination of wave-number–frequency filtering and spatial-projection methods (and of different input fields) to check for robustness of the identified signal. In cases of disagreement, one needs to carefully investigate which assumptions made for the individual methods are most probably not fulfilled. This will help in choosing an approach optimally suited to a given problem at hand and avoid misinterpretation of the results.

**KEYWORDS**

convection, equatorial Rossby waves, Kelvin waves, mixed Rossby–gravity waves, spatial projection, time–space filtering, tropical rainfall

German Research Foundation, SFB/TRR 165; Schmidt Science Foundation, Fellowship

This is an open access article under the terms of the Creative Commons Attribution License, which permits use, distribution and reproduction in any medium, provided the original work is properly cited.

© 2022 The Authors. *Quarterly Journal of the Royal Meteorological Society* published by John Wiley & Sons Ltd on behalf of the Royal Meteorological Society.

## 1 | INTRODUCTION

Geophysical fluids on a rotating sphere develop propagating planetary-scale disturbances trapped at the Equator that are usually referred to as “equatorial waves” (EWs). For example, EWs play a role in the atmospheric dynamics of Venus, Jupiter, and Saturn (Del Genio and Rossow, 1990; Yamazaki *et al.*, 2005; Sugimoto *et al.*, 2014) and have been documented for the Earth’s oceans (Wakata, 2007; Shinoda *et al.*, 2009; Farrar and Durland, 2012), where they are instrumental in the phase reversal of El Niño events (e.g., Yu and McPhaden, 1999). In the Earth’s tropical troposphere, EWs can couple with deep convection, thereby shaping large-scale variations of clouds and rainfall (Takayabu, 1994a; Wheeler and Kiladis, 1999). These EWs can propagate into the middle atmosphere and help force the Quasi-Biennial Oscillation (Lindzen and Holton, 1968; Plumb and McEwan, 1978; Baldwin *et al.*, 2001; Pahlavan *et al.*, 2021). The periodicity and coherent phase propagation of EWs contribute to longer intrinsic predictability at planetary scales in the Tropics than at higher latitudes (Žagar *et al.*, 2016; Wheeler *et al.*, 2017; Judt, 2018; 2020; Li and Stechmann, 2020).

Improving the representation of EWs in numerical weather prediction (NWP) and/or statistical models is key for advancing forecasting in the Tropics (Roundy, 2012c; Žagar, 2017; Dias *et al.*, 2018; Bengtsson *et al.*, 2019), where current operational predictions of precipitation on a daily time-scale are barely better than a climatological forecast over many regions (Haiden *et al.*, 2012; Vogel *et al.*, 2020). Improvements in NWP in the Tropics can come from both advancements in model initialization and model development. More accurate initial states (analyses) are produced using new observations and improved data assimilation schemes (e.g., Žagar, 2004; Zaplotnik *et al.*, 2018). Current methodologies do not account sufficiently for EWs, which, together with sparse wind observations and deficient moist dynamics, lead to uncertainties in tropical analysis datasets (Podglajen *et al.*, 2014; Žagar *et al.*, 2016). Initial-state errors also negatively impact climatological studies based on reanalysis data. Similarly, improvements to NWP models in the Tropics can result in better tropical forecasts and can also, in turn, improve extratropical forecasts (Jung *et al.*, 2010; Dias *et al.*, 2021). The model development issue especially pertains to the representation of moist convection (e.g., Bengtsson *et al.*, 2019; Judt and Rios-Berrios, 2021), but also numerical aspects such as the horizontal and vertical resolution. It is expected that improvements in the Tropics will help advance subseasonal to seasonal predictions worldwide (e.g., Vitart *et al.*, 2012, Dias and Kiladis, 2019).

To isolate EWs objectively, a number of different methods have been proposed that aim to observe

and understand their evolution in nature, assess their behaviour in models, or identify them for operational forecasting purposes. The main approaches employ space–time filtering in Fourier (or wavelet) space and/or spatial projection onto theoretical or empirical patterns (two- or three-dimensional). All methods require a number of complex parameter choices, and their application to the tropical troposphere is challenging owing to the high levels of background noise from convection, zonal and meridional inhomogeneities, and interactions with the extratropics.

This paper will review the different methodological approaches to isolate EWs and their theoretical underpinnings. We will for the first time systematically compare results from the most common methods of EW identification and different input datasets. We will concentrate on EWs in the Earth’s atmosphere, but most of the methods presented can, in principle, be applied to the ocean or other planetary atmospheres, too. By bringing differences between the different methods to light in a systematic way, we aim to better understand the “true” nature of EWs and to sharpen terminology. This way, we hope to create more awareness of common pitfalls and potential misuse or misinterpretation of EW identification and to guide other researchers to choose the optimal data and method for their problem at hand.

The tropical atmosphere comprises a spectacular range of weather features, ranging from short-lived individual thunderstorms ( $\sim 10$  km) to different types of synoptic ( $\sim 1,000$  km) to planetary-scale waves ( $\sim 10,000$  km). Matsuno (1966) developed a theoretical framework to understand and describe atmospheric EWs that is still widely used today. Using the rotating, shallow-water equations on the equatorial  $\beta$ -plane, he identified different types of zonally (and vertically) propagating, free solutions with different dispersion behaviour and horizontal structures: fast eastward-moving Kelvin waves (KWs), slow westward-moving equatorial Rossby waves (ERs), and westward-moving mixed Rossby–gravity waves (MRGs, sometimes referred to as WMRGs), as well as westward- and eastward-moving inertio-gravity waves (WIGs and EIGs). An extension of analytical wave solutions to the sphere (Longuet-Higgins, 1968) and to the vertical dimension using the primitive equations linearized about a resting atmosphere (Kasahara, 1976; 1980) isolates the global three-dimensional normal modes. An outline of the underlying theory will be provided in Section 2.

Studies using satellite imagery have demonstrated an apparent coupling of EWs with tropical convection (Takayabu, 1994a; 1994b; Wheeler and Kiladis, 1999), mediated predominantly through a modulation of divergence. This has led to a distinction between “convectively coupled EWs” (CCEWs; Wheeler and Kiladis, 1999;



Kiladis *et al.*, 2009) and uncoupled “dry” waves. In addition, a number of (not necessarily wave-like) coherent propagating phenomena have been identified that do not link directly to the linear theory outlined thus far. Synoptic-scale troughs that move westward within the trade winds have often been subsumed under the term “tropical disturbances” (TDs), which includes tropical cyclones, Pacific Easterly Waves (Serra *et al.*, 2008), and African Easterly Waves (Kiladis *et al.*, 2006), the latter growing at least partly from baroclinic–barotropic instability (Burpee, 1972; Hall *et al.*, 2006). Arguably the most prominent wave-like tropical phenomenon is the planetary-scale sub-seasonal Madden–Julian Oscillation (MJO) that shows diverse propagation characteristics in different parts of the Tropics (Madden and Julian, 1972; Zhang, 2013; Zhang *et al.*, 2020). Given the often unclear boundaries between different wave types, various levels of coupling and interactions with moist convection, as well as multiple hybrid forms, we here use the term EWs broadly for all coherent, primarily zonally propagating phenomena on synoptic to planetary scales with activity maxima in the equatorial belt (i.e., including the MJO and TDs). Consequently, we will use the term EWs going forward and make the distinction with CCEWs only where appropriate.

The methods to isolate EWs from observational and model datasets typically employ filtering using Fourier series in time and in the zonal direction, and/or a projection onto theoretical or empirical spatial patterns. The first method to separate TDs into progressive and retrogressive waves by space Fourier and time cross-spectral analyses was developed as early as the 1970s (Hayashi, 1971; 1981). Takayabu (1994a; 1994b) applied a fast Fourier transform (FFT) to satellite infrared (IR) data—used as a proxy for tropical convection—to isolate CCEWs over the Indian Ocean and West Pacific. Wheeler and Kiladis (1999) extended this approach to a longer, global dataset of outgoing long-wave radiation (OLR) with higher time resolution. These studies found an overall “red” energy spectrum; that is, power increasing towards long zonal wavelengths and wave periods. Since theory predicts that EWs possess structures that are either symmetric or antisymmetric about the Equator, equal and opposite latitudinal weighting is often used to distinguish them. This simple pattern projection allows, for example, the separation of lowest meridional mode EIGs, which are antisymmetric in divergence, from symmetric KWs despite similar propagation characteristics. As upper-level divergence occurs above regions of large-scale ascent associated with deep convection and high clouds, divergence has a signature in OLR. OLR spectra created using FFT filtering show distinct peaks above the red background, some of which are consistent with Matsuno’s EW solutions (see Section 2 for details). Wheeler and Kiladis (1999) defined relatively

narrow filter windows around these peaks in the zonal wave number  $k$  and frequency  $\omega$  domains to isolate the different EW types. Recently, Žagar *et al.* (2022) demonstrated specifically for the KW that the results of the Wheeler and Kiladis (1999) approach are dominated by the wave phases (and not the amplitudes).

Though the Wheeler and Kiladis (1999) approach has been used in a multitude of studies over the last 20 years—see also Kiladis *et al.* (2009) and references therein—two important modifications are worthy of note here. The first is to replace the FFT by a wavelet transform, allowing a localization in longitude (Wong, 2009; Kikuchi and Wang, 2010; Dias and Kiladis, 2014; Kikuchi *et al.*, 2018; Roundy, 2018). This approach can be applied to non-global data or to reveal regional and temporal differences in wave behaviour. The second is to replace the latitudinal averaging by a projection of horizontal fields onto parabolic cylinder functions (PCFs), the meridional basis of Matsuno’s EW solution, before filtering in time and zonal direction (Yang *et al.*, 2003; Gehne and Kleeman, 2012; Li and Stechmann, 2020). This allows the isolation of higher-order meridional modes, although typically only a few PCFs are needed to explain the bulk of observed variability.

Since 2000, two- and three-dimensional projection of gridded data onto analytical structure functions has been increasingly employed to isolate EWs (Yang *et al.*, 2003; Žagar *et al.*, 2009b; Castanheira and Marques, 2015; Blaauw and Žagar, 2018). In the three-dimensional case, wind and geopotential height data on pressure (Castanheira and Marques, 2015) or terrain-following model levels (Žagar *et al.*, 2015) are projected onto the full global three-dimensional normal modes (obtained by linearization about a stably stratified, resting atmosphere). This approach can be reduced to using a  $\beta$ -plane approximation and only a limited number of vertical modes, as in Ogrosky and Stechmann (2015; 2016). The spatial projection onto theoretical EW solutions has a long tradition in the research of the global atmospheric response to forcing such as tropical heating perturbations (Gill, 1982; Kasahara, 1984; Kosovelj *et al.*, 2019) and was the basis of efforts to formulate data assimilation systems in the Tropics (Parrish, 1988; Daley, 1993; Žagar *et al.*, 2004; 2005a).

The analytic solution for wave-like disturbances to a resting atmosphere is separable into a vertical structure function and a horizontal solution, which is the same as the solution of the shallow-water equations of Matsuno (1966). The separation constant can be expressed in terms of the “equivalent depth”  $D$  of the wave motions (although it does not represent the geometric layer depth). In the two-dimensional spatial projection methods,  $D$  is chosen empirically and determines the structure of the horizontal basis functions used for projection (Yang *et al.*, 2003).

This projection is done independently at each vertical level and time, and no assumptions are made about vertical or temporal coherence. If such coherence exists, then it is a property of the data, not the method. The individual wave modes identified by spatial projection of wind and geopotential data using the two- and three-dimensional methods outlined herein can be related to other variables, like OLR, through regression or cross-spectral analysis (e.g., Yang *et al.*, 2007c; Marques and Castanheira, 2018). Moreover, Roundy *et al.* (2009) and Roundy (2012c) developed a two-dimensional projection method using time-extended empirical orthogonal function (EEOF) patterns derived from climatological OLR data. This approach can be applied in real time once the patterns are available.

The methods described thus far have their particular strengths and weaknesses, emphasize certain characteristics of EWs, and can be more or less useful for certain applications, but a systematic comparison is lacking. For example, some methods are suitable for real-time monitoring and predictions, whereas others are designed to identify the statistical behaviour of EWs. A fundamental challenge faced by all methods is to isolate a coherent signal (the EW) from the background noise of the tropical atmosphere (unrelated convection or circulation features). As the power spectra of convective proxies such as OLR are dominated by red noise, some authors have normalized them by a background obtained from smoothing or an autoregressive process in order to bring out spectral peaks potentially related to CCEWs (e.g., Wheeler and Kiladis, 1999; Gehne and Kleeman, 2012; Marques and Castanheira, 2018). This procedure emphasizes regions in  $k$ - $\omega$  space with large gradients, whereas “flat” areas will be removed, although these can still contain signals that structurally resemble CCEWs (Roundy, 2012a; 2012b, 2020). As the computation of wave signals is ultimately done based on full fields or anomalies from a seasonal cycle (without any account of a background), the results will always contain contributions from both noise and signal by construction. This motivated Wheeler and Kiladis (1999) and others to focus on relatively small filter windows in  $k$ - $\omega$  space aligned along spectral peaks and (with the exception of MJO and TDs) theoretical dispersion curves. Other authors have opted to include broader areas of  $k$ - $\omega$  space, which they then analyse through projection onto PCFs (Yang *et al.*, 2003) or EEOFs (Roundy, 2012c), or through linear regression with other meteorological fields (Roundy, 2020). The size of the  $k$ - $\omega$  domain investigated is closely related to how one wants to account for a number of effects disregarded in classical linear wave theory, such as the following.

- **Static stability and vertical structure:** In linear wave theory, horizontal dispersion depends on  $D$ , which in

turn depends on vertical stability and vertical mode (see Section 2). For a fluid with constant static stability and a rigid lid, one would obtain sinusoidal vertical structure functions—for example, see Wheeler and Nguyen (2015). Stability variations with height and asymmetries between heating regions (usually in the troposphere) and (mostly radiative) cooling regions (stratosphere, upper troposphere for shallow convection) will lead to a spread of signal across several vertical modes (and thus in  $D$ ) and horizontal dispersion behaviour. Coupling with convection (i.e., CCEWs) will decrease stability, slow down propagation, and thus effectively act so as to reduce  $D$  (Dias *et al.*, 2013a). For instance, spectral peaks associated with tropical convection are aligned with smaller  $D$  compared with the expected EW behaviour in a dry troposphere. Such considerations motivated Wheeler and Kiladis (1999) to construct filter windows along dispersion curves for  $D$  from 8 to 90 m.

- **Doppler shifts:** Linear EW theory assumes a resting basic state, but the real tropical atmosphere typically has a strong background zonal flow that varies longitudinally and particularly affects low-frequency modes (Zhang and Webster, 1989; Webster, 2020). The effects of a uniform background flow can be anticipated theoretically, simply resulting in a Doppler shift of the waves without changing their structure. For example, an easterly basic state, as typical for the Indian Ocean, reduces the frequency of EIGs with  $n = 0$ —referred to as eastward MRGs in Yang *et al.* (2003)—shifting them into a  $k$ - $\omega$  region typical of KWs in a resting state. Westerly ambient flow can even advect the slow ER to become eastward moving relative to the Earth’s surface, whereas westward-moving MRGs slow down to speeds typical for ERs in a resting state. Such Doppler effects are readily identified if EW identification is done for different longitudinal sections (Dias and Kiladis, 2014). The propagation of a wave signal from one zonal wind regime into another can lead to a change in wave speed, which could be misinterpreted as non-coherent wave behaviour. An example of this is the slowdown of fast KWs over the Indian Ocean arriving from the Western Hemisphere (Roundy, 2020). Zonal asymmetry in the background zonal wind can also result in variation in the group velocity of EWs and wave accumulation in particular longitude sectors (Hoskins and Yang, 2016).
- **Vertical and meridional wind shear:** Meridional and vertical shear in the zonal flow (as, for example, related to the Walker cell over the equatorial Pacific Ocean) can have profound effects on the structure, propagation, and stability of EWs (Boyd, 1978; Kasahara, 1980; Wang and Xie, 1996; Serra *et al.*, 2008; Dias and Kiladis, 2014). Theoretical approaches have tried to account for changes in structure and evolution

associated with weak shear (e.g., Andrews and McIntyre, 1976), but a complete theory of the effects of shear on the EW properties has not yet been derived. Boyd (1978) argued that KWs are practically unaffected by vertical shear, in contrast to ERs and WIGs for example (Wang and Xie, 1996; Dias and Kiladis, 2014). In the aquaplanet simulations of Peatman *et al.* (2018) the negative vertical shear in the equatorial, zonally averaged zonal flow results in a prominent westwards vertical tilt of the dominant KWs (communication by the authors, not shown in that paper). Vertical shear might also explain why inertio-gravity waves tend to propagate to the west rather than to the east (Stechmann and Majda, 2009; Tulich and Kiladis, 2012). Changes in background zonal wind with latitude, especially on subtropical flanks, will create tilted wave structures (Andrews and McIntyre, 1976). This distortion shifts power towards higher  $k$ , particularly for relatively small-scale features (Zhang and Webster, 1989; Ferguson *et al.*, 2009; Webster, 2020). In extreme cases, this may even lead to EW instability (Han and Khouider, 2010). The EW diagnostic methods that use projection of data onto orthogonal basis functions (two- or three-dimensional) obtained from theory on a resting atmosphere can only determine a posteriori whether or not the projections provide a compact representation of EW dynamics in a non-resting state. For three-dimensional methods, Kasahara (1980) showed that the analytical structure of the large-scale horizontal eigensolutions of the linearized primitive equations on the sphere is not significantly affected by the latitude-dependent background zonal flow.

- **Non-sinusoidal zonal structure:** EW theory and practically all identification methods discussed thus far naturally assume smooth wave-like, (i.e., sinusoidal) structures. Though this assumption may be at times justifiable for dry waves in the stratosphere, localization of signals along with coupling to convection in CCEWs can be expected to create significant non-sinusoidal signals, the degree of which will depend on the field analysed. The fact that, for example, convective heating and rainfall occur predominantly in one phase of the wave introduces asymmetry, which leads to spectral broadening. Both isolated wave packets and sharp spatial gradients will produce power across a range of  $k$ , whereas abrupt changes in time transform into a broad  $\omega$  range. Such effects may be less significant for a smoother field such as OLR, which reflects the longer-lived anvils of convection reaching well beyond individual rain shafts. It may not come as a surprise, therefore, that Li and Stechmann (2020) find higher predictability for wave-related OLR features than for precipitation.

- **Off-equatorial signals:** In many parts of the Tropics, the main band of tropical convection is not (or not always in the seasonal evolution) centred on the Equator, forcing any coupling with EWs to take place off-Equator, too, as thermodynamic conditions elsewhere do not allow convection (e.g., Straub and Kiladis, 2002). Depending again on which parameter is used to identify EWs, this asymmetry will create a mismatch between the assumed wave structures and coherent features of the real atmosphere, which leads to a spread of signal in  $k$ - $\omega$  space. Examples are West Pacific typhoons that tend to project onto MRGs (e.g., Frank and Roundy, 2006), whereas African Easterly Waves and Atlantic hurricanes tend to fall into the “gap” between MRGs and WIGs and are often categorized as TDs. Furthermore, KWs are distorted from their theoretical pattern by off-equatorial forcing and, in this case, exhibit a secondary meridional circulation (Gill, 1980; Dias and Pauluis, 2009).
- **Extratropical interactions:** There is evidence of extratropical forcing projecting directly onto EW modes (Hoskins and Yang, 2000) and of nonlinear energy transfer from extratropical waves to EWs (Majda and Biello, 2003). This has been analysed specifically for ER waves (Kiladis and Wheeler, 1995; Schlueter *et al.*, 2019b), MRG waves (Maganã and Yanai, 1995; Kiladis *et al.*, 2016), and KWs (Straub and Kiladis, 2003). These interactions occur particularly in regions of upper-level westerlies, such as over the eastern tropical Pacific and Atlantic in boreal winter, where Rossby waves from the midlatitudes can penetrate deep into the lower latitudes and influence convection there (Kiladis and Weickmann, 1992; Waugh and Funatsu, 2003; Knippertz, 2007). These disturbances will tend to maximize at upper tropospheric levels, move eastward, and project onto synoptic scales (i.e.,  $k = 5$ – $10$ , periods of 2–10 days; Gehne and Kleeman, 2012). Surprisingly, however, Castanheira and Marques (2015) find extratropical signals to project more strongly onto EIGs, MRGs, and KWs than onto ERs.
- **Interactions with the ocean:** For the slowest atmospheric EWs (i.e., mostly the MJO), interactions with fast oceanic KWs have been discussed that could further broaden spectral peaks (Roundy and Kiladis, 2006; Gribble-Verhagen and Roundy, 2010), but these are not the focus of this paper.

Given these many complicating factors, the choice of filtering window in  $k$ - $\omega$  space is inevitably a compromise between maximizing the signal-to-noise ratio and missing parts of the real-world coherent signal. As already explained herein, projections onto three-dimensional normal modes use instantaneous dynamical fields and

therefore do not have to apply a frequency filter. All spatial information available is decomposed into wave modes, irrespective of time behaviour. Some noise will naturally project onto the three-dimensional modes, particularly at the smallest spatial scales of divergent inertio-gravity waves (Tulich and Kiladis, 2012). Cross-spectral analysis of three-dimensional normal modes with OLR shows broad power in the  $k$ - $\omega$  spectrum, spanning a wide range of  $D$  values and reaching into parts of the spectrum classically associated with other types of EWs (Castanheira and Marques, 2015). Similar results are found for the projection onto PCFs without a frequency filter (G.-Y. Yang, unpublished results), but a broad frequency filter is typically used to remove the diurnal cycle at the fast end and seasonal variation on the slow end (Yang *et al.*, 2003). This suggests that we are dealing with features that are coherent in phase and have steady phase propagation (and thus are not noise) but have a structure that differs from the assumed basis functions due to the reasons already listed herein. The grand challenge in this is that we do not know exactly how this mismatch looks in a given context.

Therefore, the systematic comparison between the different identification methods in this paper will provide new insights into the nature of the structures contributing to the spectral broadening. Specifically, we will analyse the fundamental differences between methods that are narrow (filter window methods) or broad (spatial projection methods) in  $k$ - $\omega$  space. As far as possible, we will use consistent datasets, time periods, and types of display to allow the fairest possible comparison. Real data from satellite and reanalysis will be compared with artificial randomized data to illustrate the issue of isolating signal from noise. Further attention will be paid to how different methods deal with the abrupt end of time series, a common problem in monitoring and forecasting applications (e.g., Wheeler and Weickmann, 2001; Janiga *et al.*, 2018). Given the recent advances in EW forecasting (Dias *et al.*, 2018; Janiga *et al.*, 2018; Yang *et al.*, 2021) and new satellite observations for monitoring, a systematic comparison of EW identification methods is timely and useful for a growing number of scientists. Despite the focus of this paper on the tropical troposphere, many results are of relevance to the middle atmosphere, and to other planetary atmospheres and geophysical fluids.

Section 2 provides a summary of the linear theory of EW relevant to this paper. In Section 3, the most common EW identification methods will each be introduced and related to each other. Though emphasis will be given to the “primary” methods used to identify EWs in the first place, a short subsection will be dedicated to “secondary” methods; that is, those that associate EWs with other fields. Section 4 will present the comparison between the methods and their performance in a case study and

climatological context. Finally, Section 5 will summarize and discuss the most important insights from this comparison and outline future areas of research.

## 2 | THEORETICAL BACKGROUND

The foundations of EW theory are the frictionless, adiabatic primitive equations on the sphere, linearized around a resting basic state with stable stratification (and a horizontally constant potential temperature  $\theta$ ). Since the resting state is also in hydrostatic balance, the horizontal homogeneity of  $\theta$  implies that there are no background horizontal gradients in geopotential either (i.e., a barotropic state). Analytical solutions can then be constructed using vertical- and horizontal-time separability, yielding vertical and horizontal structure equations. The two are connected by the separation constant or equivalent depth  $D$ . The vertical structure equation can be solved given suitable top and bottom boundary conditions. The horizontal structure equations are identical in form to the linearized, rotating global shallow-water equations (RSWEs) and are also known as the Laplace tidal equations without forcing (e.g., Kasahara, 1976; Swarztrauber and Kasahara, 1985). In the following, we will summarize some key theoretical underpinnings for EW identification. The reader is referred to Matsuno (1966), Kiladis *et al.* (2009), Wheeler and Nguyen (2015), Webster (2020), or Žagar and Tribbia (2020) for a more detailed treatment of the problem.

The RSWEs are usually formulated using pressure  $p$  as the vertical coordinate and considering perturbations in zonal wind  $u'$ , meridional wind  $v'$ , and geopotential  $\phi'$ . Alternatively, geometric height  $z$  or  $\theta$  can be employed as the vertical coordinate. An equivalent derivation in terrain-following coordinates was first developed by Kasahara and Puri (1981). It is also convenient to recombine  $u'$  and  $\phi'$  into the so-called characteristic variables  $q' = \alpha\phi' + u'$  and  $r' = \alpha\phi' - u'$  (where  $\alpha = (g/D)^{0.5}$ ) because EW solutions in these variables can be written as a series expansion of PCFs, and therefore projection of data onto EWs is more straightforward (e.g., Gill, 1982; Ogrosky and Stechmann, 2015; Boyd, 2018).

Solutions of the RSWEs for a given vertical mode number  $m$  (and thus associated equivalent depth  $D_m$ ) have the following form:

$$|u', v', \phi'|^T = A_n^k(m) \mathbf{H}_n^k(\lambda, \varphi; m) e^{-i\omega_n^k(m)t}. \quad (1)$$

The horizontal structure functions  $\mathbf{H}_n^k(\lambda, \varphi; m)$  define global patterns in longitude  $\lambda$  and latitude  $\varphi$  and are known as Hough harmonics (Hough, 1897; Longuet-Higgins, 1968; Swarztrauber and Kasahara, 1985). For



every vertical mode  $m$ , the structures depend on the zonal wave number  $k$  and the meridional mode index  $n$ . The exponential term defines an oscillation in time  $t$  with a frequency of  $\omega_n^k(m)$ . The Hough functions have the simple wave form  $\exp(ik\lambda)$  in the longitude direction, and therefore the zonal phase speed is given by  $\omega_n^k(m)/k$ . The coefficients  $A_n^k(m)$  describe the amplitude for each  $n$ ,  $k$ , and  $m$ . The eigensolutions shown define the three-dimensional normal mode functions upon multiplying by the vertical structure functions,  $\mathbf{V}_m(p)$  (e.g., Boyd, 2018).

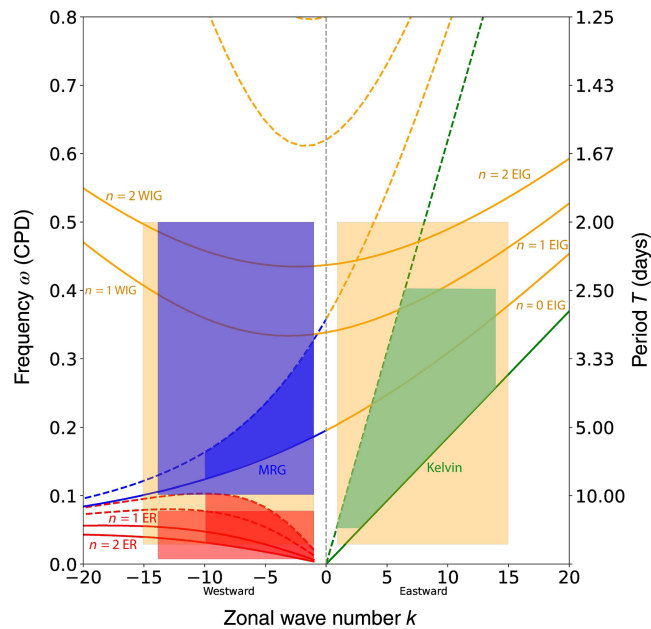
An approximation often made in tropical meteorology, including in the seminal work by Matsuno (1966), is to replace the full nonlinearly varying Coriolis parameter  $f$  by  $\beta a\varphi$ , with  $a$  being the Earth's radius. The Rossby parameter  $\beta$  is the derivative of  $f$  with respect to  $y = a\varphi$ . At  $30^\circ$  of latitude from the Equator, the difference between the equatorial  $\beta$ -plane and full  $f$  is still only about 10%, but it quickly grows beyond that. Boyd (1985; Boyd and Zhou, 2008) showed that the  $\beta$ -plane is justified as long as the motions of interest do not extend beyond a latitudinal threshold controlled by  $L + k^2$ , where  $L$  is the Lamb parameter, defined as  $L = 4\Omega^2 a^2 / (gD)$ . Solutions for the RSWEs on the equatorial  $\beta$ -plane are given in terms of PCFs in the meridional direction, the structure of which depend on  $D$ . These replace the Hough functions of the spherical solutions. The characteristic variables  $q'$  and  $r'$  have individual PCFs as orthogonal solutions, whereas the physical variables  $u'$  and  $\phi'$  require linear combinations of PCFs and, therefore, are not necessarily orthogonal to each other (Yang *et al.* 2003).

Figure 1 shows the dispersion behaviour of equatorial  $\beta$ -plane solutions for  $D$  of 8 m and 90 m. Dispersion curves for larger  $D$  are generally shifted towards higher frequencies, and thus faster propagation. Positive (negative)  $k$  indicates eastward-propagating (westward-propagating) solutions. For the range of  $k$ ,  $\omega$ , and  $D$  shown, the respective spherical solutions are practically undistinguishable from the ones shown in Figure 1 but do differ markedly for large  $D$  and  $k$  (Žagar *et al.*, 2015; Webster, 2020). There are also differences in nomenclature, in particular with respect to the meridional mode number  $n$ , with Figure 1 showing labels for the  $\beta$ -plane solutions. The differences result from the changes to the dispersion relationship when applying the  $\beta$ -plane approximation. On the sphere, the dispersion relationship for a given  $D$  and combinations of  $k$  and  $n$  has three roots with corresponding  $\omega$  and eigensolutions. The two solutions of the first kind (e.g., Swartrauber and Kasahara, 1985) are high-frequency inertial gravity (IG) waves that propagate eastward (EIGs) or westward (WIGs) (top part of Figure 1). The solution of the second kind is a low-frequency, westward-propagating Rossby wave

(bottom left part of Figure 1). The lowest meridional EIG ( $n = 0$ ) is the KW, whereas the lowest Rossby mode ( $n = 0$ ) is the MRG. The frequencies of the MRG approach that of the  $n = 1$  EIG for  $k$  close to zero. This EIG is labelled  $n = 0$  in Figure 1 according to the  $\beta$ -plane convention. The frequencies of the WIG modes connect to the frequencies of the EIG modes with  $n$  greater by 2, for example, WIG  $n = 0$  connects with EIG  $n = 2$  (Kasahara, 1978). These are the only modes defined for  $k = 0$ . In contrast, on the equatorial  $\beta$ -plane, the KW is denoted by  $n = -1$ , as it is a special solution to the respective dispersion relation. For  $n = 0$ , we obtain two roots, the MRG and the EIG  $n = 0$  mode—referred to as eastward-propagating MRG or EMRG in Yang *et al.* (2003). For  $n = 1$  and larger, there are three roots (WIGs, EIGs, and ERs). This way, the  $\beta$ -plane  $n$  values agree with those of the spherical solutions for ERs, but they are smaller (larger) by one for EIGs (WIGs). We will use the  $\beta$ -plane nomenclature from now on.

An important characteristic of the different EW solutions is their meridional structure, which depends on  $D$  and  $k$ . As an example, Figure 2a,b shows the latitudinal structure of spherical solutions of  $u'$  for KWs and of  $v'$  for MRGs for  $k = 1$  and  $k = 20$ , and  $D = 8$  m and  $D = 90$  m. As both have the same meridional mode number  $n = 0$  (in the spherical solutions), the structures obtained are all unimodal with positive (negative) values for KWs (MRGs). The selected curves illustrate that higher  $m$  (i.e., smaller  $D$ ; dashed lines) is associated with a stronger equatorial trapping for the same  $k$ . For the relatively small values of  $D$  used here, changing  $k$  (red lines) has little impact on the meridional structure of KWs, but for MRGs a higher  $k$  implies a larger amplitude near the Equator. This is related to a more complicated dependence on  $k$  and latitude of the MRG solutions (Paldor *et al.*, 2018). For values of  $D$  of a few kilometres, differences in the meridional scales of the wave solutions for different  $k$  are much greater (e.g., Žagar *et al.*, 2015, fig. 5). Figure 2c illustrates the relationship between different meteorological parameters for the ER  $n = 1$  wave and  $k = 1$  and  $D = 90$  m, which is characterized by two off-equatorial (at  $13^\circ$  N/S) maxima in  $\phi'$  (black line) with a (still positive) minimum at the Equator and a fall off in amplitude towards  $40^\circ$  N/S. In between these maxima is a prominent negative peak in  $u'$  with weaker opposite zonal flow poleward of the peaks in  $\phi'$ .  $v'$  has a much smaller amplitude, with negative (positive) values in the Northern Hemisphere (Southern Hemisphere) reflecting the change of sign of  $f$ .

The meridional structure of the  $\beta$ -plane solutions is expressed through PCFs. Figure 2d shows the PCFs for the first three meridional mode numbers  $n$  for a latitude scale  $y_0$  of  $6^\circ$ , as used in the rest of the paper. We start numbering the PCFs from zero as in Yang *et al.*, 2003, whereas Gehne and Kleeman (2012) start from 1.  $y_0$  is proportional to the



**FIGURE 1** Dispersion relation of the linear wave solutions of the rotating shallow-water equations on the equatorial  $\beta$ -plane. Wave frequency  $\omega$  is plotted for zonal wave numbers  $k$  up to  $\pm 20$  for equivalent depths of 8 m (solid lines) and 90 m (dashed lines). The lowest two meridional modes ( $n = 1, 2$ ) are shown for westward-moving inertio-gravity waves (WIGs), eastward-moving inertio-gravity waves (EIGs), and equatorial Rossby waves (ERs). CPD, cycles per day; MRG, mixed Rossby–gravity wave. The shaded areas mark the regions used for filtering in three-dimensional spatial projection using Hough functions and two-dimensional spatial projection using parabolic cylinder functions (large rectangles), two-dimensional spatial projection using time-extended empirical orthogonal functions (three light-shaded areas), and frequency–wave-number filtering methods (three dark-shaded areas). The solutions for the sphere are almost indistinguishable for the ranges shown here. Differences between the two, including those in nomenclature, are discussed in Section 2 [Colour figure can be viewed at [wileyonlinelibrary.com](http://wileyonlinelibrary.com)]

fourth root of  $D$ , indicating that horizontal structures are less sensitive to assumptions about  $D$  than vertical structures are, which allows a fairly robust projection for wave identification. A  $y_0$  of  $6^\circ$  corresponds roughly to  $D = 43$  m; that is, somewhere in the middle of the range shown in Figure 2a,b. The unimodal PCF0 shows similarities to the  $D = 90$  m KW and MRG structures in Figure 2a,b, whereas PCF1 resembles  $v'$  in Figure 2c. PCF2 has a minimum at the Equator and maxima to the north and south of it. The  $u'$  and  $\phi'$  signals in Figure 2c can be understood as linear combinations of PCF0 and PCF2 with different signs—see discussion in Yang *et al.* (2003).

The solutions found give us a powerful framework to isolate linear wave modes in the Tropics, as long as the phenomena at hand do not deviate too far from the assumptions made. Using modal structures given by theoretical

analysis of perturbations to a resting atmosphere has a great advantage, in that consistent spatial and temporal relationships between variables can be deduced from the physical equations. However, shear in the background flow is expected to modify the spatial structures of normal modes (e.g., introducing vertical and meridional tilt), change the frequencies, and also introduce non-modal behaviour. The extent to which the structures used for a projection basis are relevant to atmospheric behaviour must be deduced from the temporal coherence of the motions. Though computationally straightforward and cheap, the analysis has to be performed globally, which may be considered impractical compared with methods focusing on the tropical region (and individual vertical levels). Therefore, a range of methods have been developed to reduce complexity and to bin and compress information in an adequate way, as described in the next section.

### 3 | IDENTIFICATION METHODS FOR EQUATORIAL WAVES

In this section, we will describe, categorize, and compare six different approaches that have been developed in the last two decades to identify EWs. A first overview can be gained from the schematic shown in Figure 3. Generally, one needs to distinguish the method (and data) used to identify EWs in the first place (referred to as the primary method) and the additional method (and data) used to link the identified EWs to other fields (referred to as the secondary method). A typical example is using satellite-measured OLR and Fourier filtering in longitude and time as the primary method and linear regression (e.g., of winds, temperature, or moisture from reanalyses) to associate their effect on other fields as the secondary method (e.g., Wheeler *et al.*, 2000). We will concentrate on the main types of primary methods in the following and only briefly touch upon secondary methods at the end of the section. We will mainly distinguish methods dominated by spatial projection (Sections 3.1–3.3) and those dominated by space–time filtering using Fourier or wavelet transforms (Sections 3.4–3.6). Some concluding remarks on secondary methods, data, and real-time applications will be given in Section 3.7.

#### 3.1 | Three-dimensional spatial projection using Hough functions

The central idea of the three-dimensional spatial projection using Hough functions (3DS-HF) method is a multivariate spatial projection of instantaneous fields of horizontal wind and (pseudo-)geopotential height onto

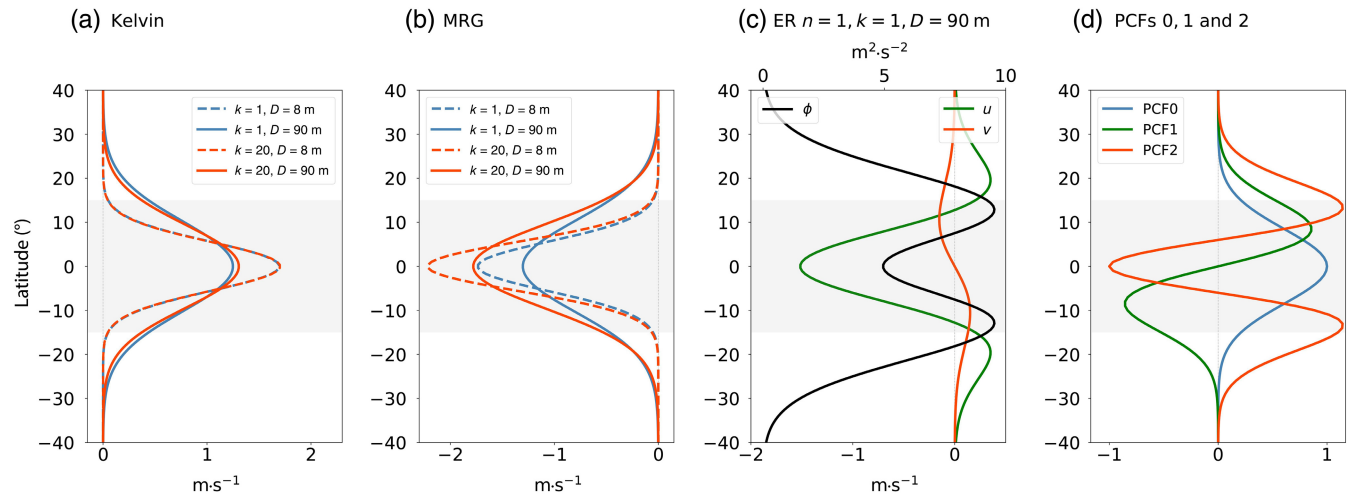


**FIGURE 2** Latitudinal profiles of different equatorial wave solutions. Spherical solutions for (a) Kelvin wave zonal wind  $u'$  and (b) mixed Rossby–gravity wave (MRG) meridional wind  $v'$ , both for  $D = 8$  m and  $D = 90$  m and for  $k = 1$  and  $k = 20$ , as well as (c) the  $n = 1$  equatorial Rossby wave (ER)  $u'$ ,  $v'$ , and geopotential  $\phi'$  for  $k = 1$  and  $D = 90$  m. These curves were produced using the software developed by Swarztrauber and Kasahara (1985). (d) Parabolic cylinder functions (PCFs) 0, 1, and 2 for  $y_0 = 6^\circ$ . The  $15^\circ$  S– $15^\circ$  N belt for averaging throughout the paper is shaded in grey [Colour figure can be viewed at [wileyonlinelibrary.com](http://wileyonlinelibrary.com)]

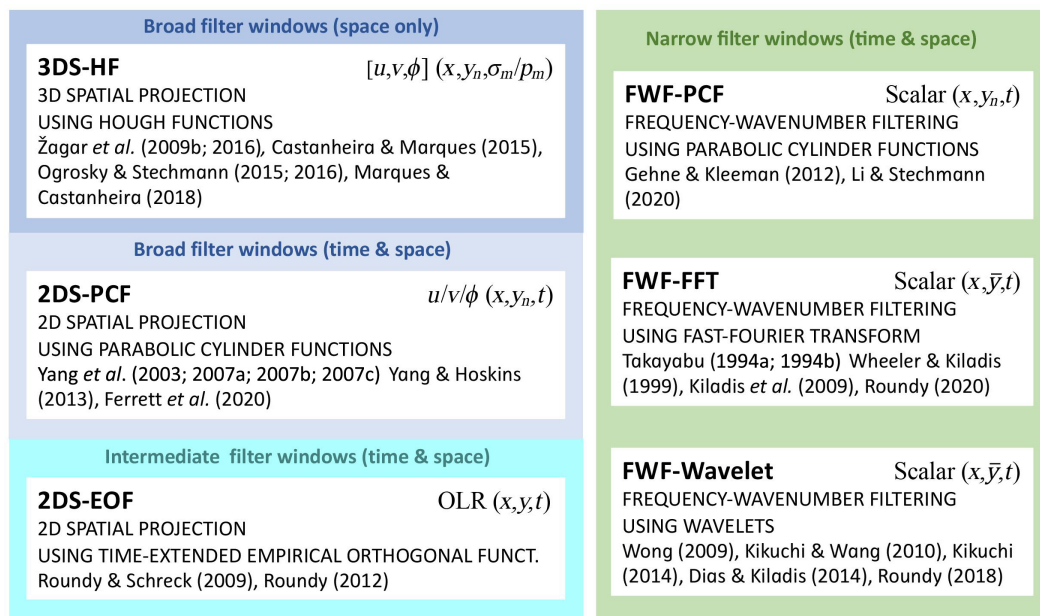


**FIGURE 3** Identification methods investigated in this paper. Each method is given with its full name and abbreviation, as well as a list of key publications. The top right corner of each box provides information about the input fields used with each method, together with the coordinates employed. Subscripts  $n$  and  $m$  stand for meridional and vertical modes, respectively; an overbar indicates a latitudinal average. OLR, outgoing long-wave radiation,  $u$ , zonal wind;  $v$ , meridional wind;  $\phi$ , geopotential;  $p$ , pressure,  $\sigma$ , terrain-following coordinate. The frequency–wave–number methods can, in principle, be applied to any two-dimensional scalar field (OLR,  $u$ ,  $v$ , and  $\phi$ , but also divergence and rainfall). The methods are grouped according to the size of the filters used to identify EWs. For more details, see Section 3 [Colour figure can be viewed at [wileyonlinelibrary.com](http://wileyonlinelibrary.com)]

three-dimensional normal-mode functions (see discussion in Section 2). Input fields typically come from (re-)analyses, weather forecasts, or climate simulations. The projection can be done using global fields in  $\sigma$ - (e.g., Žagar *et al.*, 2009b; Blaauw and Žagar, 2018) or

$p$ -coordinates (Castanheira and Marques, 2015; Marques and Castanheira, 2018). It can be applied to full fields or anomalies; for example, with respect to the mean seasonal cycle or differences between analyses and forecasts (e.g., Žagar *et al.*, 2010; 2016).

The main steps of the analysis—largely following Žagar *et al.* (2009a, 2009a; 2015) and Castanheira and Marques (2015)—are as follows. (a) Compute a representative vertical stability profile from global temperature data and use it—together with upper and lower boundary conditions—to numerically compute vertical structure functions. (b) Jointly project instantaneous fields of  $u$ ,  $v$ , and (modified)  $\phi$  onto these structure functions to obtain horizontal coefficient vectors for each vertical mode  $m$ . (c) Make horizontal coefficient vectors for each  $m$  dimensionless and project them onto Hough functions with zonal mode  $k$  and meridional mode number  $n$ . (d) Restrict the results to the modes of interest (e.g., with respect to  $k$  or wave type). (e) Transform selected modes back to physical space. (f) Fields in physical space can then be filtered in time to extract certain wave behaviour using the FFT.

The strength of this method is that the normal-mode functions form a complete set of orthogonal basis functions that reflect a multitude of different dynamical structures without a restriction on  $D$ . A disadvantage is a larger amount of data needed as input and a higher computational cost compared with other methods. In addition, the assumption of a resting background state with one globally representative vertical stability is somewhat questionable given a Pole-to-Equator difference in  $\theta$  of about 40 K at 600 hPa, whereas climatologically larger scale, free-tropospheric horizontal temperature gradients within the Tropics are small. As an alternative with reduced complexity, Ogrosky and Stechmann (2015; 2016) develop the theory in a  $z$  coordinate system with Boussinesq and  $\beta$ -plane assumptions and a rigid lid at 16 km, and restrict the analysis to the first tropospheric baroclinic mode as estimated from fields at 850 and 200 hPa.

### 3.2 | Two-dimensional spatial projection using PCFs

The two-dimensional spatial projection using PCFs (2DS-PCF) method, which was originally developed by Yang *et al.*, 2003, is also predominantly a spatial projection of dynamical fields. Key differences to 3DS-HF are: (a) An optimal  $D$  (and thus trapping scale  $y_0$ ) is determined on the basis of  $v$  variability at 200 hPa in the Tropics. Yang *et al.*, 2003 use  $y_0 = 6^\circ$ , whereas others have used  $5^\circ$  (Takayabu, 1994a; 1994b, 1994b),  $6.75^\circ$  (Li and Stechmann, 2020), and  $7\text{--}14^\circ$  (Kiladis and Wheeler, 1995). This way, projections can be done independently for individual vertical levels. (b) An equatorial  $\beta$ -plane approximation is used and analyses are restricted to the tropical belt— $20^\circ\text{S}$ — $20^\circ\text{N}$  in Yang *et al.* (2003). (c) Before projection (and not after as in 3DS-HF), fields of  $u$ ,  $v$ , and  $\phi$  (usually on pressure levels) are filtered using an FFT in  $\lambda$  and  $t$  in order to

isolate westward- and eastward-moving components in broad ranges of  $k$  and  $\omega$ — $2\text{--}10$  and  $3\text{--}30$  days, respectively, in Yang *et al.* (2003). (d) The Fourier coefficients for each  $k$  and  $\omega$  are then individually projected onto PCFs using characteristic variables  $v$ ,  $r$ , and  $q$  rather than the more conventional variables  $v$ ,  $u$ , and  $\phi$  for the reasons explained in Section 2. The final step (similar to 3DS-HF) is a transformation back to physical space for each wave mode, allowing the plotting of horizontal patterns at different times and vertical levels in order to check propagation behaviour, vertical structure, or the relationships between individual variables. This method isolates KWs, MRGs, and different EIG meridional modes—note that EIG  $n = 0$  is referred to as an eastward-moving MRG in Yang *et al.* (2003)—but cannot distinguish between ERs and WIGs due to their identical meridional structure (although the separation of these wave modes is usually obvious from the frequency associated with the wave power; see Figure 1).

Advantages of this method include no assumptions on vertical structure (other than indirectly through the choice of  $y_0$ ) nor relationships between variables via dispersion relations. The large  $k$ – $\omega$  window reduces the impact of edge effects in real-time applications or for short datasets. The method described here has been the foundation for a multitude of detailed studies on EWs and related phenomena (Tindall *et al.*, 2006a; 2006b; Yang *et al.*, 2007a; 2007b; 2007c; 2009; 2018; Yang and Hoskins, 2013; 2016; 2017; Ferrett *et al.*, 2020) and has recently been extended for real-time analysis and forecast applications in Yang *et al.* (2021). Whereas 2DS-PCF has mostly been applied as a univariate projection method in tropical dynamics research, a multivariate version was employed for studying properties of tropical forecast errors but without time filtering (Žagar *et al.*, 2005b).

### 3.3 | Two-dimensional spatial projection using EEOFs

The two-dimensional spatial projection using EEOFs (2DS-EEOF) approach, which is described in detail by Roundy and co-workers (Roundy *et al.*, 2009; Roundy, 2012c), is similar to 2DS-PCF in that it projects space–time-filtered data onto predefined two-dimensional patterns, but here these fields are not dynamical but convection related (usually OLR), and the patterns are not theoretical but obtained from an EEOF analysis. In contrast to 2DS-PCF, filter windows are chosen for individual wave types (KW, ER, MJO, 2–10 Day Westward) and not solely to separate eastward- and westward-propagating signals. The patterns for projection are obtained from the EEOF in the following way: (a) Define (at least 10) adequate time lags for each filter window (i.e., wave



type). The shortest time steps must be less than half of the shortest period intended to be resolved—thus daily for fast waves and up to about 20 days for the MJO; see Roundy *et al.* (2009, table I). (b) For each wave-type filtered dataset, create a time-extended matrix by padding the time series at each grid point by the lagged data, which adds an additional dimension to the data matrices. (c) Multiply the time-extended matrix with its transpose and compute eigenvectors. The resulting EEOF patterns can be plotted as time lag versus longitude averaged over latitude (Roundy *et al.*, 2009, fig. 6) or horizontal maps for a given time lag (Roundy *et al.*, 2009, fig. 8).

For the projection, an independent dataset of the same variable is first smoothed using centred moving averages with the same time windows as in the lag definition noted earlier to reduce noise. Then, the smoothed data are arranged into a padded matrix in the same way as for the EEOF computation (except that no separation by wave type is done). This matrix is then multiplied with the EEOF pattern of the lowest frequency waves to obtain the respective principal components (only, depending on  $t$ ) for this wave type. Subsequently, one reconstructs the lowest-frequency wave data from the principal components and associated EEOFs, and subtracts these from the unfiltered data. These two steps are repeated for all other wave types with increasing frequency. This successive treatment of the wave types prevents bleeding of information from low- onto higher-frequency processes. A great advantage of this approach is that, once the EEOFs are obtained from a climatology, the projection can be applied to real-time data without distortion. Roundy (2012c) simplified the original approach and reduced the computational expense by recreating the EEOFs from the spatial principal components instead of from the full grid of data. This revised algorithm allows for continuous integer time stepping in the lagged data matrix, allowing to skip the step of temporal smoothing. Combined with a statistical model (e.g., based on multiple linear regression), the approach can be used for prediction (Roundy, 2012c).

### 3.4 | Frequency–wave-number filtering using FFT

The method of frequency–wave-number filtering using FFT (FWF-FFT) was pioneered by Takayabu (1994a) and Wheeler and Kiladis (1999) based on the original work by Hayashi (1981) and is arguably the most widely used approach in the literature. Its key characteristic is the reliance on time–space filtering of two-dimensional horizontal fields (OLR, IR brightness temperature  $T_b$ , precipitation, horizontal divergence, etc.) in relatively narrow areas of  $k$ – $\omega$  space as opposed to the use of a projection

technique. The analysis is typically done using deseasonalized anomalies; that is, after removal of the first three harmonics of the seasonal cycle to prevent aliasing.

The filter windows for individual wave types (KW, ER, MRG, EIG, WIG, MJO) are defined on the basis of peaks in  $k$ – $\omega$  power spectra that stand above a smooth background spectrum. Details of the procedure are given in Wheeler and Kiladis (1999). The main steps are as follows: (a) computation of symmetric and antisymmetric components by adding and subtracting signals from corresponding latitudes in each hemisphere then dividing by 2; (b) division of data into overlapping time segments—for example, of 96 days in Wheeler and Kiladis (1999)—to minimize effects of spectral leakage; (c) removal of linear trends in each segment and tapering of endpoints using a cosine bell; (d) application of the complex FFT in  $\lambda$  and subsequently in  $t$  by latitude; (e) computation of  $k$ – $\omega$  power spectra and averaging over all segments; (f) summation over desired latitudes and smoothing of results to obtain a background spectrum; and (g) definition of filter windows (i.e., ranges of  $k$  and  $\omega$ ) for individual wave types taking into account the theoretical dispersion curves (Figure 1) for plausible ranges of  $D$ . These windows are much narrower than those used for 3DS-HF and 2DS-PCF.

To obtain wave-filtered fields, a  $k$ – $\omega$  power spectrum is computed as described earlier for the full deseasonalized data record (i.e., without segmentation). Taking the inverse Fourier transform for coefficients within the selected  $k$ – $\omega$  filter windows yields fields in physical space ( $\lambda, t$ ). Parts of this procedure have been used in a multitude of studies, often with only minor modification. For example, Roundy (2020) computes latitudinal averages prior to the FFT. Other authors replace the simple smoothing used by Wheeler and Kiladis (1999) by an autoregressive process (AR-1) (Hendon and Wheeler, 2008; Kikuchi, 2014; Castanheira and Marques, 2015; Marques and Castanheira, 2018).

### 3.5 | Frequency–wave-number filtering using wavelets

The Fourier transform used in FWF-FFT can be replaced by a wavelet-based approach, frequency–wave-number filtering using wavelets (FWF-Wavelet), to allow localization in  $\lambda$  (and thus using non-global data) and  $t$  (and thus for case studies). Instead of  $k$  and  $\omega$ , wavelets are characterized by a scale parameter and a phase speed, but these can be related to each other to obtain power spectra as in FWF-FFT. Approaches found in the literature include the following: (a) the complex spatio-temporal Morlet wavelet, which consists of a plane wave in  $\lambda$  and  $t$  localized with a Gaussian envelope (Wong, 2009; Kikuchi and Wang, 2010;

Kikuchi *et al.*, 2018); (b) the real-valued Morlet wavelet in  $\lambda$  and  $t$  applied to a central longitude (Roundy, 2018); (c) a Fourier analysis in  $\lambda$  combined with complex Morlet wavelets for  $t$  (Kikuchi, 2014) (available from <http://iprc.soest.hawaii.edu/users/kazuyosh/>); and (d) a Fourier analysis in  $\lambda$  and  $t$  combined with a double Hann window (squared sine function) for localization in both variables (Dias *et al.*, 2013b; Dias and Kiladis, 2014). Apart from that, the different methods usually follow the steps outlined in Wheeler and Kiladis (1999) (choice of dataset, deseasonalization, treatment of latitudinal averages/summation, etc.). Depending on the application, the background used to normalize power spectra needs to be restricted to the  $\lambda$ - $t$  window considered.

### 3.6 | Frequency–wave-number filtering using PCFs

The frequency–wave-number filtering using PCFs (FWF-PCF) method, first described in Gehne and Kleeman (2012), largely follows FWF-FFT, but instead of the equally weighted symmetric and antisymmetric latitudinal averages used there, projections onto PCFs are applied before the FFT. Consistent with Yang *et al.*, 2003 a trapping scale of  $y_0 = 6^\circ$  is used and analyses are restricted to  $20^\circ$  S– $20^\circ$  N. Individual fields (e.g.,  $u$ ,  $v$ ,  $\phi$ , divergence, and  $T_b$ ) are projected separately. Subsequently, all steps (except for the latitudinal summation of power) follow Wheeler and Kiladis (1999) but are applied to the PCF coefficients rather than the original fields. Power spectra for symmetric and anti-symmetric signals can be created by summing over even and odd PCFs (see Figure 2d). For the normalization of power spectra, a background needs to be computed for each PCF. Results can be related to the solutions of the RSWE—see Gehne and Kleeman (2012, eq. 1) and Section 2—indicating that solutions for  $u$  and  $\phi$  should be linear combinations of PCFs. Other authors follow this idea in principle, but only use a limited set of PCFs or physical variables. For example, Li and Stechmann (2020) project precipitation fields onto PCF0 (which equals Gaussian-weighted averaging; see Figure 2d) and PCF1.

### 3.7 | Further remarks

The majority of studies discussed so far focus on climatological aspects of tropical waves, such as mean geographical or seasonal variations in the importance and structure of different wave types, but there is also growing interest in real-time applications, such as monitoring of current state and dynamical or statistical forecasting of wave phases and

amplitudes, as well as the associated rainfall. Generally speaking, all FWF methods have issues with an abrupt end of the time series. One way to deal with this is to combine atmospheric analyses with a model forecast to obtain a sufficiently long time series that can be tapered at the beginning and padded with zeros at the end (Wheeler and Weickmann, 2001; Janiga *et al.*, 2018). This issue is less problematic for the projection approaches (3DS-HF, 2DS-PCF, 2DS-EOF). For 3DS-HF, the MODES software by Žagar *et al.* (2015) provides real-time examples based on operational forecasts from the European Centre for Medium-Range Weather Forecasts (ECMWF; see <http://modes.cen.uni-hamburg.de>). 2DS-PCF has recently been implemented operationally at the UK Met Office, based on 83 days of analysis and 7 days of global forecast data (both six-hourly) (Yang *et al.*, 2021). Roundy (2012c) has developed a statistical model to extrapolate waves identified with 2DS-EOF into the future.

In addition, many papers combine their wave identification results with other datasets; for example, to further elucidate the relationship between different fields, to investigate vertical or horizontal structures, or to create composite time evolution. The most straightforward approach is linear regression. This usually begins with the choice of an adequate base point (or region); for example, where a certain wave type explains a large fraction of overall variance. Unfiltered fields of interest (e.g., winds, temperature, geopotential height) are regressed against wave-filtered data (e.g., OLR) at the base point. For the regression, time lags are considered that reflect the typical period of the wave type at hand and the analysis can be restricted to windows of activity (i.e., when the given wave type explains above a certain threshold of the background variance). The results are typically given as deviations in the wave-filtered quantity (e.g., two standard deviations to reflect the magnitude of typical events) and can be presented as horizontal maps, vertical sections, or longitude–time lag plots (Wheeler *et al.*, 2000). Other examples of this technique can be found in Yang *et al.* (2007a; 2007b; 2007c), Ogrosky and Stechmann (2016), and Roundy (2020).

Moreover, cross-spectral analysis between two fields offers a mathematically consistent way of combining datasets. An early example is given in Wheeler and Kiladis (1999), where OLR is combined with layer-mean temperature and 1000 hPa geopotential height. The analysis then largely follows the steps outlined in FWF-FFT, except that the co-spectra and quadrature spectra are calculated to determine the coherence and phase between two variables per  $k$ - $\omega$  bin. The final plots can be arranged in the same way as  $k$ - $\omega$  power spectra but showing coherence squared, which measures the ratio of the cross-spectral density of the two input fields relative to the product of

the individual spectral densities. It is thus sensitive to both amplitude and phase relationship for each  $k$  and  $\omega$ . The phase is often included in the plot as an arrow. Such plots have also been extensively used by Castanheira and Marques (2015; Marques and Castanheira, 2018) to link their three-dimensional normal mode-based results with OLR, allowing an assessment of CCEWs.

Finally, wave-phase composites can be constructed on the basis of a phase diagram at a given longitude, which plots wave-filtered data against its local time derivative (or another phase-shifted field) after division by the respective standard deviations to make the fields dimensionless (Riley *et al.*, 2011). The passage of a wave will appear as a circle in this diagram, with the radius indicating the amplitude of the signal. It is then common to break down this phase diagram into eight equal areas, with, for example, with phase 1 (5) being the maximum (minimum) in the wave-filtered field and phase 7 (3) the maximum (minimum) in the time tendency. After that, composites of unfiltered fields can be computed for each phase in the form of horizontal maps or vertical sections. Examples for this type of analysis, using model-generated fields and satellite measurements, can be found in Riley *et al.* (2011), Yasunaga and Mapes (2012a; 2012b), and Schlueter *et al.* (2019a; 2019b).

## 4 | SYSTEMATIC COMPARISON OF METHODS

In this section, the six methods discussed in Section 3 will be compared with each other in a systematic way. Section 4.1 provides information on the data employed and technical details about the methods used. Section 4.2 presents a case study for one season for KW, MRG, and ER, mostly through the use of Hovmoeller diagrams. Section 4.3 takes a climatological perspective and compares the variance explained by different EW types.

### 4.1 | Data and Methods

#### 4.1.1 | Data

Following the numerous examples in the literature, we will compare input data reaching from widely used OLR to dynamical fields from reanalyses. As a common period for all data, the 18 years 2001–2018 were chosen. All data but OLR are brought to the same  $1^\circ$  grid and a six-hourly time resolution before the EW analysis. An exception is 3DS-HF, which uses the regular  $256 \times 128$  Gaussian grid with about 150 km grid spacing at the Equator.

For OLR we use data from the National Oceanic and Atmospheric Administration (NOAA) available twice daily (Liebmann and Smith, 1996). This global dataset has a record going back to 1974 and has been used in many studies on tropical meteorology (Gruber, 1974; Wheeler and Kiladis, 1999; Yang *et al.*, 2003), where it has been shown to represent the broad-scale signal of deep tropical convection well. We will refer to this dataset as “OLR”.

A challenge with this dataset is the reliance on polar orbiting satellites to cover the full IR spectrum, allowing only a relatively coarse resolution in space and time. An alternative, therefore, is to use narrow-band IR data that is mostly based on information from geostationary satellites. Several older studies use the Cloud Archive User Service IR brightness temperature (in kelvin) dataset that was discontinued in 2009. A more recent example, and the dataset employed here, is the Clouds and the Earth’s Radiant Energy System (CERES) SYN1deg–Level 3 Window-region Flux ( $8\text{--}12\ \mu\text{m}$ ; in  $\text{W}\cdot\text{m}^{-2}$ ) (Doelling *et al.*, 2016) available three-hourly on a global  $1^\circ \times 1^\circ$  grid. We used a six-hourly resolution for our analysis (0000, 0600, 1200, and 1800 UTC) and refer to these data as “CERES”.

To represent precipitation, we use the satellite-based, globally gridded product Integrated Multi-Satellite Retrievals for Global Precipitation Measurement (GPM) (IMERG) V6B, final version (Huffman *et al.*, 2019), as described in detail in Huffman *et al.* (2015). This is a gauge-calibrated Level 3 product combining data from the GPM dual-frequency precipitation radar, multiple passive microwave instruments, and IR information from geostationary satellites. The data are available at  $0.1^\circ$  spatial resolution but were conservatively remapped to  $1^\circ$ . The original temporal resolution is 30 min, but here we use six-hourly averages centred on 0000, 0600, 1200, and 1800 UTC. We will refer to this dataset as “IMERG”.

For all three satellite-based datasets, anomalies are computed by subtracting the first three harmonics of the seasonal cycle from the data. To make them comparable, so called “Z scores” are computed; that is, the anomalies are divided by standard deviations based on daily mean fields. The justification for this is that the full six-hourly data are strongly influenced by the large diurnal variations over land. Such fields will be referred to as “OLR-Z”, for example.

Finally, for dynamical fields (wind, geopotential) we employ the ERA5 reanalysis dataset (Hersbach *et al.*, 2020). ERA5 is based on ECMWF’s Integrated Forecasting System Cy41r2, which was operational in 2016. The data are available every hour at a spatial resolution of 31 km. To be consistent with CERES and IMERG, ERA5 data were sampled every 6 hr and interpolated to  $1^\circ$ . Horizontal divergence interpolated to pressure levels is taken directly from ERA5 (it is a prognostic variable in the ECMWF

**TABLE 1** Filter windows to isolate Kelvin waves (KWs), mixed Rossby–gravity waves (MRGs), and equatorial Rossby waves (ERs) for the six methods compared in this paper (see Section 3 for details). For each wave type, zonal wavenumber  $k$ , wave period  $T$ , and equivalent depth  $D$  are provided

Method	KW			MRG <sup>a</sup>			ER		
	$k$	$T$ (days)	$D$ (m)	$k$	$T$ (days)	$D$ (m)	$k$	$T$ (days)	$D$ (m)
3DS-HF	$\pm 1$ to $\pm 15$	2–30	mult <sup>b</sup>	$\pm 1$ to $\pm 15$	2–30	mult <sup>b</sup>	$\pm 1$ to $\pm 15$	2–30	mult <sup>b</sup>
2DS-PCF	1–15	2–30	43 <sup>c</sup>	$-15$ to $-1$ <sup>d</sup>	2–30	43 <sup>c</sup>	$-15$ to $-1$ <sup>d</sup>	2–30	43 <sup>c</sup>
2DS-EOF	1–14	2.5–20	8–90	$-14$ to $-1$	2–10	–	$-14$ to $-1$	15–100	–
FWF-x	1–14	2.5–17	8–90	$-10$ to $-1$	2.5–10	8–90	$-10$ to $-1$	6.25–96	1–90

Notes: 3DS-HF, three-dimensional spatial projection using Hough functions; 2DS-PCF, two-dimensional spatial projection using parabolic cylinder functions; 2DS-EOF, two-dimensional spatial projection using time-extended empirical orthogonal functions; FWF-x, the three frequency–wave-number filtering methods (fast Fourier transform, wavelet, PCFs).

<sup>a</sup>Called “2–10 Day Westward” in 2DS-EOF.

<sup>b</sup>Twent-seven different  $D$  values.

<sup>c</sup> $D$  corresponding to  $y_0 = 6^\circ$ .

<sup>d</sup>In Section 4.3, positive  $k$  will be considered, too (MRG-E and ER-E).

model). Owing to the way this field is smoothed in the data assimilation process, the ERA5-analysed divergence is not identical to that calculated from the wind fields (e.g., using finite differences), and in fact is less coherent with independently derived IMERG precipitation estimates (not shown).

#### 4.1.2 | EW identification methods

The systematic comparison will be done with the six approaches described in detail in Section 3. In some cases, minor modifications are made to the original procedure to produce more consistent comparisons. The chosen filter windows in  $k$  and wave period  $T$  ( $= 2\pi/\omega$ ), as well as restrictions on  $D$  if they exist, are given in Table 1. These filter windows are also marked in Figure 1. The two methods using theoretical projection patterns (3DS-HF and 2DS-PCF) consistently use broad windows with  $k$  from 1 to 15 (or  $-1$  to  $-15$ ) for all EW types. Both also filter in time for wave periods  $T$  from 2 to 30 days, but 2DS-PCF does so before and 3DS-HF after the spatial projection (see Section 3 for details). In the most extreme cases, the filter window used in 2DS-PCF and 3DS-HF allows phase speeds at the Equator ranging from  $\pm 2$  to  $\pm 232 \text{ m}\cdot\text{s}^{-1}$ . The trapping scale of  $y_0 = 6^\circ$  chosen in 2DS-PCF corresponds to  $D = 43 \text{ m}$ , whereas 3DS-HF considers 27 different  $D$  values from 8 to 10,060 m. It should also be noted that 2DS-PCF separates westward- and eastward-propagating signals at the beginning, and therefore can also identify MRG and ER with positive  $k$  (termed MRG-E and ER-E, respectively, in Section 4.3), whereas 3DS-HF always contains both signs of  $k$ .

With respect to KW, the other methods use only slightly smaller windows in  $k$  and  $\omega$  but strongly restrict

the signals considered to a narrow, diagonal sector in  $k$ – $\omega$  space by assuming  $D$  to be between 8 and 90 m (see Figure 1 for a graphical depiction). This narrows the range of possible phase speeds to  $8.9$ – $29.7 \text{ m}\cdot\text{s}^{-1}$ . In the case of MRG, there are much larger differences between 2DS-EOF and the FWF methods (referred to as FWF-x in the following, where “x” indicates FFT, wavelet, and PCF). Whereas the former considers all waves with  $k$  from  $-14$  to  $-1$  and  $T$  between 2 and 10 days, the latter cut  $k$  already at  $-10$  and again assume  $D$  to fall between 8 and 90 m. Nevertheless, both approaches consider wide ranges of possible phase speeds of  $-3.3$  to  $-231.9 \text{ m}\cdot\text{s}^{-1}$  and  $-4.6$  to  $-185.5 \text{ m}\cdot\text{s}^{-1}$ , respectively. Finally, for ER, both 2DS-EOF and FWF-x focus on slow westward-moving waves with  $T$  of 15–100 days (2DS-EOF) and 6.25–96 days (FWF-x) and  $k$  down to  $-14$  and  $-10$ , respectively, but only FWF-x restricts  $D$  to 1–90 m. In the case of FWF-x (2DS-EOF), this corresponds to a phase speed range of  $-0.5$  to  $-74.2 \text{ m}\cdot\text{s}^{-1}$  ( $-0.3$  to  $-30.9 \text{ m}\cdot\text{s}^{-1}$ ). In addition, these methods also define filter windows for the MJO ( $k = 0$ – $10$  and  $T = 20$ – $100$  days for 2DS-EOF and  $k = 0$ – $5$  and  $T = 30$ – $96$  days for FWF-x; not shown in Table 1).

#### 4.2 | Case study

In order to illustrate the differences between the six methods portrayed in Section 3, we apply them to a common period from February 20 to May 20, 2009. This period occurred during the “Year of Tropical Convection” and was highlighted in Waliser *et al.* (2012) to feature multiple interacting CCEWs including the MJO, ER, and KW. After a short general introduction to the study period in Section 4.2.1, Section 4.2.2 will focus on KW activity, and



the following sections discuss MRG (Section 4.2.3) and ER (Section 4.2.4).

#### 4.2.1 | Overview

Figure 4 shows Hovmoeller plots for the entire 3-month study period based on unfiltered data averaged over  $15^{\circ}$  S– $15^{\circ}$  N. The OLR anomalies (Figure 4a) show a stable longitudinal structure with high-frequency variability over and near the African continent ( $20^{\circ}$  W– $50^{\circ}$  E), positive (i.e., dry) anomalies over the Indian Ocean ( $50^{\circ}$ – $100^{\circ}$  E), low-frequency variability over the Maritime Continent and Pacific Ocean out to about  $120^{\circ}$  W, and a mostly dry (wet) area to the west (east) of the Andes ( $80^{\circ}$  W). Several CCEWs can be seen by the naked eye. Three examples are marked with thick lines in all panels of Figure 4: (a) A convectively coupled ER that propagates with a phase speed of about  $-3.9 \text{ m}\cdot\text{s}^{-1}$  from the West Pacific to the Indian Ocean between mid-March and mid-April; (b) a convectively coupled KW that propagates with about  $15 \text{ m}\cdot\text{s}^{-1}$  from the central Pacific to Africa between late April and early May and appears to emerge from a prominent MJO event propagating across the Maritime Continent in the course of April interacting with the ER mentioned earlier; (c) a dry MRG over the Pacific at the beginning of the investigation period. Though the ER and KW (as well as the MJO event) are clearly documented in Waliser *et al.* (2012, fig. 4a), the MRG is only evident in dynamical fields (see Section 4.2.3).

The corresponding diagram for CERES (Figure 4b) is structurally similar to OLR but with a considerably lower amplitude due to the smaller part of the IR spectrum considered. However, though many negative anomalies are consistent between the two datasets (including the highlighted KW and ER waves), there are significant differences over dry areas. This is most evident when comparing the warm, dry areas over the Indian Ocean and West Pacific, which are prominent in both datasets, with the cold dry areas west of the Andes, which are de-emphasized in CERES. These differences lead to a pattern correlation between the two of 0.69 (after coarse-graining CERES data). Precipitation from IMERG (Figure 4c) shows a more fine-grained picture than CERES despite the same spatial resolution used here, reflected in a pattern correlation of only  $-0.46$ . Many more CCEWs are evident to the naked eye in IMERG data, including the ER and KW highlighted. The Andes show up as a sharp divide between dry and wet areas, but occasionally CCEWs appear to propagate across them.

The corresponding plots based on  $Z$  scores (Figure 4d–f) generally de-emphasize stationary longitudinal patterns and deviations between the three input fields, whereas the overall structures are maintained. For

example, CERES-Z and CERES have a pattern correlation of 0.87. One reason for the deviation from one is the dry area to the west of the Andes, which is much more prominent in CERES-Z than in CERES, indicating very low standard deviations there. Wet anomalies in OLR and CERES (including most CCEWs) are generally not as strongly affected by the standardization as dry regions are, but for IMERG (Figure 4f) much of the signal is shifted from the rainy, variable Warm Pool area to the drier, less variable eastern Pacific. The pattern correlation between CERES-Z and IMERG-Z of  $-0.49$  is almost identical to that of the raw anomalies ( $-0.46$ ).

Finally, Figure 4g–i shows corresponding analyses for raw (not anomalous) values of zonal wind at 850 and 200 hPa as well as 200 hPa divergence. The wind fields are dominated by large longitudinal structures. The 850 hPa zonal winds (Figure 4g) are predominantly easterly with maxima near the Date Line. The Andes and East African Highlands, where 850 hPa is below the model orography, appear as prominent low-wind areas. Westerlies occur only episodically, particularly over the Indian Ocean (e.g., in connection with the highlighted ER). EW signals are generally much harder to see in this field, including the highlighted KW. Wind signals at 200 hPa (Figure 4h) have larger amplitudes and are often opposite to 850 hPa (pattern correlation of  $-0.71$ ). This is to a large extent a reflection of the Walker cell over the tropical Pacific and a weaker, more variable meridional cell over the Indian Ocean. EWs are again difficult to see in the unfiltered winds. In stark contrast, divergence at 200 hPa (Figure 4i) is much more fine-grained in structure, resembling IMERG (Figure 4c) in many ways and including numerous evident EWs. Despite this, the pattern correlation between the two only amounts to 0.35.

Since background winds are important for EWs with respect to possible Doppler shifts as well as vertical and meridional shear, Figure 5 shows a height–longitude section of  $15^{\circ}$  S– $15^{\circ}$  N averaged zonal winds. The 850 and 200 hPa levels used to represent the lower and upper troposphere are marked. Strong vertical shear is evident over the Pacific between mean westerlies of more than  $15 \text{ m}\cdot\text{s}^{-1}$  around 100 hPa and easterlies of well above  $5 \text{ m}\cdot\text{s}^{-1}$  in the lower half of the troposphere. Opposite but much weaker shear occurs over the Indian Ocean, whereas the South American–Atlantic–African sector shows deep easterlies with a maximum in the mid-troposphere. The effect of this mean wind pattern on EWs will be discussed in the following subsections. Strong shear is also evident above 100 hPa.

#### 4.2.2 | Kelvin waves

In this section we compare Hovmoeller depictions of KW based on different datasets and methods. According to the

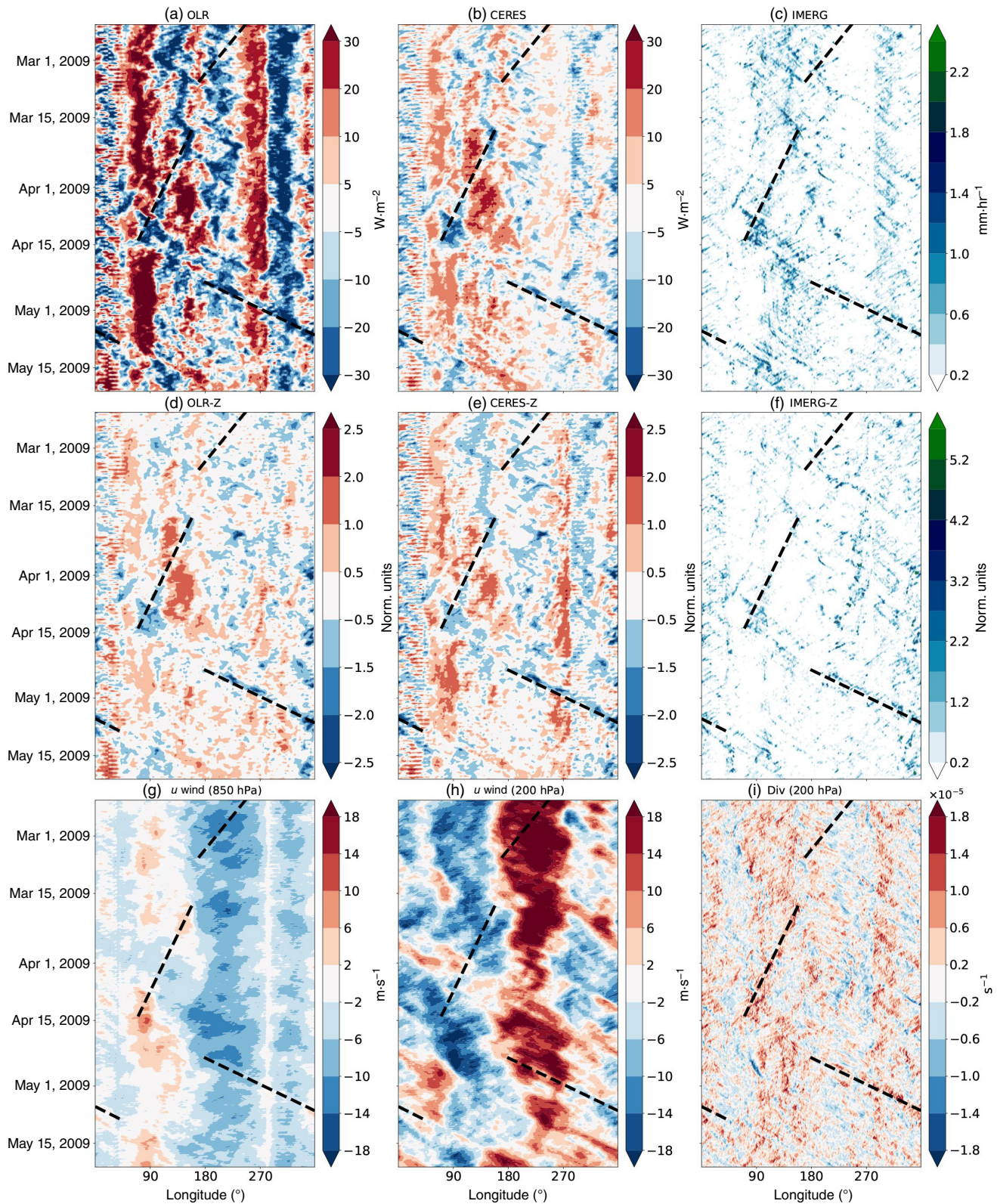


**FIGURE 4** Unfiltered Hovmoeller diagrams for February 20–May 20, 2009 (averaged  $15^{\circ}$  S– $15^{\circ}$  N). Anomalies from the 2001–2018 deseasonalized climatology for (a) outgoing long-wave radiation (OLR) from National Oceanic and Atmospheric Administration (twice daily), (b) narrowband infrared from the Clouds and the Earth’s Radiant Energy System (CERES; four times daily) and (c) precipitation from the Integrated Multi-Satellite Retrievals for Global Precipitation Measurement (IMERG; four times daily). (d–f) As (a)–(c) but for Z scores (i.e., anomalies normalized with the local daily standard deviation). (g–i) As (a)–(c) but for full fields of zonal winds at (g) 850 hPa and (h) 200 hPa as well as (i) divergence at 200 hPa from ERA5. The example cases for Kelvin waves, mixed Rossby–gravity waves, and equatorial Rossby waves discussed in this paper are marked by dashed lines [Colour figure can be viewed at [wileyonlinelibrary.com](http://wileyonlinelibrary.com)]



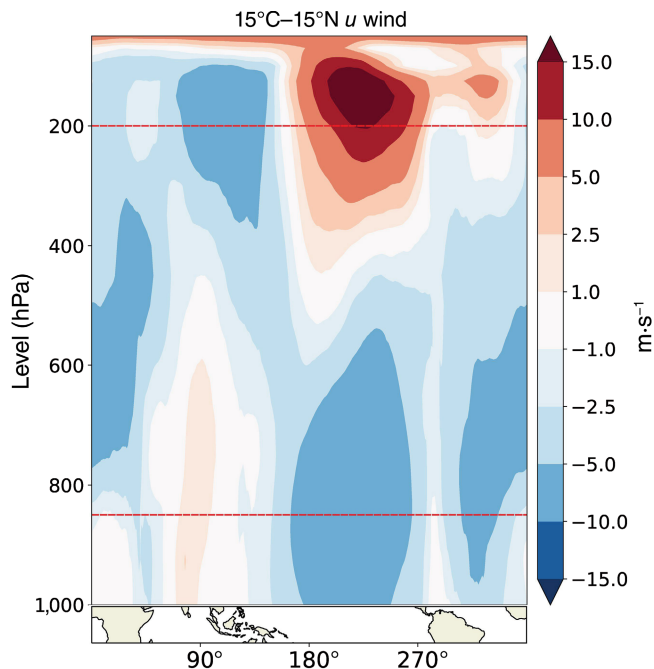


**FIGURE 5** Vertical profile of mean background zonal winds during February 20–May 20, 2009 (averaged 15° S–15° N). Data are taken from the ERA5 reanalysis. The vertical levels analysed in this study (i.e., 850 and 200 hPa) are marked. Note the nonlinear colour scale. A map is provided for better orientation [Colour figure can be viewed at [wileyonlinelibrary.com](http://wileyonlinelibrary.com)]

linear theory for perturbations to a resting atmosphere, KWs have structures symmetric about the Equator with perturbations in zonal wind and geopotential in quadrature with divergence and no meridional wind perturbations on the equatorial  $\beta$ -plane (small  $\nu$  on the sphere). If convectively coupled, one would expect OLR anomalies to be closely related to upper-level divergence. KWs propagate eastward and are non-dispersive. For example, see Kiladis *et al.* (2009) for more details.

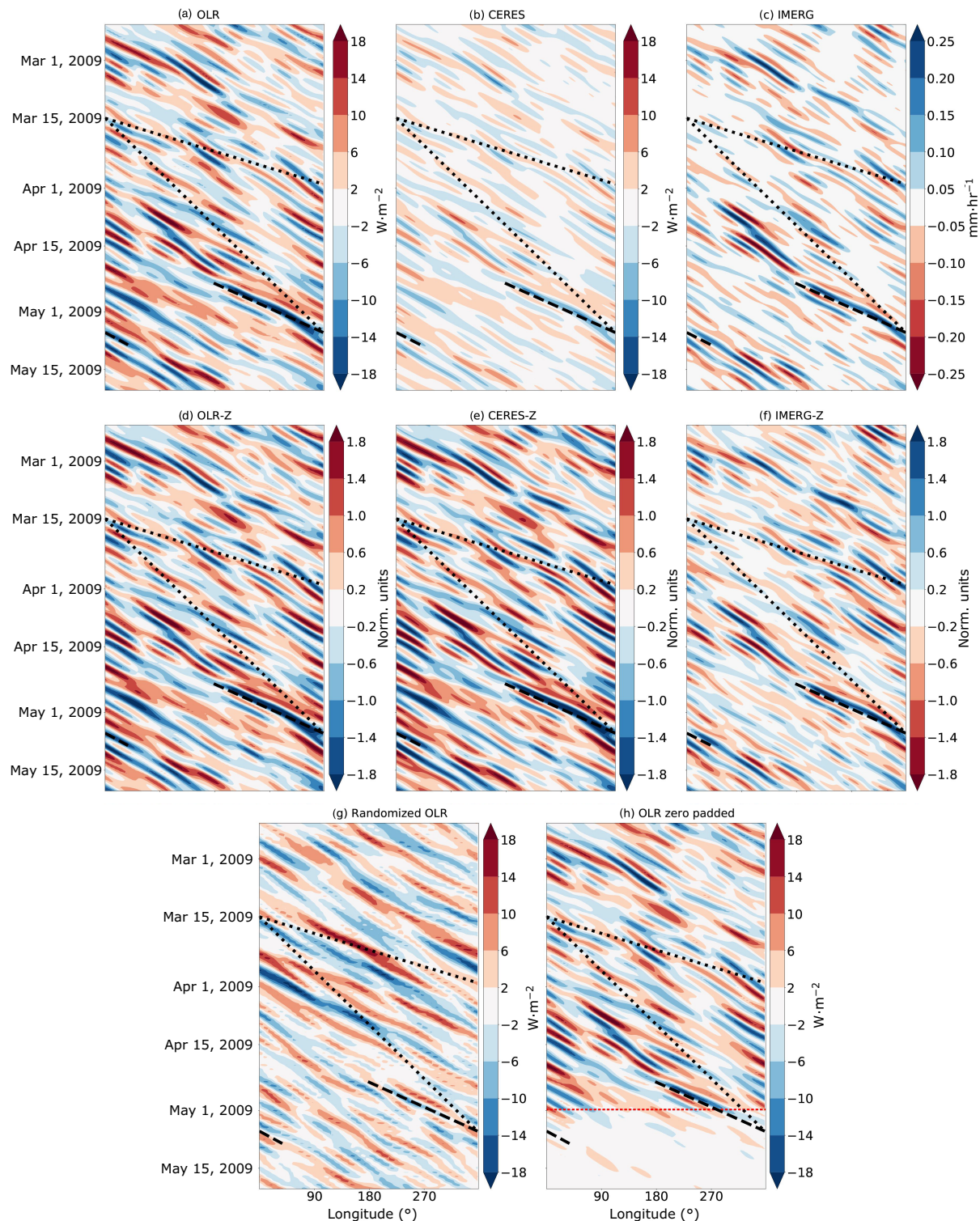
Figure 6 shows KW filtered data obtained by applying FWF-FFT to OLR, CERES, and IMERG anomalies as well as to their respective Z scores. Compared with the raw anomalies shown in Figure 4, the filtered fields are generally much smoother in longitude and extend even across topographic features such as the Andes. In OLR (Figure 6a), the identified waves appear quite regular in space and time. The example KW from Figure 4 is clearly evident, and its phase speed of  $15 \text{ m}\cdot\text{s}^{-1}$  is characteristic for the entire period (maximum and minimum phase speeds of the filter window are indicated in Figure 6). Amplitudes typically range from  $-15$  to  $+15 \text{ W}\cdot\text{m}^{-2}$  and are thus about half of the raw anomalies shown in Figure 4a. KWs in CERES (Figure 6b) correspond closely to those in OLR (pattern correlation 0.98 after remapping CERES to the OLR resolution) but with a much lower amplitude. IMERG (Figure 6c) shows many structures similar to

OLR and CERES but is much more accentuated, strongly emphasizing few individual waves (including our example KW). The pattern correlation between CERES and IMERG is  $-0.75$ , and therefore considerably larger in magnitude than between the raw anomalies ( $-0.46$ ). Comparing the KW filtered OLR anomalies with the corresponding Z scores (Figure 6d–f) shows that the normalization by the standard deviation has a much smaller effect when applied in combination with filtering. Pattern correlation between CERES and CERES-Z (Figure 6e), for example, is 0.99, indicating that the fields are mostly rescaled. IMERG waves remain accentuated when using Z scores (Figure 6f) with slightly reduced contrasts in time and longitude, leaving pattern correlations to other fields almost unchanged.

Figure 6g shows the results of FWF-FFT wave filtering applied to randomized OLR data, which are characterized by the same global  $k$ – $\omega$  power spectrum as the original data but shuffled in longitude and time—see Roundy (2020) for more details. The resulting Hovmoeller plot has many structural similarities to the real data shown in Figure 6a. Wave amplitudes are somewhat reduced, but some marked signals are discernible, particularly from mid-March to early April. Owing to the randomization, however, the pattern correlation between the two is very close to zero. This analysis demonstrates that although there is no coherent propagation in the raw data due to the random phases, applying the narrow  $k$ – $\omega$  filter and then transforming back to physical space results in patterns that could be mistaken for KW propagation. This implies that Hovmoeller plots from the FWF methods must be interpreted with caution by comparing with signals in the unfiltered data or from the spatial projection methods discussed later.

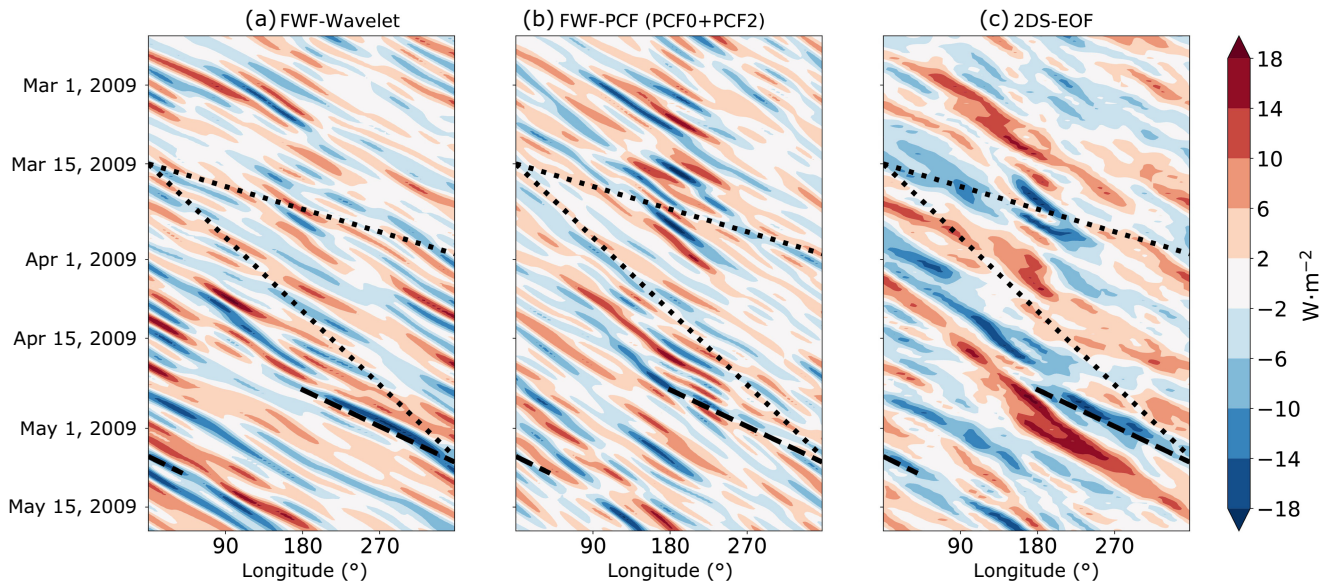
Figure 6h shows the same Hovmoeller plot as Figure 6a but with the data from May 1 onward replaced by zeros to mimic a near-real time monitoring situation (e.g., Wheeler and Weickmann, 2001, Janiga *et al.*, 2018). From this, it is evident that the time filtering, on the one hand, allows some wave signals to extend beyond May 1 and, on the other hand, causes distortion of the original results stretching backwards into April. A correlation along longitude between the two (not shown) reveals that the first deviations begin on April 22, but correlations remain above 80% until April 30. As mentioned already, such issues do not occur for the projection-dominated methods 3DS-HF, 2DS-PCF, and 2DS-EOF. Full decorrelation is reached roughly 10 days after the cut-off.

Figure 7 exclusively uses OLR as input but varies the method used for filtering compared with the reference method FWF-FFT (Figure 6a). The use of wavelets (Figure 7a) instead of FFT does not change the results much (pattern correlation 0.96). For FWF-Wavelet, peaks



**FIGURE 6** Hovmoeller diagrams for February 20–May 20, 2009, filtered for Kelvin waves (KW) using the frequency–wave-number filtering using fast Fourier transform method. Anomalies from the 2001–2018 deseasonalized climatology for (a) outgoing long-wave radiation (OLR) from National Oceanic and Atmospheric Administration (twice daily), (b) narrowband infrared from the Clouds and the Earth’s Radiant Energy System (CERES; four times daily) and (c) precipitation from the Integrated Multi-Satellite Retrievals for Global Precipitation Measurement (IMERG; four times daily). (d–f) As (a)–(c) but for corresponding Z scores (i.e., anomalies normalized with the local standard deviation). (g) As (a) but using randomized OLR data as input (see Section 4.2.2 for more details). (h) As (a) but replacing the last 20 days (from May 1 onwards) by zeros to mimic the effect of real-time monitoring. The example KW from Figure 4 is marked with a dashed line, and the stippled lines show the maximum and minimum phase speeds possible with this filter ( $8.9 \text{ m} \cdot \text{s}^{-1}$  and  $29.7 \text{ m} \cdot \text{s}^{-1}$ , respectively; see Section 4.1.2) [Colour figure can be viewed at [wileyonlinelibrary.com](http://wileyonlinelibrary.com)]





**FIGURE 7** Hovmoeller diagrams for February 20–May 20, 2009, filtered for Kelvin waves (KWs). National Oceanic and Atmospheric Administration outgoing long-wave radiation anomalies (twice daily) from the 2001–2018 deseasonalized climatology for (a) frequency–wave-number filtering using wavelets (FWF-Wavelet), (b) frequency–wave-number filtering using parabolic cylinder functions (FWF-PCF: PCF0 and PCF2), and (c) two-dimensional spatial projection using time-extended empirical orthogonal functions (2DS-EOF). The example KW from Figure 4 is marked with a dashed line, and the stippled lines show the maximum and minimum phase speeds possible with this filter ( $8.9 \text{ m}\cdot\text{s}^{-1}$  and  $29.7 \text{ m}\cdot\text{s}^{-1}$ , respectively; see Section 4.1.2) [Colour figure can be viewed at [wileyonlinelibrary.com](http://wileyonlinelibrary.com)]

are smoothed, as some wave energy cannot be represented when not considering the entire latitude circles. This particularly affects fast waves, whereas the influence on the MJO is usually small (Kikuchi, 2014). Projecting OLR onto the symmetric PCF0 and PCF2 before filtering (Figure 7b) also produces similar overall structures, but with differences in amplitude and regional distribution, resulting in a pattern correlation with FWF-FFT of only 0.46. Particularly over areas of off-equatorial convection, such as South America and the Atlantic, signals in FWF-PCF are weaker, indicating that the latitudinal average used in Figures 6a and 7a can contain contributions from PCFs other than PCF0 and PCF2 used here, whereas in theory PCF0 alone should be enough to represent KW patterns. The example KW highlighted in Figure 7 illustrates this effect, since KW convective activity over the eastern Pacific tends to follow the off-equatorial Intertropical Convergence Zone (Straub and Kiladis, 2002). Finally, the results based on 2DS-EOF (Figure 7c) show fundamentally different characteristics, leading to a pattern correlation with FWF-FFT of only 0.45. There is a general tendency towards smaller  $k$  (i.e., longer wavelength) and slower waves, some even close to the minimum possible phase speed of  $9 \text{ m}\cdot\text{s}^{-1}$  (stippled lines in Figure 7). The spatial projection appears to allow more localized changes in amplitude and wave speed than the FWF methods. This way, the KWs identified have more of an “MJO flavour” than for the other methods. Nevertheless, most of the strong KW anomalies, including

the highlighted example, are detected consistently by this method.

Figure 8 extends the analysis towards dynamical fields (wind and horizontal divergence at 850 and 200 hPa) using the FWF-PCF method. The results can be compared with the corresponding plot based on OLR (Figure 7b; marked as dashed lines in Figure 8). At 200 hPa (Figure 8a), zonal wind perturbations show some structural similarities to OLR in terms of  $k$  and phase speed, but there is a general tendency for the KWs to have higher amplitudes over the South American–Atlantic–African sector in contrast to the moisture-related fields. Maximum amplitudes reach  $5 \text{ m}\cdot\text{s}^{-1}$  in both directions, which is substantial relative to the raw fields (Figure 4h). The example KW is evident in 200 hPa zonal wind perturbations, but not as prominently as in latitudinally averaged OLR (Figure 6a) and with a phase shift by one-quarter wavelength. A corresponding diagram for horizontal divergence (Figure 8b) shows phase-shifted, overall consistent but also noisier patterns (in correspondence with the raw field shown in Figure 4i). Physically, one would expect a close relationship to OLR, but the pattern correlation with Figure 7b only amounts to  $-0.45$ . Even though the correlation is moderate, there are several occurrences of a nearly perfect match between OLR negative and divergence at 200 hPa positive anomalies. Results for 850 hPa (Figure 8c,d) show some structural consistency with the corresponding 200 hPa fields, but the amplitude is about three times smaller. Theoretically, one

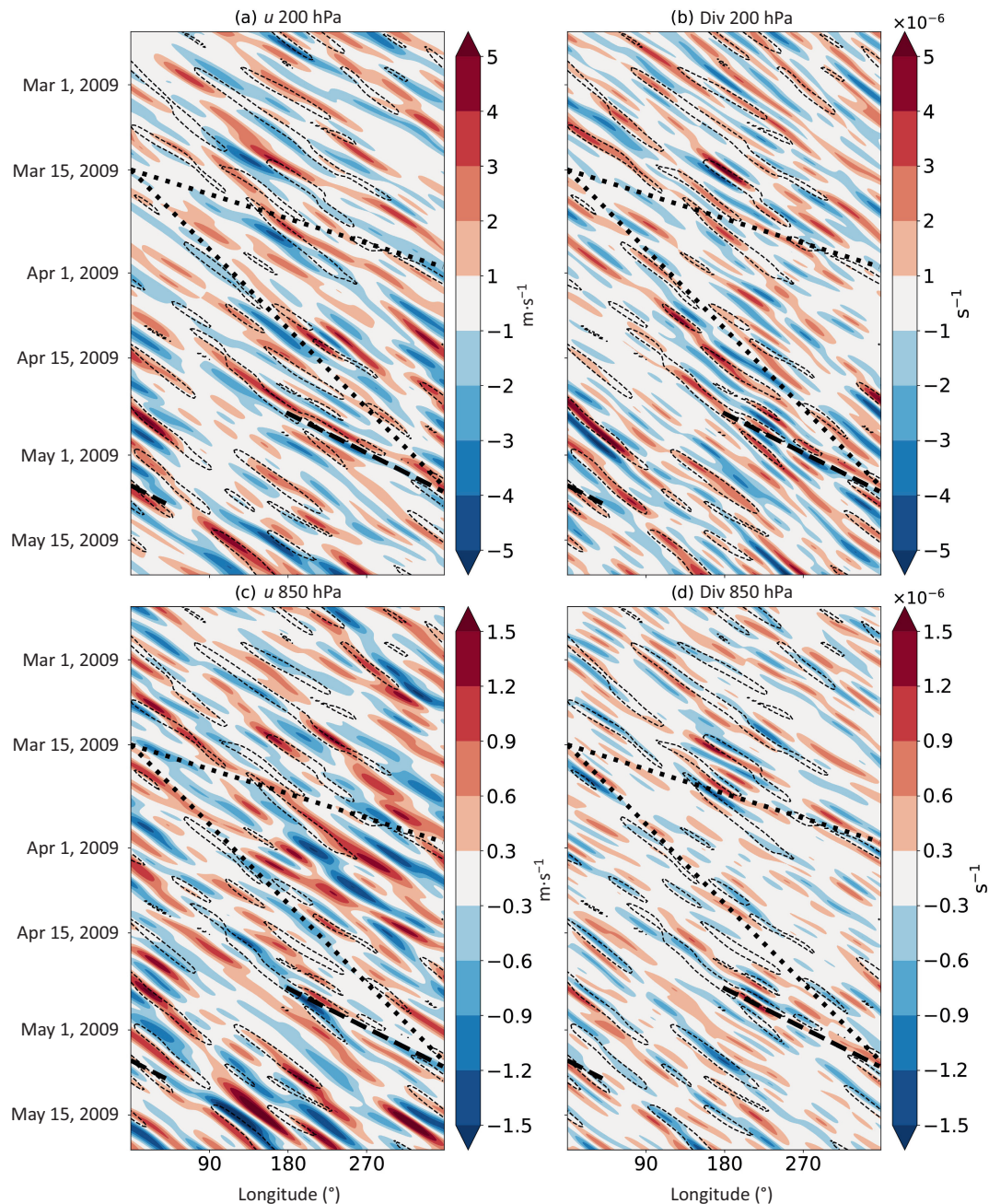


**FIGURE 8** Hovmoeller diagrams for February 20–May 20, 2009, filtered for Kelvin waves (KWs) using the frequency–wave-number filtering using parabolic cylinder functions (PCFs) method (PCF0 and PCF2). Anomalies from the 2001–2018 deseasonalized climatology for (a) zonal wind and (b) horizontal divergence at 200 hPa. (c, d) As (a) and (b) but for 850 hPa. All data are from ERA5 reanalysis (four times daily). The dashed lines show the  $-6 \text{ W}\cdot\text{m}^{-2}$  contour of outgoing long-wave radiation from Figure 7b. The example KW from Figure 4 is marked with a dashed line, and the stippled lines show the maximum and minimum phase speeds possible with this filter ( $8.9 \text{ m}\cdot\text{s}^{-1}$  and  $29.7 \text{ m}\cdot\text{s}^{-1}$ , respectively; see Section 4.1.2) [Colour figure can be viewed at [wileyonlinelibrary.com](http://wileyonlinelibrary.com)]

would expect opposite phases between the two levels, but the pattern correlation for zonal wind only reaches  $-0.06$ . The example KW is barely evident in 850 hPa zonal wind and divergence, possibly because there is more noise at this level.

Finally, Figure 9 compares KW zonal winds using FWF-PCF with those based on 2DS-PCF and 3DS-HF.

Recall that though 2DS-PCF projects each variable and vertical level separately, 3DS-HF projects three-dimensional fields of wind and geopotential together, but only the zonal wind signal is shown here. As already discussed, filtering based on FWF-PCF (Figure 9a) shows robust signals at 200 hPa, but those at 850 hPa are relatively weak and the phase relationship to 200 hPa is variable. The two



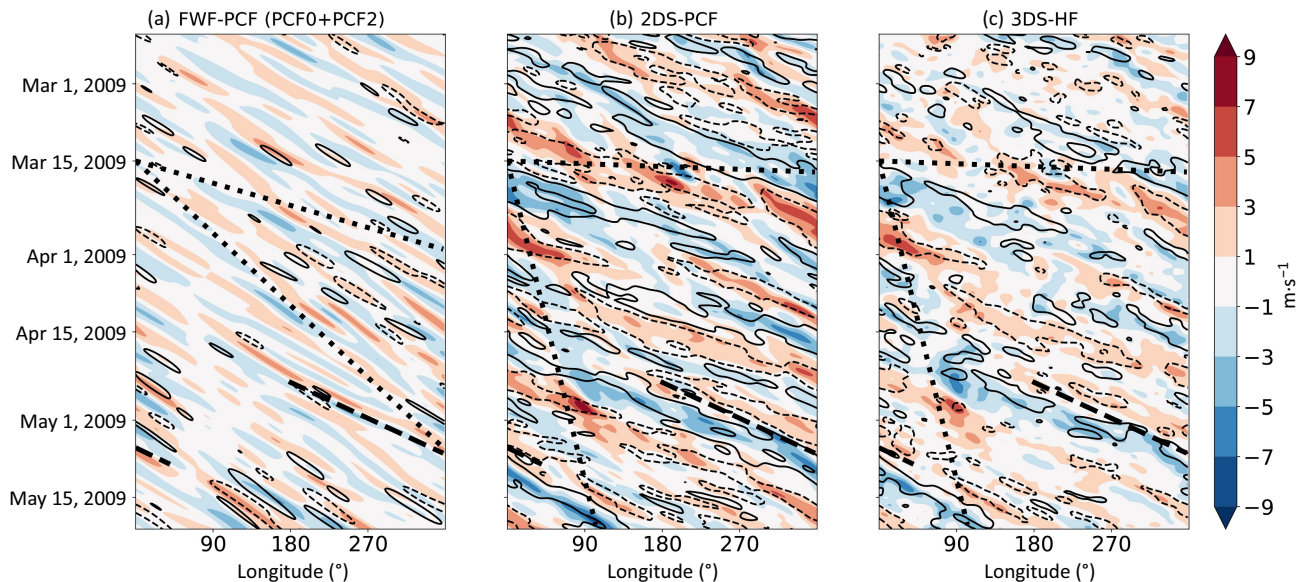


**FIGURE 9** Hovmoeller diagrams for February 20–May 20 2009 filtered for Kelvin waves (KWs). Zonal wind at 200 hPa (shading) and 850 hPa (solid and dashed contours at  $\pm 1 \text{ m}\cdot\text{s}^{-1}$ ) using the methods (a) frequency–wave-number filtering using parabolic cylinder functions (FWF-PCF: PCF0 and PCF2; as in Figure 8a,c), (b) two-dimensional spatial projection using PCFs (2DS-PCF), and (c) three-dimensional spatial projection using Hough functions (3DS-HF). The example KW from Figure 4 is marked with a dashed line. The stippled lines show the maximum and minimum phase speeds possible with the applied time–space filters (see Section 4.1.2):  $8.9 \text{ m}\cdot\text{s}^{-1}$  and  $29.7 \text{ m}\cdot\text{s}^{-1}$ , respectively, for FWF-PCF and  $2 \text{ m}\cdot\text{s}^{-1}$  and  $231.9 \text{ m}\cdot\text{s}^{-1}$ , respectively, for 2DS-PCF and 3DS-HF [Colour figure can be viewed at [wileyonlinelibrary.com](http://wileyonlinelibrary.com)]

projection methods (Figure 9b,c) show fundamentally different KW anomalies characterized consistently by smaller  $k$  (similar to 2DS-EOF applied to OLR; see Figure 7c) but faster propagation (in contrast to 2DS-EOF; note the much wider range of possible phase speeds indicated by the stippled lines in Figure 9b,c than in Figure 9a). As for 2DS-EOF, the projection allows for more abrupt changes in both time and longitude. Pattern correlations for 200 hPa zonal wind amount to 0.18 (FWF-PCF vs. 2DS-PCF), 0.14 (FWF-PCF vs. 3DS-HF), and 0.84 (2DS-PCF vs. 3DS-HF). The agreement between the latter two is remarkable given the different treatment of vertical and meridional structure (see Section 3). 3DS-HF, which uses a superposition of 27  $D$  values and applies time filtering after the spatial projection, appears to generate more small-scale features than 2DS-PCF does. The multivariate approach is one reason contributing to this. 2DS-PCF has the largest amplitude of the three methods shown in Figure 9 at both levels. This suggests that KWs with different vertical structures contribute to the total KW signal, another potential reason for the more patchy structure in Figure 9c. Both projection methods show a relatively clear out-of-phase relationship between the winds at 200 and 850 hPa, as expected for a first baroclinic mode in the vertical (pattern correlations are  $-0.59$  for 3DS-HF and  $-0.60$  for 2DS-PCF). The example KW in the Western hemisphere and over Africa is evident in both methods, straddling positive and negative wind anomalies, as theory predicts.

To better understand the three-dimensional structure and propagation behaviour of the example KW, Figure 10 shows vertical and horizontal sections using the methods 3DS-HF (Figure 10a,c,e,g) and 2DS-PCF (Figure 10b,d,f,h). Both methods show a well-developed KW stretching from the Indian Ocean to the central Pacific. Owing to the chosen trapping scale  $y_0$  of  $6^\circ$  in 2DS-PCF, horizontal patterns are largely confined to the inner Tropics (Figure 10b,d), while stretching further poleward in 3DS-HF (Figure 10a,c). A fairly clear correspondence between wind and geopotential is seen in both methods despite the multivariate versus univariate projection (see Section 3 for details). Averaging zonal winds latitudinally from  $15^\circ \text{ S}$  to  $15^\circ \text{ N}$  reveals the vertical structures of the waves (Figure 10e–h). Overall the two methods yield consistent results on both days. The most conspicuous signal is the strongly tilted, positive zonal wind anomaly over the Indian Ocean that stretches from the upper troposphere deep into the stratosphere. Given the marked background easterlies in this region (Figure 5), the KW signal propagates rather slowly from April 29 to May 1, 2009, while weakening somewhat. In contrast, the corresponding negative anomaly further east propagates much faster through the region of mean upper-level westerlies over the Pacific. The vertical structure is to first order consistent with a first baroclinic mode.

We can conclude from this analysis that the different methods and input data used lead to considerable

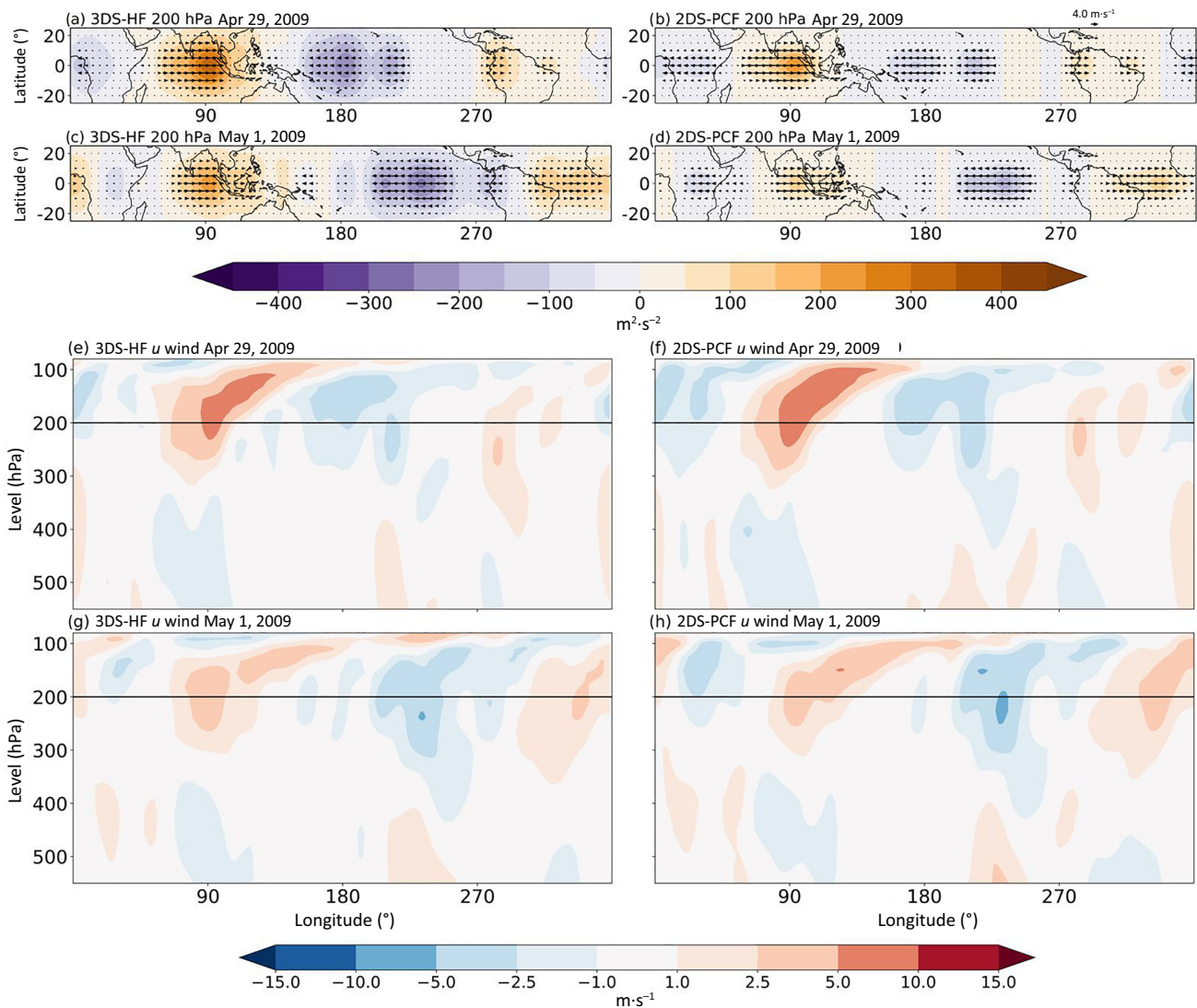


**FIGURE 10** Vertical and horizontal structures of Kelvin waves (KWs) on April 29 and May 1, 2009, based on (a, c, e, g) three-dimensional spatial projection using Hough functions (3DS-HF) and (b, d, f, h) two-dimensional spatial projection using parabolic cylinder functions (2DS-PCF). Bottom plots show vertical cross-sections in the upper troposphere of meridionally ( $15^{\circ}$  S– $15^{\circ}$  N) averaged KW filtered zonal wind. Top plots show corresponding horizontal sections at the 200 hPa level (marked with black lines in the bottom panels) with wind vectors and geopotential [Colour figure can be viewed at [wileyonlinelibrary.com](http://wileyonlinelibrary.com)]

structural differences as reflected in  $k$ , phase speed, amplitude, and longitudinal variations. Though FWF methods show good structural agreement amongst each other, there are fundamental differences from projection methods, which tend towards lower  $k$  and can accommodate more abrupt changes and a much wider range of phase speeds. As expected, there are also marked differences between “moist” and “dry” variables and between vertical levels. Nevertheless, most methods and data detected the long-lived and high-amplitude KW during late April to early May. This feature is generally less clear in FWF-PCF, possibly due to off-equatorial convection, and at 850 hPa where amplitudes tend to be small (with the exception of zonal wind in 2DS-PCF).

#### 4.2.3 | Mixed Rossby-gravity waves

This section compares Hovmoeller depictions of (westward-propagating) MRG waves based on different datasets and methods. Given the insights gained from the KW analysis, we will restrict the investigation to anomalies of OLR and full-field meridional wind. According to linear theory, MRGs are characterized by antisymmetric structures in zonal wind and geopotential in quadrature to divergence (and thus OLR if convectively coupled), as well as by a strong, symmetric, cross-equatorial flow collocated longitudinally with the extrema in divergence. MRGs propagate westward but have an eastward group velocity. For example, see Kiladis *et al.* (2009) for more details.



Figure 11 shows MRG anomalies obtained from the six different EW identification methods. Generally, there are large and potentially consequential differences between the FWF and the projection methods. Given that boreal spring is not a prime season for convectively coupled MRGs, the FWF methods applied to OLR (Figure 11a,b) show low-amplitude (order  $\pm 5 \text{ W}\cdot\text{m}^{-2}$ ) signals throughout the study period over most of the domain that are only marginally stronger than those generated from randomized fields (not shown; see previous section for details on how these are generated). As for KWs, the use of wavelets instead of FFT leads to similar structures but lower amplitude (cf. Figure 11a with Figure 11b, pattern correlation 0.85). Applying FWF methods to CERES and IMERG produces largely similar results, but with the latter emphasizing areas of warm sea-surface temperatures (not shown). Using 2DS-EOF, in contrast, yields higher amplitudes and slower propagation with a more localized structure (Figure 11c). Recall that 2DS-EOF uses a 2–10-day westward filter window instead of the much narrower one of FWF-FFT (see Figure 1). Pattern correlation of 2DS-EOF with FWF-FFT is only 0.07, indicating no relation between the approaches despite the same input fields.

For 200 hPa meridional wind perturbations, the FWF-PCF approach (using the symmetric PCF0 and PCF2, Figure 11d) yields a result similar in structure to OLR using FWF-FFT. Amplitudes are on the order of few metres per second at best, with a tendency to even faster waves than in Figure 11a. The corresponding wave signals at 850 hPa (contours in Figure 11d) are very weak and noisy. In stark contrast, 2DS-PCF (Figure 11e) shows well-developed MRG signals in 200 hPa meridional wind over the Pacific during the first 2 months of the study period. Amplitudes reach  $\pm 10 \text{ m}\cdot\text{s}^{-1}$  and the wave signal lasts for 2–3 weeks. Propagation is much slower than in the FWF methods with some similarities to 2DS-EOF, particularly over the Pacific, where strong westerlies may slow down the wave propagation (see Figure 5). There is also some evidence in Figure 11e for an eastward group velocity, as linear theory predicts. Pattern correlation with FWF-PCF is only 0.27, reflecting the fundamentally different approaches despite using the same input field. Corresponding signals at 850 hPa are generally noisier, with an unclear phase relationship to 200 hPa. The faster propagation at this level is consistent with a Doppler shift in the low-level easterlies (see Figure 5). Finally, 3DS-HF (Figure 11f) shows some similarities in amplitude and phase speed to 2DS-PCF (pattern correlation 0.66), but the wave signal is more patchy and less confined to the Pacific than for 2DS-PCF. Individual signals last up to about a week, and their  $k$  values are higher than for other methods. The movement is hard to interpret, as the signals appear as a mixture of eastward- and westward-moving

features. Amplitudes at 850 hPa are slightly larger than for the 2DS-PCF projection, but again dominated by higher  $k$  values. The peak of MRG activity at synoptic zonal scales evident from Figure 11f is a property of the average MRG variance spectra in the troposphere, as discussed by Stephan *et al.* (2021).

The dashed lines in all panels of Figure 11 mark the MRG example discussed in Section 4.2.1. This feature stands out clearly in 2DS-PCF and 3DS-HF, and to a lesser extent in 2DS-EOF (noting that OLR rather than  $v$  is shown in Figure 11c), but is more or less absent in the other approaches. One possible reason is that the MRG identified is not strongly coupled to convection, leaving little signal in OLR. This, however, cannot explain the weak signal in FWF-PCF when applied to meridional wind. The slow phase speed found in 2DS-PCF and 3DS-HF exceeds the minimum speed compatible with the filter windows used for FWF (stippled lines in Figure 11a,b,d). However, given that the dominant  $k$  is about 5, the FWF filter likely suppresses most of these signals (see Figure 1). It is also possible that the strongly longitudinally confined wave signal is not well represented in FWF. These results suggest that there are coherent MRG-like spatial patterns, whose Doppler-shifted propagation behaviour, however, is incompatible with the FWF assumptions. The 3DS-HF results suggest little coherence in time when a larger spectrum of three-dimensional modes is considered, which could be an indicator of strong MRG wave dispersion.

Finally, Figure 12 shows vertical and horizontal sections as in Figure 10. Both the 3DS-HF and 2DS-PCF methods show a well-developed MRG wave over the Pacific with some link across South America into the Atlantic, as well as a some more confined activity over the Indian Ocean (Figures 12a–d). As for the KW (Figure 10), horizontal patterns in 2DS-PCF are more trapped than those in 3DS-HF and a clear correspondence between wind and geopotential is evident. Overall structures in  $15^\circ\text{S}$  to  $15^\circ\text{N}$  averaged meridional winds (Figures 12e–h) are consistent but 3DS-HF tends to have less deep, higher-amplitude signals over the Pacific, in contrast to a deeper structure over the Indian Ocean. 3DS-HF also appears to have more variable propagation of individual wave maxima. Both methods show some weak eastward tilt with height over the Pacific, in the same direction as the strong vertical shear in the Walker Cell (Figure 5).

#### 4.2.4 | Equatorial Rossby waves

This section closes the case study with a corresponding analysis of ERs with the meridional mode number  $n = 1$ . According to linear theory, these ERs are characterized by symmetric structures in geopotential, divergence,

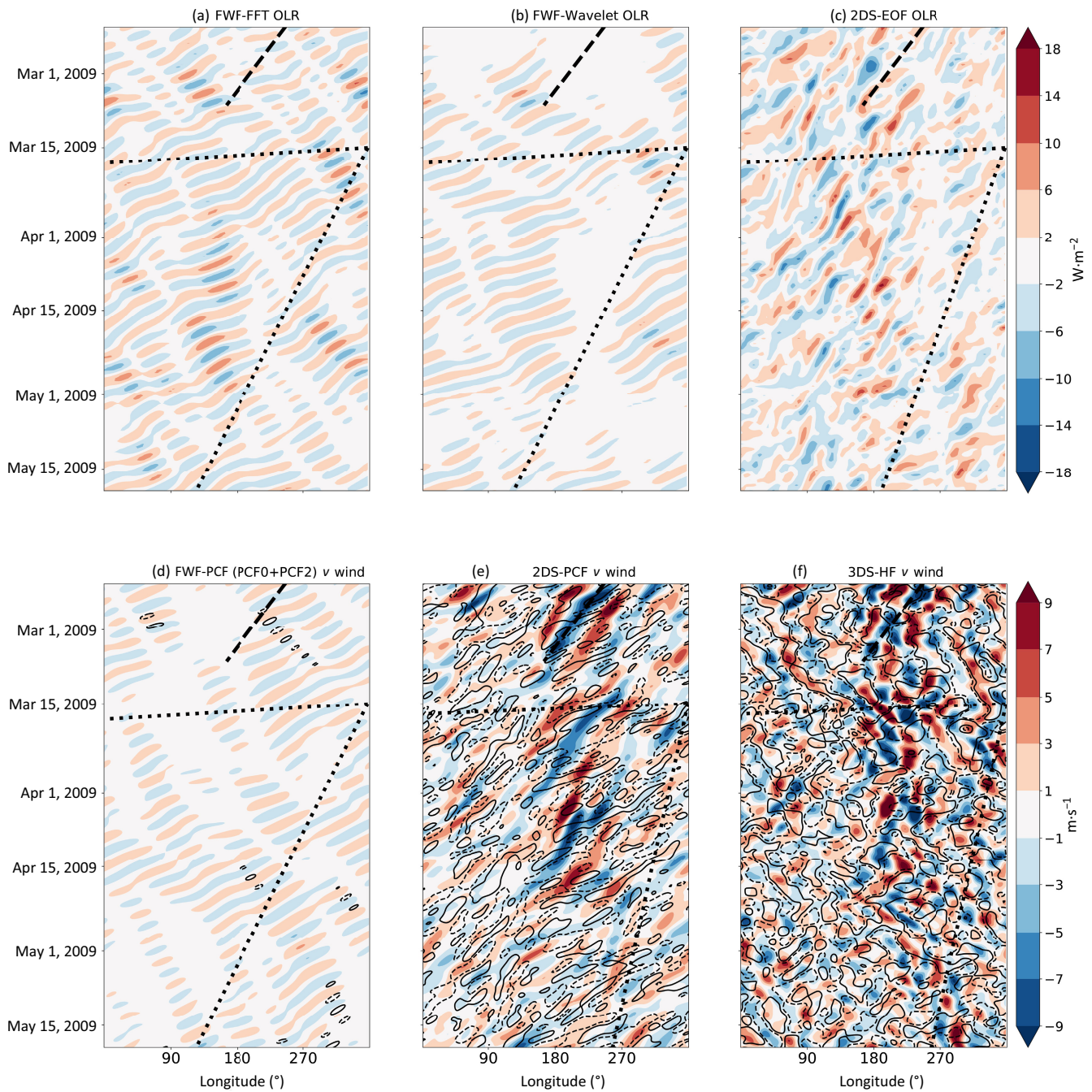


**FIGURE 11** Hovmoeller diagrams for February 20–May 20, 2009, filtered for mixed Rossby–gravity waves (MRGs). National Oceanic and Atmospheric Administration outgoing long-wave radiation (OLR) anomalies (twice daily) from the 2001–2018 deseasonalized climatology using the methods (a) frequency–wave-number filtering using fast Fourier transform (FWF-FFT), (b) frequency–wave-number filtering using wavelets (FWF-Wavelet; both antisymmetric latitudinal averaging), and (c) two-dimensional spatial projection using time-extended empirical orthogonal functions (2DS-EOF); meridional wind at 200 hPa (shading) and 850 hPa (solid and dashed contours at  $\pm 0.7 \text{ m}\cdot\text{s}^{-1}$ ) using the methods (d) frequency–wave-number filtering using parabolic cylinder functions (FWF-PCF: PCF0 and PCF2), (e) two-dimensional spatial projection using PCFs (2DS-PCF), and (f) three-dimensional spatial projection using Hough functions (3DS-HF). The example MRG from Figure 4 is marked with a dashed line. The stippled lines show the maximum and minimum phase speeds possible with the applied time–space filters (see Section 4.1.2):  $-4.6 \text{ m}\cdot\text{s}^{-1}$  and  $-185.5 \text{ m}\cdot\text{s}^{-1}$ , respectively, for all FWF methods,  $-3.3 \text{ m}\cdot\text{s}^{-1}$  and  $-231.9 \text{ m}\cdot\text{s}^{-1}$ , respectively, for 2DS-EOF, and  $-2 \text{ m}\cdot\text{s}^{-1}$  and  $-231.9 \text{ m}\cdot\text{s}^{-1}$ , respectively, for 2DS-PCF and 3DS-HF [Colour figure can be viewed at [wileyonlinelibrary.com](http://wileyonlinelibrary.com)]

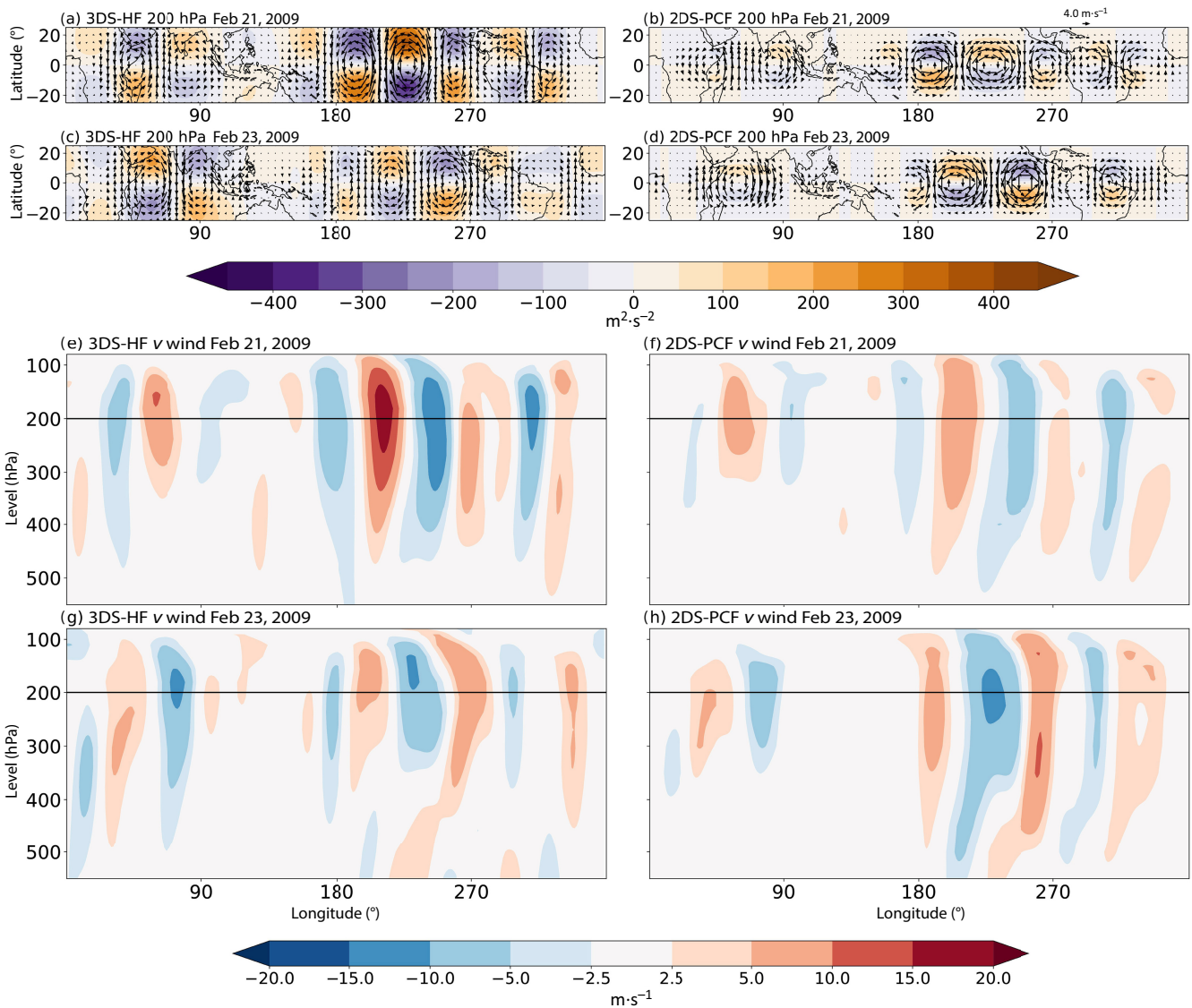


**FIGURE 12** Vertical and horizontal structures of mixed Rossby–gravity waves (MRGs) on February 21 and 23, 2009, based on (a, c, e, g) three-dimensional spatial projection using Hough functions (3DS-HF) and (b, d, f, h) two-dimensional spatial projection using parabolic cylinder functions (2DS-PCF). Bottom plots show vertical cross-sections in the upper troposphere of meridionally ( $15^{\circ}$  S– $15^{\circ}$  N) averaged MRG-filtered meridional wind. Top plots show corresponding horizontal sections at the 200 hPa level (marked with black lines in the bottom panels) with wind vectors and geopotential [Colour figure can be viewed at [wileyonlinelibrary.com](http://wileyonlinelibrary.com)]

and zonal wind as well as antisymmetric meridional wind perturbations with off-equatorial maxima. There is strong zonal flow along the Equator and opposite perturbations in the outer Tropics. OLR anomalies typically maximize between the off-equatorial vortices out of phase (in phase) with the low-level meridional wind in the Northern Hemisphere (Southern Hemisphere). ERs propagate slowly westward and are thus more strongly affected by Doppler shifts than KWs and MRGs are. For example, see Kiladis *et al.* (2009) for more details. Given the complex structure of ERs, we will show results for OLR and IMERG, as well as zonal and meridional winds.

Figure 13 shows in total 12 different depictions of ERs ( $n = 1$ ) using different methods and input data. The example ER discussed in the context of Figure 4 is indicated in all panels. OLR-based methods (Figure 13a–d) consistently show marked ER activity over the Indian Ocean and Maritime Continent with amplitudes well above  $\pm 10 \text{ W}\cdot\text{m}^{-2}$ . Structural agreement between FWF-FFT (Figure 13a) and FWF-Wavelet (Figure 13b) is high, with a pattern correlation of 0.97, but somewhat reduced amplitude in FWF-Wavelet, as already discussed for KW and MRG. FWF-PCF (Figure 13c) has a fairly high pattern correlation with FWF-FFT of 0.71, but amplitudes are markedly reduced and there are some minor



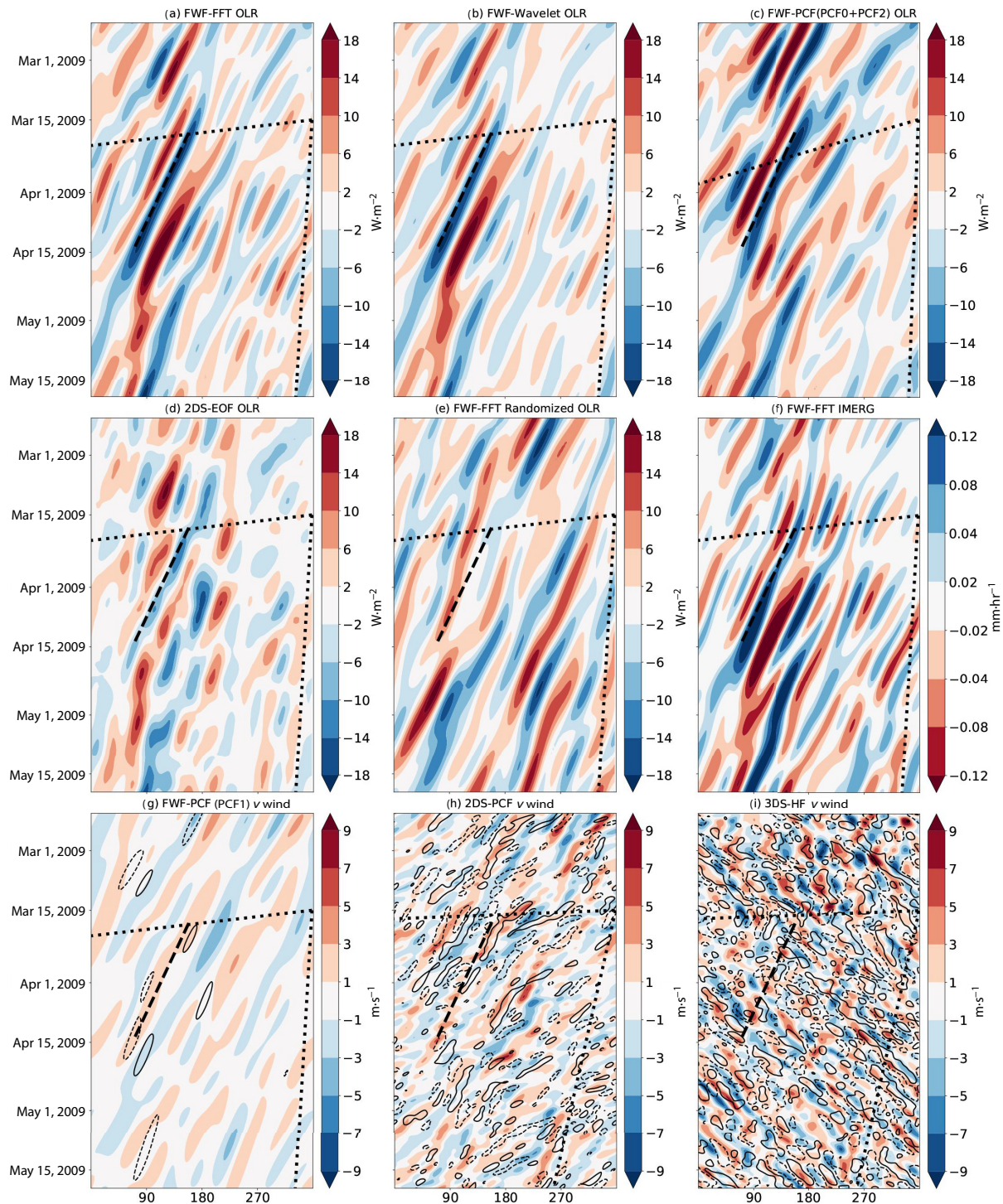


**FIGURE 13** Hovmoeller diagrams for February 20–May 20 2009 filtered for equatorial Rossby waves (ERs;  $n = 1$ ). National Oceanic and Atmospheric Administration outgoing long-wave radiation (OLR) anomalies (twice daily) from the 2001–2018 deseasonalized climatology using (a) frequency–wave-number filtering using fast Fourier transform (FWF-FFT), (b) frequency–wave-number filtering using wavelets (FWF-Wavelet), (c) frequency–wave-number filtering using parabolic cylinder functions (FWF-PCF: PCF0 and PCF2), and (d) two-dimensional spatial projection using time-extended empirical orthogonal functions (2DS-EOF). (e) As (a) but for randomized OLR data (see Section 4.2.2 for details). (f) As (a) but for the Integrated Multi-Satellite Retrievals for Global Precipitation Measurement (IMERG) precipitation. (g–i) Meridional and (j–l) zonal wind at 200 hPa (shading) and 850 hPa (solid and dashed contours at  $\pm 1 \text{ m s}^{-1}$ ) using the methods (g, j) FWF-PCF for (g) PCF1 and (j) PCF0 and PCF2, (h, k) 2DS-PCF, and (i, l) three-dimensional spatial projection using Hough functions (3DS-HF). The example ER from Figure 4 is marked with a dashed line. The stippled lines show the maximum and minimum phase speeds possible with the applied time-space filters (see Section 4.1.2):  $-0.5$  to  $-74.2 \text{ m s}^{-1}$  for all FWF methods,  $-0.3$  to  $-30.9 \text{ m s}^{-1}$  for 2DS-EOF, and  $-2$  to  $-231.9 \text{ m s}^{-1}$  for 2DS-PCF and 3DS-HF [Colour figure can be viewed at [wileyonlinelibrary.com](http://wileyonlinelibrary.com)]



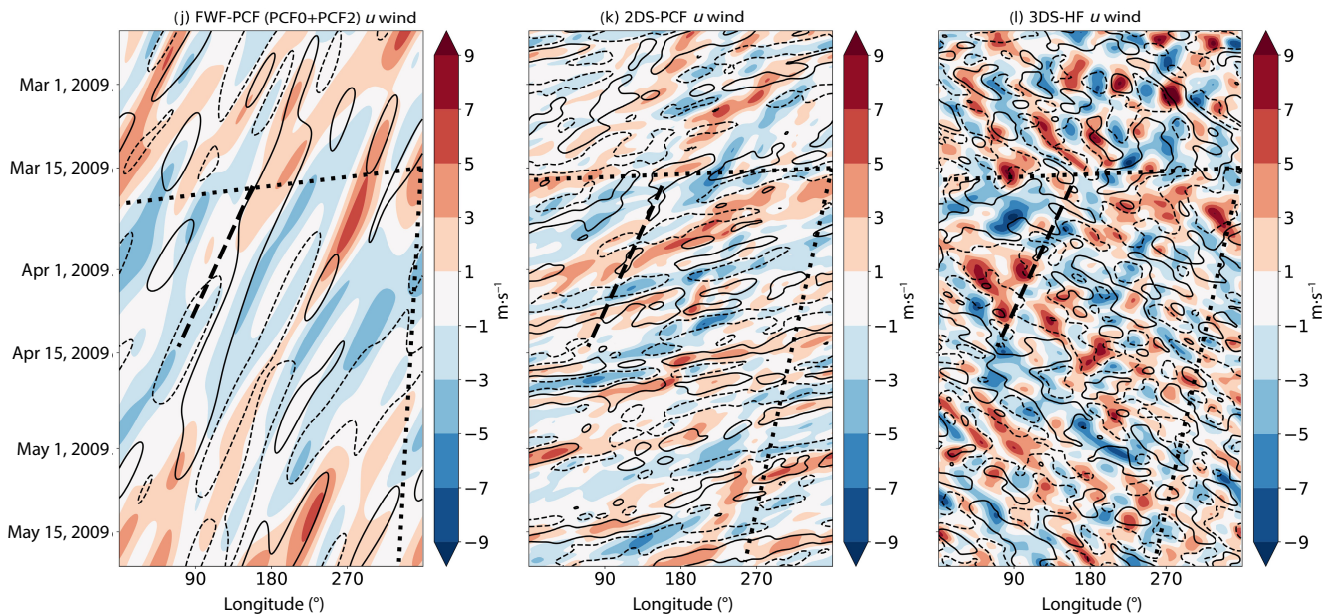


**FIGURE 13** (Continued)

structural differences. As we use the symmetric PCF0 and PCF2 (see Figure 2d) here, the lower amplitude may indicate that asymmetric signals or signals contained in higher-order PCFs are missed. It is also possible that a larger trapping scale would pick up more of the ER signal, since these waves tend to have a wider meridional extent than KW and MRG do. In 2DS-EOF (Figure 13d), similar larger-scale structures are evident, but signals tend to be more localized with indications for an eastward group velocity, leading to a pattern correlation with FWF-FFT of only 0.55. The example ER highlighted in all panels of Figure 13 is less prominent in 2DS-EOF than in the other OLR-based methods.

Figure 13e corresponds to Figure 13a but uses randomized OLR data as in Figure 6g. It is a strong demonstration of how the time-space filter isolates seemingly propagating features despite the randomized phases. The phase speeds apparent from Figure 13e appear largely consistent with the real data shown in Figure 13a. Maximum amplitudes are lower than that of the real-world ER highlighted with a black line, but not by a large margin, whereas the observed longitudinal differences disappear through the randomization. The pattern correlation of  $-0.07$  between the two Hovmoeller plots probably is a reflection of the reduced effective degrees of freedom due to the slow propagation of ERs. This effect is also evident in the padded-zeros experiment we conducted in analogy to Figure 6h, where correlations to the full-data analysis drop about 1 week earlier than for the fast KW (not shown). Finally, when applying FWF-FFT to IMERG instead of OLR (Figure 13f), similar structures emerge, leading to a pattern correlation of  $-0.87$  after remapping to

the OLR resolution, substantially higher than that for the KW (Figure 6).

For meridional wind, more dramatic differences between the methods become evident. For FWF-PCF (Figure 13g) spatial structures and propagation behaviour at 200 hPa overall agree with the FWF results based on OLR, but the amplitude is rather small. Signals at 850 hPa are hardly discernible. 2DS-PCF (Figure 13h) shows smaller-scale structures with higher amplitudes at both levels (resulting in a pattern correlation with FWF-PCF of 0.37 at 200 hPa). Some correspondence with the OLR signals is evident. The example ER is discernible at 200 hPa but hardly at 850 hPa. Finally, using 3DS-HF (Figure 13i), wave signals at both levels have larger amplitudes and smaller zonal scales, thus appearing more patchy. Coherent structures show a tendency to move eastward rather than westward. This demonstrates the complex dynamics of dispersive ERs propagating in temporally and spatially varying background flow when no hard constraint on propagation direction is imposed, as in all the other methods. The pattern correlation of 3DS-HF is 0.27 to FWF-PCF and 0.44 to 2DS-PCF.

Zonal wind differences between the three methods are even more pronounced. Pattern correlations at 200 hPa only amount to 0.18 (FWF-PCF to 2DS-PCF), 0.21 (FWF-PCF to 3DS-HF), and 0.41 (2DS-PCF to 3DS-HF). Using FWF-PCF (now based on the symmetric PCF0 and PCF2; Figure 13j), ERs reach fairly high amplitude (more than  $\pm 5 \text{ m s}^{-1}$  at 200 hPa); their propagation characteristics are similar to the meridional wind signals (Figure 13g) but the structures identified have a tendency towards lower  $k$ . The phase shift between zonal and meridional

wind is evident for some of the more developed signals, and the phase relationship to the example wave identified from OLR changes during its lifetime. A similar correspondence between zonal and meridional wind patterns is found for 3DS-HF (Figure 13l), which also shows a relatively clear out-of-phase behaviour between 200 and 850 hPa, indicating a first baroclinic vertical structure. Recall that, in this method, projections are not done separately for vertical levels. Somewhat surprisingly, however, results using 2DS-PCF (Figure 13k) reveal much faster signals in zonal than in meridional wind. Some of these structures (e.g., the positive signal during late March and early April) are also visible in 3DS-HF. A potential reason for this unexpected behaviour is that ERs have a large zonal wind signal at the Equator, which projects very strongly onto  $k = 2$  such that this wave number can dominate more easily over higher  $k$  values than for the ER (or MRG) meridional wind.

Looking at horizontal and vertical sections for the example ER wave (Figure 14; analogous to Figures 10 and 12) also reveals some marked differences between 3DS-HF and 2DS-PCF. The former (Figures 14a and c) produces higher amplitude signals in both wind and geopotential with a greater  $k$  and stretching farther into the subtropics (as already observed for KW and MRG). The latter (Figures 14b and d) reveals the dominance of the  $k = 2$  zonal wind signal mentioned in the previous paragraph. The emphasis on different patterns is also strongly reflected in the propagation behaviour. As 3DS-HF generally includes both west- and eastward moving waves, the overall signals move only slowly westward or even eastward, while 2DS-PCF suggests a fast westward propagation consistent with the dominance of the  $k = 2$  structure. However, vertical sections of meridional wind (Figures 14e–h) indicate higher  $k$  structures and relatively slow propagation in both methods. Compared to the nearly equivalent barotropic vertical structure in 3DS-HF, the 2DS-PCF waves are weaker and less vertically coherent. This analysis suggests that the full complexity of three-dimensional normal modes is useful to represent the diverse structures of ER and their non-trivial propagation behaviour in a non-resting background flow. Meridional winds are appropriate to represent these diverse structures using 2DS-PCF, as  $v$  is a component of only PCF1. Using zonal wind instead must be treated with caution, as  $u$  is a linear combination of PCF0 and PCF2.

### 4.3 | Climatological analysis

In this section, the climatological behaviour of five of the six EW identification methods (all but 3DS-HF) will be compared over the entire 2001–2018 period. The input

fields OLR and zonal and meridional wind at 200 and 850 hPa are first deseasonalized using the first three harmonics of the annual cycle and are then averaged from 15° S–15° N and on a daily basis. Finally, the total variance over time is computed for each longitude. Daily averages are preferred here to six-hourly data to allow a fair comparison between land areas with strong diurnal cycles and ocean areas. This raw unfiltered variance is then correlated with the corresponding variance associated with the different EW types. The square of the correlation coefficient is a measure of the explained variance (usually expressed as a percentage). Assuming independence between individual EWs, the explained variances can be stacked on top of each other to create a “variance budget” plot, as in Schlueter *et al.* (2019a). The sum of the individual terms can be understood as the maximum explained variance by all wave types analysed, as no wave interactions are taken into account. In the following we will discuss results for both Equator-symmetric and -antisymmetric variance.

Figure 15 shows results based on OLR comparing four different methods. The unfiltered OLR variance (identical black lines in all panels of Figure 15) peaks between 60° and 160° E; that is, over the warm waters of the Indian Ocean and West Pacific Ocean. Smaller local maxima occur over the African and South American continents. According to FWF-FFT (Figure 15a) KWs contribute around 15% to OLR variability throughout most of the tropical belt, with a minimum over the Indian Ocean and a maximum over Africa. ER ( $n = 1$ ) contributions are also substantial, particularly over the Indian and Pacific oceans, with somewhat reduced contributions over Africa and the Maritime Continent. The MJO, defined as in Kiladis *et al.*, 2009, dominates explained variance over the Indian Ocean, where the three wave types taken together reach a value of more than 60%. High contributions continue eastward until the Date Line, reducing to about 5% in the Western Hemisphere and over Africa. Consistent with the Hovmoeller plots in the previous sections, differences between FWF-FFT and FWF-Wavelet (Figure 15b) are small. Interestingly, however, the latter produces slightly higher values of explained variance overall, indicating that, although the wavelets tend to generate lower amplitudes in the Hovmoeller diagrams (see previous sections), correlations with the local background are higher, as they can better resolve longitudinally confined signals. The opposite behaviour is found for FWF-PCF (here again using the two symmetric PCF0 and PCF2; Figure 15c). The overall structures are again similar to the other FWF methods, but values of explained variance tend to be lower, particularly for KWs over the eastern Pacific, where off-equatorial convection cannot be represented well with the PCFs. In contrast, ER contributions over the Pacific are slightly larger, indicating cancellation

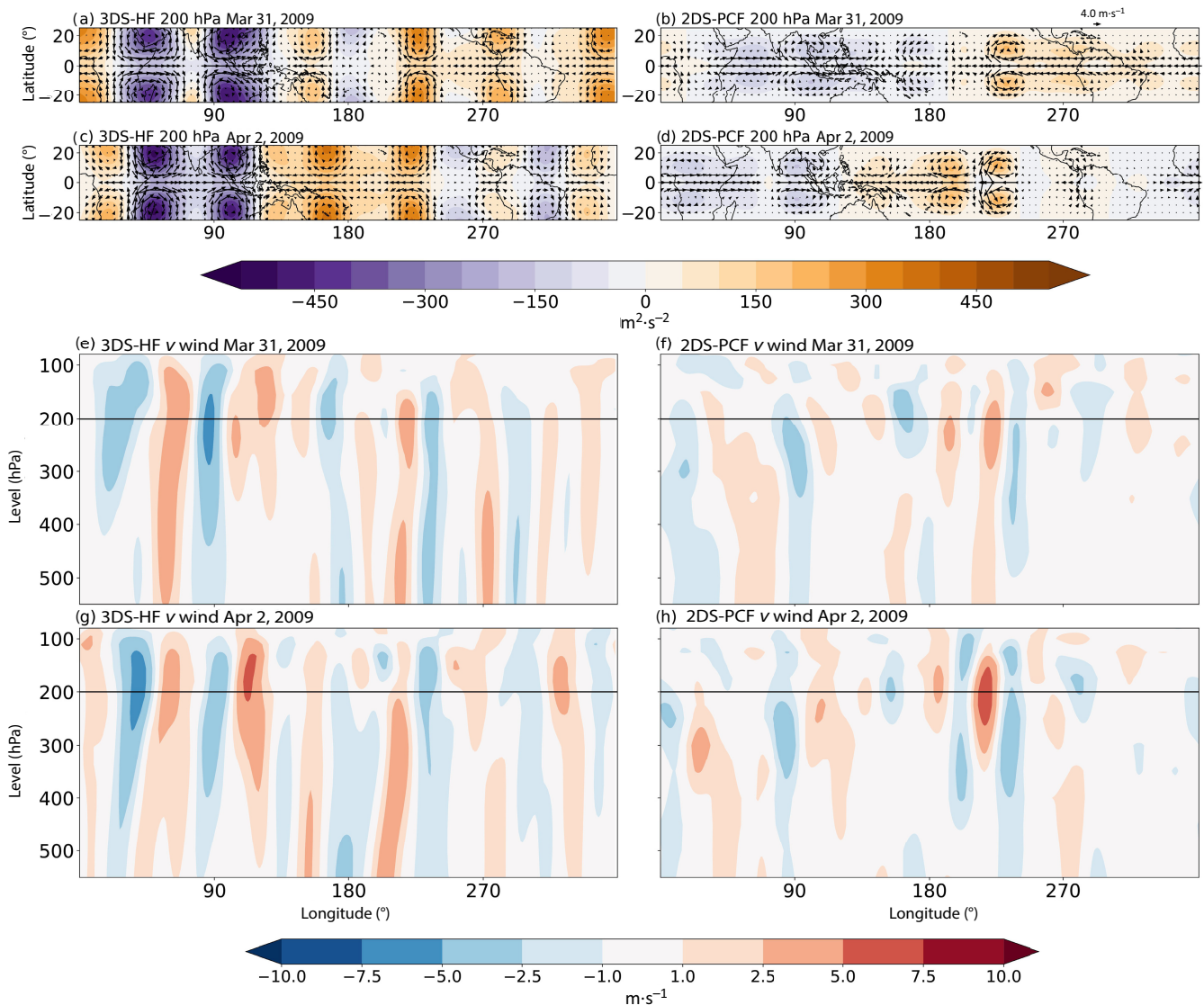


**FIGURE 14** Vertical and horizontal structures of equatorial Rossby waves (ERs;  $n = 1$ ) on March 31 and April 2, 2009, based on (a, c, e, g) three-dimensional spatial projection using Hough functions (3DS-HF) and (b, d, f, h) two-dimensional spatial projection using parabolic cylinder functions (2DS-PCF). Bottom plots show vertical cross-sections in the upper troposphere of antisymmetrically ( $15^{\circ}$  S– $15^{\circ}$  N) averaged ER-filtered meridional wind. Top plots show corresponding horizontal sections at the 200 hPa level (marked with black lines in the bottom panels) with wind vectors and geopotential [Colour figure can be viewed at [wileyonlinelibrary.com](http://wileyonlinelibrary.com)]

effects in the simple latitudinal averages. Finally, using 2DS-EOF yields markedly different longitudinal structures and overall smaller explained variance (Figure 15d). KWs contribute everywhere in the Tropics with several local peaks, whereas contributions from ERs and the MJO are largely restricted to the area of maximum raw variance over the Indian Ocean and West Pacific Ocean, suggesting that the high variance there dominates the EOF computation used in 2DS-EOF.

Figure 16 shows the corresponding results for winds at 200 hPa and 850 hPa using the methods FWF-PCF (as in Figure 15c) and 2DS-PCF. The unfiltered variance in 200 hPa  $u$  (black lines in Figure 16a,b) has less stark

longitudinal contrasts compared with OLR (Figure 15) with peaks over the western Indian Ocean, the eastern Pacific and Africa. The FWF-PCF method (Figure 16a) finds a significant contribution of KWs everywhere in the tropical belt, which, however, is smaller than that for OLR (Figure 15c). In contrast, the contribution from ER ( $n = 1$ ) is relatively more important than for OLR, with local peaks corresponding to the maxima in the background variance, leading to a combined explained variance of more than 40% over the Indian Ocean. In contrast, the 2DS-PCF method (Figure 16b) yields a much larger influence of KWs than ERs with overall similar combined values of explained variance but less longitudinal structure.



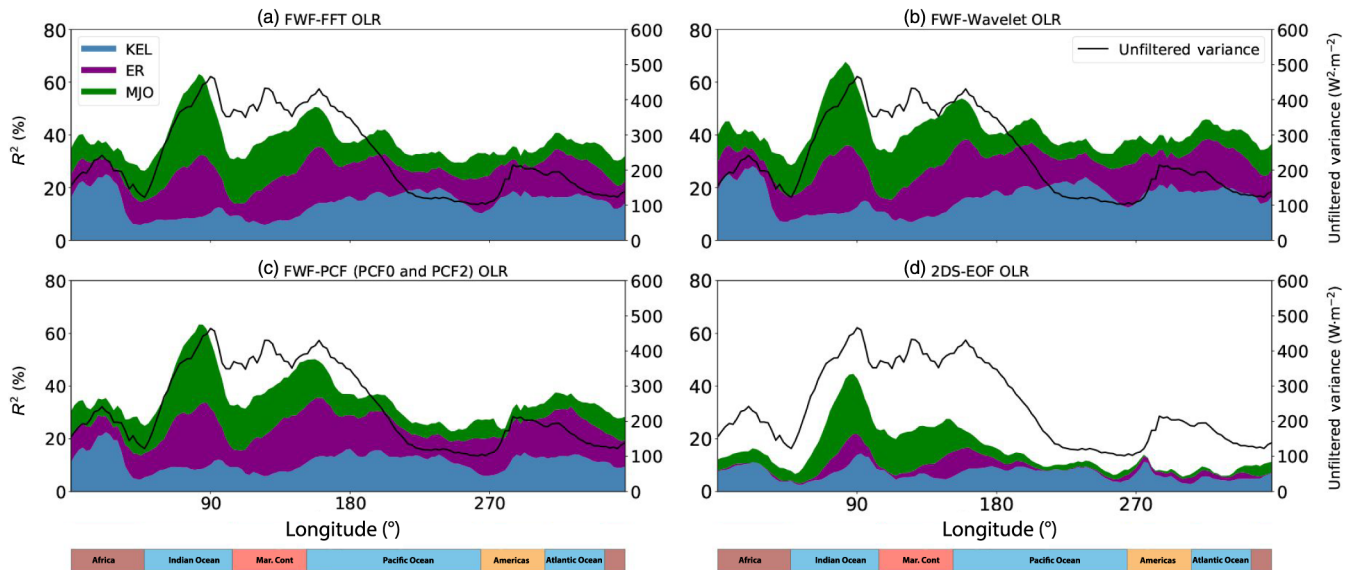


**FIGURE 15** Total (daily) symmetric variance (black lines, right axis) and fraction explained by individual wave types (in per cent, shadings, left axis) for 2001–2018. Based on National Oceanic and Atmospheric Administration outgoing long-wave radiation (OLR) and using the method (a) frequency–wave-number filtering using fast Fourier transform (FWF-FFT), (b) frequency–wave-number filtering using wavelets (FWF-Wavelet), (c) frequency–wave-number filtering using parabolic cylinder functions (FWF-PCF; using PCF0 and PCF2) and (d) two-dimensional spatial projection using time-extended empirical orthogonal functions (2DS-EOF). Note that, in 2DS-EOF, mixed Rossby–gravity wave (MRG) indicates “2–10 day westward”-propagating disturbances. All fields are averaged from 15° S to 15° N before the computation of variance and correlations [Colour figure can be viewed at [wileyonlinelibrary.com](http://wileyonlinelibrary.com)]

Additionally in this plot, we show the contribution of ER-E waves—that is, spatial patterns consistent with theoretical ER structures that propagate eastward (e.g., due to Doppler shifts). Their contribution overall is as large as for ERs and even dominates in the Western Hemisphere, where upper-level westerlies occur during the boreal winter half year and allow the equatorward propagation of extratropical Rossby waves (e.g., Knippertz, 2007). Therefore, we suspect these to be mostly a reflection of disturbances with wave activity concentrated in the subtropics of one hemisphere projecting onto the basis functions for EWs (Yang and Hoskins, 2016), illustrating the difficulty in interpretation when wave disturbances exist on a state with strong meridional shear in the zonal flow. The coexistence of eastward- and westward-propagating ERs may also explain the apparently noisy “standing patterns” in 3DS-HF in Figure 13l, whereas 2DS-PCF shows only the westward-filtered ERs (Figure 13k).

Corresponding plots for  $u$  at 850 hPa (Figure 16c,d) show much reduced unfiltered variance compared with 200 hPa (black lines). Nevertheless, the contributions of KWs and ERs for both FWF-PCF and 2DS-PCF have some similarities to 200 hPa. Exceptions are the areas of high terrain in East Africa and South America, where 850 hPa winds are ill defined in ERA5. In stark contrast to 200 hPa, however, ER-E have hardly any influence at this level due to the dominance of easterlies, except maybe over the

Indian Ocean, where low-level westerlies can occur (see Figure 5 for an example).

For meridional wind  $v$ , unfiltered variance at 200 hPa is relatively weak in the Eastern Hemisphere but almost as large as that in  $u$  in the Western Hemisphere (black lines in Figure 16e,f). According to FWF-PCF (Figure 16e), only about 10% of the variability is explained by MRGs with little longitudinal structure. In contrast, 2DS-PCF (Figure 16f) estimates much larger contributions on the order of 40%, indicating that much of that variability lies outside of the narrow window in  $k$ – $\omega$  space used in FWF-PCF. In addition, 2DS-PCF finds substantial contributions from eastward-moving MRGs (labelled MRG-E), such that the explained variance exceeds 60% throughout the tropical belt. This is consistent with the apparent two-way propagation of MRGs in Figure 11f based on 3DS-HF, which includes both types. Signals at 850 hPa (Figure 16g,h) are again characterized by much smaller overall variance, but relative contributions from MRG and MRG-E waves are not dissimilar from 200 hPa. As for  $u$ , distortions by topography are evident and the relative role of eastward-moving signals is reduced relative to 200 hPa, but not as much as for ERs.

Figure 17 shows results for antisymmetric structures in  $v$  using again the methods FWF-PCF and 2DS-PCF. Comparing the unfiltered variances with their symmetric counterparts from Figure 16e–h shows an expected



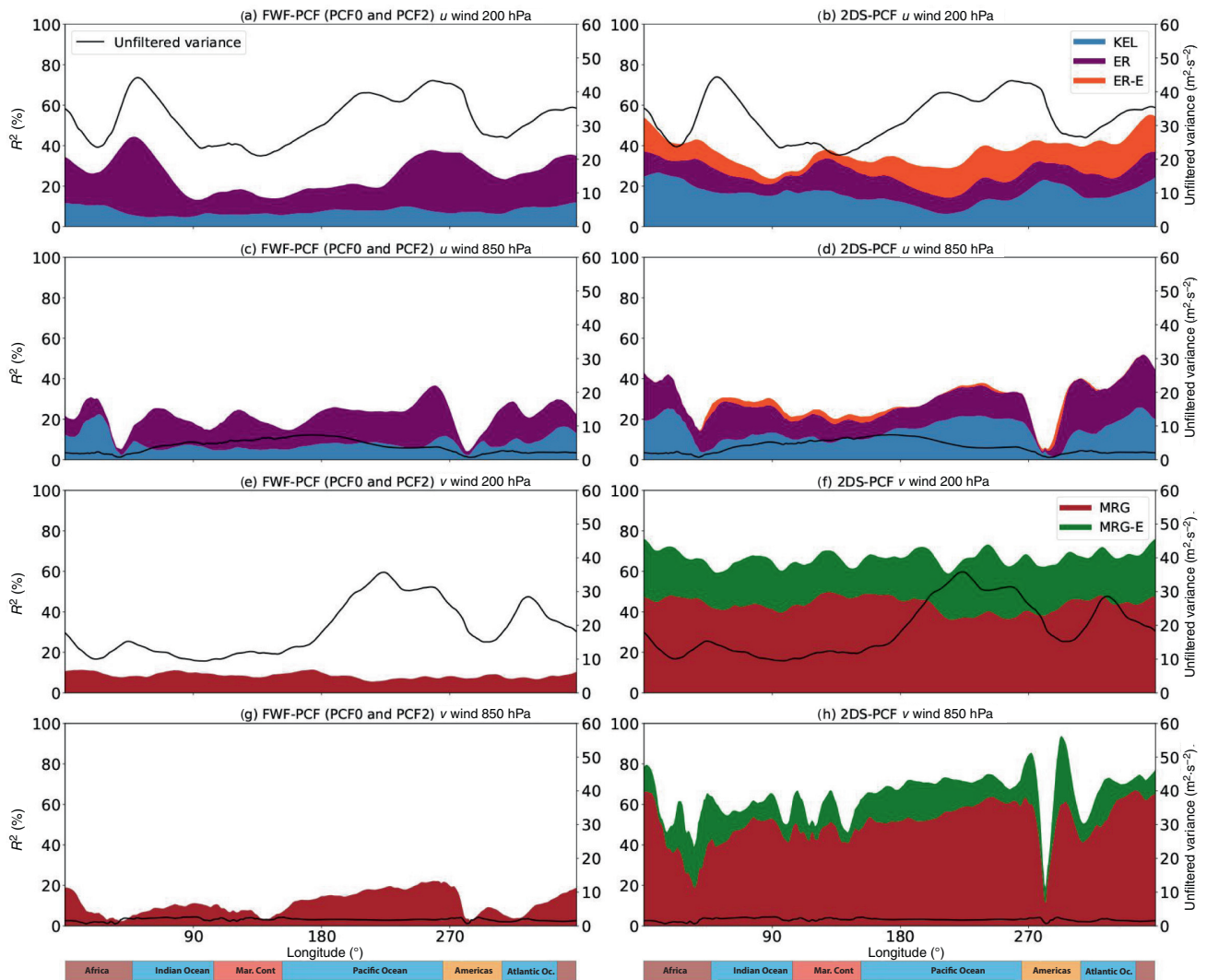


**FIGURE 16** Total (daily) symmetric variance (black lines, right axis) and fraction explained by individual wave types (in per cent, shadings, left axis) for 2001–2018. The results are based on ERA5 reanalysis using the method (a, c, e, g) frequency–wave-number filtering using parabolic cylinder functions (FWF-PCF: PCF0 and PCF2) and (b, d, f, h) two-dimensional spatial projection using parabolic cylinder functions (2DS-PCF). Zonal wind at (a, b) 200 hPa and (c, d) 850 hPa as well as meridional wind at (e, f) 200 hPa and (g, h) 850 hPa. All fields are averaged from 15° S to 15° N before the computation of variance and correlations. Note that the axis for explained variance stretches to 100% in contrast to Figures 15 and 17. MRG, mixed Rossby–gravity wave; MRG-E, eastward-moving MRG [Colour figure can be viewed at [wileyonlinelibrary.com](http://wileyonlinelibrary.com)]

reduction (black lines). At 200 hPa, variance about halves in the Eastern Hemisphere and decreases even more in the Western Hemisphere. Using FWF-PCF, about 20% of the variance at 200 hPa is explained by ERs and slightly smaller fractions at 850 hPa (Figure 17a,c). As for the symmetric  $v$  shown in Figure 16f,h, the 2DS-PCF method finds much larger contributions from ERs at both levels and additional contributions from ER-E waves, particularly at 200 hPa (Figure 17b,d). Together, about 60% of the unfiltered variance can be explained, with slightly lower values at 850 hPa and more longitudinal structure. The importance of both ER and ER-E for  $v$  is also evident in the Hovmoeller plot based on 3DS-HF (Figure 13i).

## 5 | CONCLUSIONS

EWs dominate synoptic- to planetary-scale variability in the low latitudes from the daily to the subseasonal time-scale and have been a research focus in tropical meteorology for decades. Most work on the subject relies on (or at least refers to) theoretical wave solutions derived from dynamical equations linearized around an atmospheric state of rest with a fixed vertical stability profile, either on the equatorial  $\beta$ -plane or on a sphere. In addition to the theoretical wave solutions (KW, MRG, ER, EIG, WIG), TDs, which includes tropical cyclones, Pacific and African Easterly Waves, and the MJO are included in the

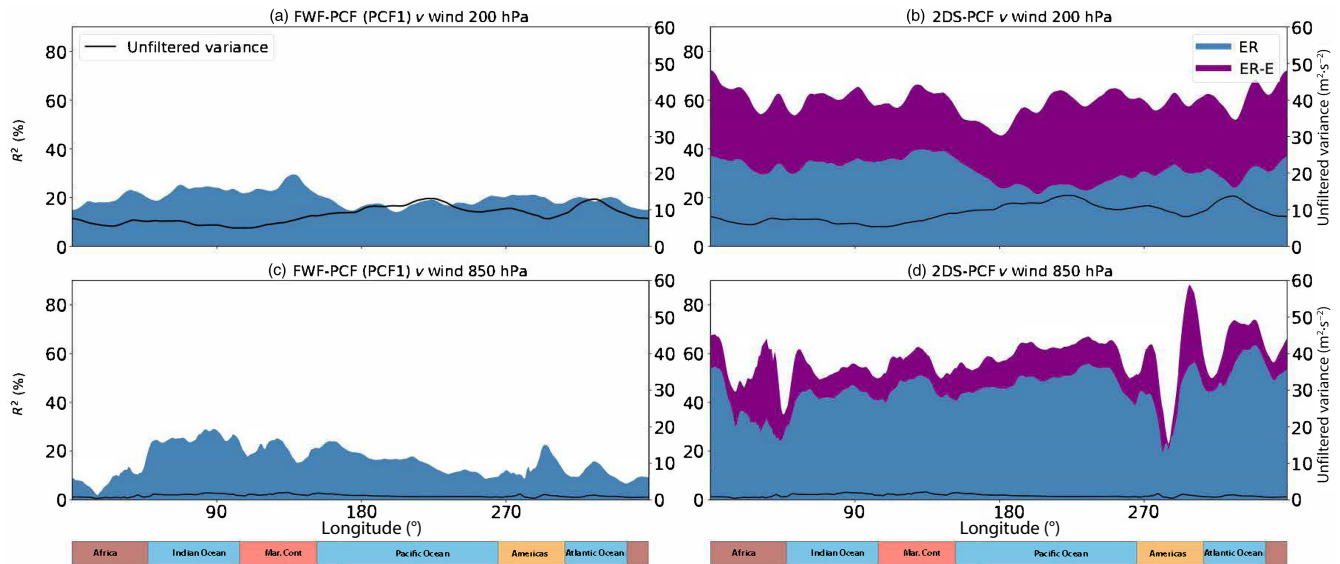


**FIGURE 17** Total (daily) antisymmetric variance (black lines, right axis) and fraction explained by individual wave types (in per cent, shadings, left axis) for 2001–2018. The results are based on ERA5 reanalysis using the method (a, c) frequency–wave-number filtering using parabolic cylinder functions (FWF-PCF; PCF1 only) and (b, d) two-dimensional spatial projection using parabolic cylinder functions (2DS-PCF). Meridional wind at (a, b) 200 hPa and (c, d) 850 hPa. All fields are averaged in an antisymmetric way from 15° S to 15° N before the computation of variance and correlations [Colour figure can be viewed at [wileyonlinelibrary.com](http://wileyonlinelibrary.com)]

concept of EWs. Often, EWs couple with moist convection and are then referred to as CCEWs. In this paper, we have for the first time systematically compared six different objective methods designed to isolate EWs from satellite or model data. For this comparison, we chose both a case study (February 20–May 20, 2009) and a climatological (2001–2018) perspective, concentrating on the global tropical belt (15° S–15° N). As input, standard datasets for OLR (from NOAA), narrowband IR (from CERES), and rainfall (from IMERG) as well as geopotential  $\phi$  and zonal and meridional wind ( $u$  and  $v$ ) at different vertical levels (all from ERA5) were used. Details of the six methods and how we have employed them in this study are provided in Sections 3 and 4, respectively, and shall not be repeated here (see Figure 3 for an overview). An underlying question of the study is on how the different methods deal with violations of the underlying assumptions, such as variations in stability (e.g., through coupling with convection), Doppler shifts, vertical and meridional wind shear, non-sinusoidal structures, off-equatorial signals, and interactions with the extratropics. The main conclusions from this comprehensive analysis are as follows.

**1. Overall sensitivity:** The identified EW signal (i.e., its amplitude, phase speed, dominant  $k$ , and longitudinal variations) generally depends on the input data, the identification method, the wave type considered, the longitude, the vertical level (only analysed for wind and divergence), and the season and year.

**2. Input data:** CCEWs can be identified well from OLR, CERES, and IMERG. Although unfiltered fields show substantial differences in structure and amplitude, frequency–wave-number filtering (FFW; as demonstrated here for the KW) creates largely consistent results with pattern correlations above 0.7 in Hovmöller diagrams. To make input fields more comparable, a normalization with the respective daily standard deviation can be applied ( $Z$  scores), but this has hardly any effect on the wave features identified. The dry components of EWs can be identified in  $\phi$ ,  $u$ ,  $v$ , and divergence, but individual EWs are typically harder to see without filtering. There is some indication of a first baroclinic vertical structure with opposing signals at 200 hPa and 850 hPa, but signals in the latter level are usually much weaker. Divergence is a relatively noisy field that shows moderate agreement with IMERG rainfall and OLR. The climatological analysis reveals that moist variables have maximum variance over the warm waters of the Indian and Pacific oceans, whereas dynamical fields have high variance over the Western Hemisphere, possibly partly related to extratropical synoptic activity.

**3. General characterization of methods:** The six methods analysed can broadly be grouped into those dominated by FWF and those dominated by two- and three-dimensional spatial projection (2DS and 3DS), which show fundamentally different results. There is generally good agreement between the three FWF

methods (FWF-FFT, FWF-Wavelet, FWF-PCF), which are usually applied to OLR, and between 2DS-PCF and 3DS-HF, which use wind and geopotential as input and can accommodate more abrupt changes and a much wider range of phase speeds. 2DS-EOF is a hybrid method, in the sense that it relies on relatively narrow filter windows and spatial projection on empirical OLR patterns at the same time, leading to a relatively small fraction of the climatological variance explained by EWs. For the KW case study, the three spatial projection methods show smaller  $k$  as well as faster (2DS-PCF and 3DS-HF) and slower (2DS-EOF) propagation than the FWF methods. For the MRG case study, hardly any significant wave signals are found using the FWF methods, in stark contrast to 2DS-PCF and 3DS-HF with intermediate amplitudes in 2DS-EOF, which suggests reduced convective coupling as well as issues with strong longitudinal confinement and slow propagation due to Doppler shifts. A smaller disagreement among the methods for the KW is expected, given its nearly non-dispersive nature and a geostrophic balance between the zonal wind and the meridional pressure gradient. For the ER case study, some level of correspondence is found for all six methods and different input fields, in spite of the different role of the background wind for the FWF methods. Comparing explained wind variances between FWF-PCF and 2DS-PCF, the latter finds generally higher contributions from KWs, MRGs, and ERs, with details depending on the wind component and symmetry. Finally, it should be noted that the FWF methods and 2DS-EOF can easily be expanded to identify phenomena for which no theoretical wave solution patterns exist (such as TDs and the MJO), though this is less straightforward for 2DS-PCF and 3DS-HF (e.g., Kitsios *et al.*, 2019).

**4. Differences between FWF methods:** FWF-FFT is the oldest and most widely used method. Applied to the global wide tropical belt, results from FWF-Wavelet are almost identical to those of FWF-FFT, but the wavelets can more flexibly be applied to shorter time-scales and non-global data. Interestingly, the variance explained by EWs is slightly higher with FWF-Wavelet despite generally lower-amplitude signals, presumably due to a better representation of local features. Contrasts between FWF-FFT and FWF-PCF are larger, with the latter generally showing lower-amplitude wave signals. This indicates that the latitudinal average used for FWF-FFT contains signals of higher order than represented in the one or two PCFs used for FWF-PCF (i.e., PCF1 for Equator-antisymmetric signals, and PCF0 and PCF2 for Equator-symmetric signals). The problem is particularly acute for OLR over the eastern Pacific due to the predominantly off-equatorial convection, where

this method finds less explained variance than the other two. There are also clear structural differences when applying FWF-PCF to OLR and wind.

- 5. Differences between spatial-projection methods:** Despite a number of fundamental differences such as equatorial  $\beta$ -plane versus spherical system, univariate versus multivariate projection, and single-level versus multilevel projection using different equivalent depths  $D$ , there is remarkable agreement between the results using 2DS-PCF and 3DS-HF for the 3-month period analysed. This pertains primarily to the horizontal and vertical structures and to a smaller degree to the Hovmoeller plots. Owing to the chosen meridional scale of  $y_0 = 6^\circ$ , wave signals are generally more confined to the tropical belt in 2DS-PCF than 3DS-HF. Though KWs are relatively consistent, larger discrepancies are evident with respect to ERs and MRGs. This may be due to the fact that 2DS-PCF applies frequency filtering to separate the westward- and eastward-propagating signals, whereas the 3DS-HF Hovmoeller plots reflect both westward- and eastward-propagating disturbances projecting onto the MRG and ER meridional structures. It is therefore useful to partition them to see clear propagation signatures, particular as the eastward signals may reflect the penetration of extratropical Rossby waves into the Tropics (mostly over the so-called westerly duct regions over the eastern Pacific and Atlantic). The challenge here, like with the FWF methods, is to separate wave signals from the quasi-stationary background state. The ER case study also demonstrates that the single-variate projection of 2DS-PCF can lead to considerably different results for  $u$  and  $v$ , which suggests nonlinear dynamics. A systematic comparison between 2DS-EOF on the one hand and 2DS-PCF and 3DS-HF on the other hand is difficult due to the different input data (OLR vs. dynamical fields).
- 6. Near-real time applications:** A common application for EW identification methods is near-real-time monitoring or prediction based on satellite observations or model analysis and forecast fields. Such applications are relatively straightforward for the spatial-projection methods, as these use broad filters in time (or no filters at all). To test the impact of the much narrower filter windows used in the FWF methods, an experiment with padded zeros after a defined end date was conducted. It demonstrates that the distortion to the wave identification depends on the wave type with correlations to the original results falling off to 0.8 one day before the cut-off for KW and more than a week for ER.
- 7. Significance of identified wave signals:** A challenging question is whether the EW signals identified with a given method can be considered to stand out



significantly from the background noise. To illustrate this problem, we conducted experiments in which the spectrum of the OLR data used was retained but with wave phases randomized. Applying FWF-FFT to the randomized data yields Hovmoeller plots that share many characteristics with those of the real data, although amplitudes are overall somewhat reduced and longitudinal differences disappear. This demonstrates that the relatively narrow filter windows can isolate seemingly coherent structures from random data and that only features that clearly stand out in amplitude and longevity should be considered as significant and physically meaningful. In fact, given the results of this paper, we generally recommend comparing results from FWF methods with those from spatial-projection methods to check for robustness of the signal identified. If several methods (and different input fields) agree, one can be relatively certain that a “real” physical EW feature has been isolated. If this is not the case, one needs to investigate carefully which assumptions made for the individual methods are most probably not fulfilled to explain the differences found.

The discrepancies between the EW identification results from different methods—systematically shown in this paper for the first time—have brought to light a number of challenges that require further study. We suspect these discrepancies to largely come about through assumptions/simplifications in the underpinning wave theory. First, whereas the classical theory assumes a resting basic state, the real atmosphere shows (seasonally varying) considerable large-scale shear in the zonal flow. Second, the theory is essentially dry and cannot directly account for effects of moisture, convection, and latent heat release. Third, as convection often occurs away from the Equator, we expect the dynamical structures of EWs to be distorted such that projection onto the structures for a resting, dry atmosphere could miss a lot of the EW activity simply due to a mismatch in meridional structure. Fourth, the current theory does not take into account the influence of surface fluxes and friction, or even interactions with the ocean for the slowest waves as debated for the MJO (Zhang *et al.*, 2020). Fifth, being an essentially linear theory, interactions between different waves are not considered. It would be particularly interesting to examine whether the eastward and westward EW modes can propagate through each other without modification (e.g., Dias and Kiladis, 2016). There is some evidence that precipitation can be enhanced through superposition of different wave types (e.g., Schlueter *et al.*, 2019a). It seems likely that the associated convective heating can alter both, while corresponding wind structures may propagate more smoothly. Finally, this paper has presented some evidence for possible conversion of extratropical wave energy into

EWs, and vice versa, but the significance and the dynamics of this process remain somewhat unclear. We are confident that the complementary nature of the different EW identification tools analysed here can help to shed more light into these fascinating issues.

## AUTHOR CONTRIBUTIONS

**Peter Knippertz:** conceptualization; funding acquisition; methodology; supervision; writing – original draft. **Maria Gehne:** data curation; formal analysis; investigation; software; visualization. **George N. Kiladis:** conceptualization; data curation; formal analysis; investigation; writing – review and editing. **Kazuyoshi Kikuchi:** formal analysis; visualization. **Athul Rasheeda Satheesh:** **Paul E. Roundy:** conceptualization; data curation; formal analysis; investigation; visualization. **Gui-Ying Yang:** conceptualization; data curation; formal analysis; investigation; visualization; writing – review and editing. **Nedjeljka Žagar:** **Juliana Dias:** conceptualization; formal analysis; investigation; writing – review and editing. **Andreas H. Fink:** conceptualization; funding acquisition; investigation; supervision; writing – review and editing. **John Methven:** conceptualization; investigation; writing – review and editing. **Andreas Schlueter:** investigation; writing – review and editing. **Frank Sielmann:** data curation; formal analysis; visualization. **Matthew C. Wheeler:** investigation; writing – review and editing.

## ACKNOWLEDGEMENTS

The research leading to these results has been accomplished within project C2 “Statistical-dynamical forecasts of tropical rainfall” of the Transregional Collaborative Research Center SFB/ TRR 165 “Waves to Weather” funded by the German Science Foundation. AS was funded as a Schmidt Science Fellow during the period of writing this paper. We thank Martin Stengel for advice on satellite imagery. PK would like to thank Michael Reeder and Christian Jakob for hosting a 6-months sabbatical at Monash University in Melbourne (Australia), during which this paper was initiated. We thank Steve Woolnough (University of Reading) for his useful comments in the early stages of this project. NZ and FS thank Kalil Karami for applying the MODES software to ERA5 data. We are grateful for the constructive criticism from two anonymous reviewers. Open Access funding enabled and organized by Projekt DEAL.






## ORCID

Peter Knippertz  <https://orcid.org/0000-0001-9856-619X>

Maria Gehne  <https://orcid.org/0000-0002-7267-8676>

Paul E. Roundy  <https://orcid.org/0000-0002-2201-0002>

Gui-Ying Yang  <https://orcid.org/0000-0001-7450-3477>

Nedjeljka Žagar  <https://orcid.org/0000-0002-7256-5073>  
 Andreas H. Fink  <https://orcid.org/0000-0002-5840-2120>  
 John Methven  <https://orcid.org/0000-0002-7636-6872>  
 Andreas Schlueter  <https://orcid.org/0000-0002-5398-8150>  
 Matthew C. Wheeler  <https://orcid.org/0000-0002-9769-1973>

## REFERENCES

- Andrews, D.G. and McIntyre, M.E. (1976) Planetary waves in horizontal and vertical shear: Asymptotic theory for equatorial waves in weak shear. *Journal of the Atmospheric Sciences*, 33, 2049–2053.
- Baldwin, M.P., Gray, L.J., Dunkerton, T.J., Hamilton, K., Haynes, P.H., Randel, W.J., Holton, J.R., Alexander, M.J., Hirota, I., Hironouchi, T., Jones, D.B.A., Kinnerson, J.S., Marquardt, C., Sato, K. and Takahashi, M. (2001) The quasi-biennial oscillation. *Reviews of Geophysics*, 39, 179–229.
- Bengtsson, L., Dias, J., Gehne, M., Bechtold, P., Whitaker, J., Bao, J.-W., Magnusson, L., Michelson, S., Pegion, P., Tulich, S. and Kiladis, G.N. (2019) Convectively coupled equatorial wave simulations using the ECMWF IFS and the NOAA GFS cumulus convection schemes in the NOAA GFS model. *Monthly Weather Review*, 147, 4005–4025.
- Blaauw, M. and Žagar, N. (2018) Multivariate analysis of Kelvin wave seasonal variability in ECMWF L91 analyses. *Atmospheric Chemistry and Physics*, 18, 8313–8330.
- Boyd, J.P. (1978) The effects of latitudinal shear on equatorial waves. Part II: Applications to the atmosphere. *Journal of the Atmospheric Sciences*, 35, 2259–2267.
- Boyd, J.P. (1985) Barotropic equatorial waves: The non-uniformity of the equatorial beta-plane. *Journal of the Atmospheric Sciences*, 42, 1865–1967.
- Boyd, J.P. (2018) *Dynamics of the equatorial ocean*. Berlin, Germany: Springer-Verlag.
- Boyd, J.P. and Zhou, C. (2008) Uniform asymptotics for the linear Kelvin wave in spherical geometry. *Journal of the Atmospheric Sciences*, 65, 655–660.
- Burpee, R.W. (1972) The origin and structure of easterly waves in the lower troposphere of North Africa. *Journal of the Atmospheric Sciences*, 29, 77–90.
- Castanheira, J.M. and Marques, C.A.F. (2015) Convectively coupled equatorial-wave diagnosis using three-dimensional normal modes. *Quarterly Journal of the Royal Meteorological Society*, 141, 2776–2792.
- Daley, R. (1993) Atmospheric data analysis on the equatorial beta plane. *Atmosphere–Ocean*, 31, 421–450.
- Del Genio, A.D. and Rossow, W.B. (1990) Planetary-scale waves and the cyclic nature of cloud top dynamics on Venus. *Journal of the Atmospheric Sciences*, 47, 293–318.
- Dias, J., Dias, P.L.S., Kiladis, G.N. and Gehne, M. (2013a) Modulation of shallow-water equatorial waves due to a varying equivalent height background. *Journal of the Atmospheric Sciences*, 70, 2726–2750.
- Dias, J., Gehne, M., Kiladis, G.N., Sakaeda, N., Bechtold, P. and Haiden, T. (2018) Equatorial waves and the skill of NCEP and ECMWF numerical weather prediction systems. *Monthly Weather Review*, 146, 1763–1784.
- Dias, J. and Kiladis, G.N. (2014) Influence of the basic state zonal flow on convectively coupled equatorial waves. *Geophysical Research Letters*, 41, 6904–6913.
- Dias, J. and Kiladis, G.N. (2016) The relationship between equatorial mixed Rossby–gravity and eastward inertia–gravity waves. Part II. *Journal of the Atmospheric Sciences*, 73, 2147–2163.
- Dias, J. and Kiladis, G.N. (2019) The influence of tropical forecast errors on higher latitude predictions. *Geophysical Research Letters*, 46, 4450–4459.
- Dias, J., Leroux, S., Tulich, S.N. and Kiladis, G.N. (2013b) How systematic is organized tropical convection within the MJO?. *Geophysical Research Letters*, 40, 1420–1425.
- Dias, J. and Pauluis, O. (2009) Convectively coupled waves propagating along an equatorial ITCZ. *Journal of the Atmospheric Sciences*, 66, 2237–2255.
- Dias, J., Tulich, S.N., Gehne, M. and Kiladis, G.N. (2021) Tropical origins of weeks 2–4 forecasts errors during Northern Hemisphere cool season. *Monthly Weather Review*, 73, 2147–2163.
- Doelling, D.R., Sun, M., Nguyen, L.T., Nordeen, M.L., Haney, C.O., Keyes, D.F. and Mlynchzak, P.E. (2016) Advances in geostationary-derived longwave fluxes for the CERES Synoptic (SYN1deg) product. *Journal of Atmospheric and Oceanic Technology*, 33, 503–521.
- Farrar, J.T. and Durland, T.S. (2012) Wavenumber–frequency spectra of inertia–gravity and mixed Rossby–gravity waves in the equatorial Pacific Ocean. *Journal of Physical Oceanography*, 42, 1859–1881.
- Ferguson, J., Khouider, B. and Namazi, M. (2009) Two-way interactions between equatorially-trapped waves and the barotropic flow. *Chinese Annals of Mathematics, Series B*, 30, 539–568.
- Ferrett, S., Yang, G.-Y., Woolnough, S., Methven, J., Hodges, K. and Holloway, C. (2020) Linking extreme precipitation in southeast Asia to equatorial waves. *Quarterly Journal of the Royal Meteorological Society*, 146, 665–684.
- Frank, W.M. and Roundy, P.E. (2006) The role of tropical waves in tropical cyclogenesis. *Monthly Weather Review*, 134, 2397–2417.
- Gehne, M. and Kleeman, R. (2012) Spectral analysis of tropical atmospheric dynamical variables using a linear shallow-water modal decomposition. *Journal of the Atmospheric Sciences*, 69, 2300–2316.
- Gill, A.E. (1980) Some simple solutions for heat-induced tropical circulation. *Quarterly Journal of the Royal Meteorological Society*, 106, 447–462.
- Gill, A.E. (1982) *Atmosphere–ocean dynamics*. New York, NY: Academic Press.
- Gribble-Verhagen, L. and Roundy, P.E. (2010) Analysis of apparent coupling between an oceanic Kelvin wave and atmospheric convection during the winter of 1986/87. *Journal of Climate*, 23, 6352–6364.
- Gruber, A. (1974) The wavenumber–frequency spectra of satellite-measured brightness in the Tropics. *Journal of the Atmospheric Sciences*, 31, 1675–1680.
- Haiden, T., Rodwell, M.J., Richardson, D.S., Okagaki, A., Robinson, T. and Hewson, T. (2012) Intercomparison of global model precipitation forecast skill in 2010/11 using the SEEPS score. *Monthly Weather Review*, 140, 2720–2733.
- Hall, N., Kiladis, G. and Thorncroft, C. (2006) Three-dimensional structure and dynamics of African easterly waves. Part II: Dynamical modes and growth mechanisms. *Journal of the Atmospheric Sciences*, 63, 2231–2245.

- Han, Y. and Khouider, B. (2010) Convectively coupled waves in a sheared environment. *Journal of the Atmospheric Sciences*, 67, 2913–2942.
- Hayashi, J. (1971) A generalized method of resolving disturbances into progressive and retrogressive waves by space Fourier and time cross-spectral analyses. *Journal of the Meteorological Society of Japan*, 49, 125–128.
- Hayashi, J. (1981) Space–time spectral analysis and its applications to atmospheric waves. *Journal of the Meteorological Society of Japan*, 60, 156–171.
- Hendon, H.H. and Wheeler, M.C. (2008) Some space–time spectral analyses of tropical convection and planetary-scale waves. *Journal of the Atmospheric Sciences*, 65, 2936–2948.
- Hersbach, H., Bell, B., Berrisford, P., Hirahara, S., Horányi, A., Muñoz-Sabater, J., Nicolas, J., Peubey, C., Radu, R., Schepers, D., Simmons, A., Soci, C., Abdalla, S., Abellan, X., Balsamo, G., Bechtold, P., Biavati, G., Bidlot, J., Bonavita, M., De Chiara, G., Dahlgren, P., Dee, D., Diamantakis, M., Dragani, R., Flemming, J., Forbes, R., Fuentes, M., Geer, A., Haimberger, L., Healy, S., Hogan, R.J., Hólm, E., Janisková, M., Keeley, S., Laloyaux, P., Lopez, P., Lupu, C., Radnoti, G., de Rosnay, P., Rozum, I., Vamborg, F., Villaume, S. and Thépaut, J.-N. (2020) The ERA5 global reanalysis. *Quarterly Journal of the Royal Meteorological Society*, 146, 1999–2049.
- Hoskins, B. and Yang, G.-Y. (2016) The longitudinal variation of equatorial waves due to propagation on a varying zonal flow. *Journal of the Atmospheric Sciences*, 73, 605–620.
- Hoskins, B.J. and Yang, G.-Y. (2000) The equatorial response to higher-latitude forcing. *Journal of the Atmospheric Sciences*, 57, 1197–1213.
- Hough, S.S. (1897) On the application of harmonic analysis to the dynamical theory of the tides. Part I. On Laplace's oscillations of the first species, and on the dynamics of ocean currents. *Philosophical Transactions of the Royal Society A: Mathematical, Physical and Engineering Sciences*, 189, 201–257.
- Huffman, G.J., Bolvin, D.T., Braithwaite, D., Hsu, K., Joyce, R., Kidd, C., Nelkin, E.J. and Xie, P. (2015) NASA Global Precipitation Measurement (GPM) Integrated Multi-satellite Retrievals for GPM (IMERG). Algorithm Theoretical Basis Document (ATBD) Version 4.5. Greenbelt, MD: National Aeronautics and Space Administration. [http://pmm.nasa.gov/sites/default/files/document\\_files/IMERG\\_ATBD\\_V4.5.pdf](http://pmm.nasa.gov/sites/default/files/document_files/IMERG_ATBD_V4.5.pdf)
- Huffman, G.J., Stocker, E., Bolvin, D.T., Nelkin, E. and Tan, J. (2019). GPM IMERG final precipitation L3 half hourly 0.1 degree  $\times$  0.1 degree V06 (GPM\_3IMERGHH). <https://doi.org/10.5067/GPM/IMERG/3B-HH/06>
- Janiga, M.A., J. Schreck and C., R.i.d.o.u.t. (2018) Subseasonal forecasts of convectively coupled equatorial waves and the MJO: Activity and predictive skill. *Monthly Weather Review*, 146, 2337–2360.
- Judt, F. (2018) Insights into atmospheric predictability through global convection-permitting model simulations. *Journal of the Atmospheric Sciences*, 75, 1477–1497.
- Judt, F. (2020) Atmospheric predictability of the Tropics, middle latitudes, and polar regions explored through global storm-resolving simulations. *Journal of the Atmospheric Sciences*, 77, 257–276.
- Judt, F. and Rios-Berrios, R. (2021) Resolved convection improves the representation of equatorial waves and tropical rainfall variability in a global nonhydrostatic model. *Geophysical Research Letters*, 48, e2021GL093265.
- Jung, T., Miller, M.J. and Palmer, T.N. (2010) Diagnosing the origin of extended-range forecast errors. *Monthly Weather Review*, 138, 2434–2446.
- Kasahara, A. (1976) Normal modes of ultralong waves in the atmosphere. *Monthly Weather Review*, 104, 669–690.
- Kasahara, A. (1978) Further studies on a spectral model of the global barotropic primitive equations with Hough harmonic expansions. *Journal of the Atmospheric Sciences*, 35, 2043–2051.
- Kasahara, A. (1980) Effect of zonal flows on the free oscillations of a barotropic atmosphere. *Journal of the Atmospheric Sciences*, 37, 917–929. Corrigendum, *Journal of the Atmospheric Sciences*, 38 (1981), 2284–2285.
- Kasahara, A. (1984) The linear response of a stratified global atmosphere to a tropical thermal forcing. *Journal of the Atmospheric Sciences*, 41, 2217–2237.
- Kasahara, A. and Puri, K. (1981) Spectral representation of three-dimensional global data by expansion in normal mode functions. *Monthly Weather Review*, 109, 37–51.
- Kikuchi, K. (2014) An introduction to combined Fourier–wavelet transform and its application to convectively coupled equatorial waves. *Climate Dynamics*, 43, 1339–1356.
- Kikuchi, K., Kiladis, G.N., Dias, J. and Nasuno, T. (2018) Convectively coupled equatorial waves within the MJO during CINDY/DYNAMO: Slow Kelvin waves as building blocks. *Climate Dynamics*, 50, 4211–4230.
- Kikuchi, K. and Wang, B. (2010) Spatiotemporal wavelet transform and the multiscale behavior of the Madden–Julian Oscillation. *Journal of Climate*, 23, 3814–3834.
- Kiladis, G.N., Dias, J. and Gehne, M. (2016) The relationship between equatorial mixed Rossby–gravity and eastward inertia-gravity waves. Part I. *Journal of the Atmospheric Sciences*, 73, 2123–2145.
- Kiladis, G.N., Thorncroft, C.D. and Hall, N.M.J. (2006) Three-dimensional structure and dynamics of African easterly waves. Part I: Observations. *Journal of the Atmospheric Sciences*, 63, 2212–2230.
- Kiladis, G.N. and Weickmann, K.M. (1992) Extratropical forcing of tropical Pacific convection during northern winter. *Monthly Weather Review*, 120, 1924–1938.
- Kiladis, G.N. and Wheeler, M.C. (1995) Horizontal and vertical structure of observed tropospheric equatorial Rossby waves. *Journal of Geophysical Research*, 100, 22981–22997.
- Kiladis, G.N., Wheeler, M.C., Haertel, P.T., Straub, K.H. and Roundy, P.E. (2009) Convectively coupled equatorial waves. *Reviews of Geophysics*, 47, RG2003. <https://doi.org/10.1029/2008RG000266>
- Kitsios, V., O'Kane, T.J. and Žagar, N. (2019) A reduced-order representation of the Madden–Julian Oscillation based on reanalyzed normal mode coherences. *Journal of the Atmospheric Sciences*, 76, 2463–2480.
- Knippertz, P. (2007) Tropical–extratropical interactions related to upper-level troughs at low latitudes. *Dynamics of Atmospheres and Oceans*, 43, 36–62.
- Kosovelj, K., Kucharski, F., Molteni, F. and Žagar, N. (2019) Modal decomposition of the global response to tropical heating perturbations resembling MJO. *Journal of the Atmospheric Sciences*, 76, 1457–1469.
- Li, Y. and Stechmann, S.N. (2020) Predictability of tropical rainfall and waves: Estimates from observational data. *Quarterly Journal of the Royal Meteorological Society*, 146, 1668–1684.



- Liebmann, B. and Smith, C.A. (1996) Description of a complete (interpolated) outgoing longwave radiation dataset. *Bulletin of the American Meteorological Society*, 77, 1275–1277.
- Lindzen, R.S. and Holton, J.R. (1968) A theory of the Quasi-Biennial Oscillation. *Journal of the Atmospheric Sciences*, 25, 1095–1107.
- Longuet-Higgins, M.S. (1968) The eigenfunctions of Laplace's tidal equations over a sphere. *Philosophical Transactions of the Royal Society A: Mathematical, Physical and Engineering Sciences*, 262, 511–607.
- Madden, R.A. and Julian, P.R. (1972) Description of global-scale circulation cells in the Tropics with a 40–50 day period. *Journal of the Atmospheric Sciences*, 29, 1109–1123.
- Maganã, V. and Yanai, M. (1995) Mixed Rossby–gravity waves triggered by lateral forcing. *Journal of the Atmospheric Sciences*, 52, 1473–1486.
- Majda, A.J. and Biello, J.A. (2003) The nonlinear interaction of barotropic and equatorial baroclinic Rossby waves. *Journal of the Atmospheric Sciences*, 60, 1809–1821.
- Marques, C.A.F. and Castanheira, J.M. (2018) Diagnosis of free and convectively coupled equatorial waves. *Mathematical Geosciences*, 50, 585–606.
- Matsuno, T. (1966) Quasi-geostrophic motions in the equatorial area. *Journal of the Meteorological Society of Japan*, 44(1), 25–43. [https://doi.org/10.2151/jmsj1965.44.1\\_25](https://doi.org/10.2151/jmsj1965.44.1_25)
- Ogrosky, H.R. and Stechmann, S.N. (2015) Assessing the equatorial long-wave approximation: Asymptotics and observational data analysis. *Journal of the Atmospheric Sciences*, 72, 4821–4843.
- Ogrosky, H.R. and Stechmann, S.N. (2016) Identifying convectively coupled equatorial waves using theoretical wave eigenvectors. *Monthly Weather Review*, 144, 2235–2264.
- Pahlavan, H.A., Wallace, J.M., Fu, Q. and Kiladis, G.N. (2021) Revisiting the Quasi-Biennial Oscillation as seen in ERA5. Part II: Evaluation of waves and wave forcing. *Journal of the Atmospheric Sciences*, 78, 693–707.
- Paldor, N., Fouxon, I., Shamir, O. and Garfinkel, C. (2018) The mixed Rossby–gravity wave on the spherical Earth. *Quarterly Journal of the Royal Meteorological Society*, 144(715), 1820–1830. <https://doi.org/10.1002/qj.3354>
- Parrish, D. (1988). The introduction of Hough functions into optimum interpolation, *Proceedings of Eighth Conference on NWP* (pp. 191–196). Boston, MA: American Meteorological Society.
- Peatman, S., Methven, J. and Woolnough, S. (2018) Isolating the effects of moisture entrainment on convectively coupled equatorial waves in an aquaplanet GCM. *Journal of the Atmospheric Sciences*, 75, 3139–3157.
- Plumb, R.A. and McEwan, A.D. (1978) The instability of a forced standing wave in a viscous stratified fluid: A laboratory analogue of the Quasi-Biennial Oscillation. *Journal of the Atmospheric Sciences*, 35, 1827–1839.
- Podglajen, A., Hertzog, A., Plougonven, R. and Žagar, N. (2014) Assessment of the accuracy of (re)analyses in the equatorial lower stratosphere. *Journal of Geophysical Research*, 119, 11166–11188.
- Riley, E.M., Mapes, B.E. and Tulich, S.N. (2011) Clouds associated with the Madden–Julian Oscillation: A new perspective from CloudSat. *Journal of the Atmospheric Sciences*, 68, 3032–3051.
- Roundy, P.E. (2012a) Observed structure of convectively coupled waves as a function of equivalent depth: Kelvin waves and the Madden–Julian Oscillation. *Journal of the Atmospheric Sciences*, 69, 2097–2106.
- Roundy, P.E. (2012b) The spectrum of convectively coupled Kelvin waves and the Madden–Julian oscillation in regions of low-level easterly and westerly background flow. *Journal of the Atmospheric Sciences*, 69, 2107–2111.
- Roundy, P.E. (2012c) Tracking and prediction of large-scale organized tropical convection by spectrally focused two-step space–time EOF analysis. *Quarterly Journal of the Royal Meteorological Society*, 138, 919–931.
- Roundy, P.E. (2018) A wave-number frequency wavelet analysis of convectively coupled equatorial waves and the MJO over the Indian Ocean. *Quarterly Journal of the Royal Meteorological Society*, 144, 333–343.
- Roundy, P.E. (2020) Interpretation of the spectrum of eastward-moving tropical convective anomalies. *Quarterly Journal of the Royal Meteorological Society*, 146, 795–806.
- Roundy, P.E. and Kiladis, G.N. (2006) Observed relationships between oceanic Kelvin waves and atmospheric forcing. *Journal of Climate*, 19, 5253–5272.
- Roundy, P.E., Schreck, C.J. and Janiga, M.A. (2009) Contributions of convectively coupled equatorial Rossby waves and Kelvin waves to the real-time multivariate MJO indices. *Monthly Weather Review*, 137, 469–478.
- Schlueter, A., Fink, A.H. and Knippertz, P. (2019b) A systematic comparison of tropical waves over northern Africa. Part II: Dynamics and thermodynamics. *Journal of Climate*, 32(9), 2605–2625.
- Schlueter, A., Fink, A.H., Knippertz, P. and Vogel, P. (2019a) A systematic comparison of tropical waves over northern Africa. Part I: Influence on rainfall. *Journal of Climate*, 32(5), 1501–1523. <https://doi.org/10.1175/JCLI-D-18-0173.1>
- Serra, Y.L., Kiladis, G.N. and Cronin, M.F. (2008) Horizontal and vertical structure of easterly waves in the Pacific ITCZ. *Journal of the Atmospheric Sciences*, 65, 1266–1284.
- Shinoda, T., Kiladis, G.N. and Roundy, P.E. (2009) Statistical representation of equatorial waves and tropical instability waves in the Pacific Ocean. *Atmospheric Research*, 94, 37–44.
- Stechmann, S.N. and Majda, A.J. (2009) Gravity waves in shear and implications for organized convection. *Journal of the Atmospheric Sciences*, 66, 2579–2599.
- Stephan, C.C., Žagar, N. and Shepherd, T. (2021) Waves and coherent flows in the tropical atmosphere: New opportunities, old challenges. *Quarterly Journal of the Royal Meteorological Society*, 147, 2597–2624.
- Straub, K.H. and Kiladis, G.N. (2002) Observations of a convectively coupled Kelvin wave in the eastern Pacific ITCZ. *Journal of the Atmospheric Sciences*, 59, 30–53.
- Straub, K.H. and Kiladis, G.N. (2003) Extratropical forcing of convectively coupled Kelvin waves during austral winter. *Journal of the Atmospheric Sciences*, 60, 526–543.
- Sugimoto, N., Takagi, M. and Matsuda, Y. (2014) Waves in a Venus general circulation model. *Geophysical Research Letters*, 41, 7461–7467.
- Swarztrauber, P.N. and Kasahara, A. (1985) The vector harmonic analysis of Laplace tidal equations. *SIAM Journal on Scientific and Statistical Computing*, 6, 464–491.
- Takayabu, Y.N. (1994a) Large-scale cloud disturbances associated with equatorial waves. Part I: Spectral features of the cloud disturbances. *Journal of the Meteorological Society of Japan*, 72, 433–448.

- Takayabu, Y.N. (1994b) Large-scale cloud disturbances associated with equatorial waves. Part II: Westward-propagating inertio-gravity waves. *Journal of the Meteorological Society of Japan*, 72, 451–465.
- Tindall, J.C., Thuburn, J. and Highwood, E.J. (2006a) Equatorial waves in the lower stratosphere. I: A novel detection method. *Quarterly Journal of the Royal Meteorological Society*, 132, 177–194.
- Tindall, J.C., Thuburn, J. and Highwood, E.J. (2006b) Equatorial waves in the lower stratosphere. II: Annual and interannual variability. *Quarterly Journal of the Royal Meteorological Society*, 132, 195–212.
- Tulich, S.N. and Kiladis, G.N. (2012) Squall lines and convectively coupled gravity waves in the Tropics: Why do most cloud systems propagate westward?. *Journal of the Atmospheric Sciences*, 69, 2995–3012.
- Vitart, F., Robertson, A.W. and Anderson, D.L.T. (2012) Subseasonal to seasonal prediction project: Bridging the gap between weather and climate. *WMO Bulletin*, 61, 23–28.
- Vogel, P., Knippertz, P., Fink, A.H., Schlueter, A. and Gneiting, T. (2020) Skill of global raw and postprocessed ensemble predictions of rainfall in the Tropics. *Weather and Forecasting*, 35, 2367–2385.
- Wakata, Y. (2007) Frequency–wavenumber spectra of equatorial waves detected from satellite altimeter data. *Journal of Oceanography*, 63, 483–490.
- Waliser, D.E., Moncrieff, M.W., Burridge, D., Fink, A.H., Gochis, D., Goswami, B.N., Guan, B., Harr, P., Heming, J., Hsu, H.-H., Jakob, C., Janiga, M., Johnson, R., Jones, S., Knippertz, P., Marengo, J., Nguyen, H., Pope, M., Serra, Y., Thorncroft, C., Wheeler, M., Wood, R. and Yuter, S. (2012) The “Year” of Tropical Convection (May 2008–April 2010): Climate variability and weather highlights. *Bulletin of the American Meteorological Society*, 93, 1189–1218.
- Wang, B. and Xie, X. (1996) Low-frequency equatorial waves in vertically sheared zonal flow. Part I: Stable waves. *Journal of the Atmospheric Sciences*, 53, 3424–3437.
- Waugh, D. and Funatsu, B. (2003) Intrusions into the tropical upper troposphere: Three-dimensional structure and accompanying ozone and OLR distributions. *Journal of the Atmospheric Sciences*, 60, 637–653.
- Webster, P.J. (2020) *Dynamics of the tropical atmosphere and oceans*. Chichester, UK: John Wiley & Sons, Ltd.
- Wheeler, M.C. and Kiladis, G.N. (1999) Convectively coupled equatorial waves: Analysis of clouds and temperature in the wavenumber–frequency domain. *Journal of the Atmospheric Sciences*, 56, 374–399.
- Wheeler, M.C., Kiladis, G.N. and Webster, P.J. (2000) Large-scale dynamical fields associated with convectively coupled equatorial waves. *Journal of the Atmospheric Sciences*, 57, 613–640.
- Wheeler, M.C. and Nguyen, H. (2015). Tropical meteorology and climate: Equatorial waves. In G.R. North, J. Pyle, and F. Zhang (Eds.), *Encyclopedia of atmospheric sciences* (Vol. 6, 2nd ed., pp. 102–112). Amsterdam, Netherlands: Academic Press.
- Wheeler, M.C. and Weickmann, K.M. (2001) Real-time monitoring and prediction of modes of coherent synoptic to intraseasonal tropical variability. *Monthly Weather Review*, 129, 2677–2694.
- Wheeler, M.C., Zhu, H., Sobel, A.H., Hudson, D. and Vitart, F. (2017) Seamless precipitation prediction skill comparison between two global models. *Quarterly Journal of the Royal Meteorological Society*, 143, 374–383.
- Wong, M.L.M. (2009) Wavelet analysis of the convectively coupled equatorial waves in the wavenumber–frequency domain. *Journal of the Atmospheric Sciences*, 66, 209–212.
- Yamazaki, Y.H., Read, P.L. and Skeet, D.R. (2005) Hadley circulations and Kelvin wave-driven equatorial jets in the atmospheres of Jupiter and Saturn. *Planetary and Space Science*, 53, 508–525.
- Yang, G.-Y., Ferrett, S., Woolnough, S., Methven, J. and Holloyay, C. (2021) Real-time identification of equatorial waves and evaluation of waves in global forecasts. *Weather and Forecasting*, 36, 171–193.
- Yang, G.-Y. and Hoskins, B.J. (2013) ENSO impact on Kelvin waves and associated tropical convection. *Journal of the Atmospheric Sciences*, 70, 3513–3532.
- Yang, G.-Y. and Hoskins, B.J. (2016) ENSO-related variation of equatorial MRG and Rossby waves and forcing from higher latitudes. *Quarterly Journal of the Royal Meteorological Society*, 142, 2488–2504.
- Yang, G.-Y. and Hoskins, B.J. (2017) The equivalent barotropic structure of waves in the tropical atmosphere in the Western Hemisphere. *Journal of the Atmospheric Sciences*, 74, 1689–1704.
- Yang, G.-Y., Hoskins, B.J. and Slingo, J.M. (2003) Convectively coupled equatorial waves: A new methodology for identifying wave structures in observational data. *Journal of the Atmospheric Sciences*, 60, 1637–1654.
- Yang, G.-Y., Hoskins, B. and Slingo, J. (2007a) Convectively coupled equatorial waves. Part II: Propagation characteristics. *Journal of the Atmospheric Sciences*, 64, 3424–3437.
- Yang, G.-Y., Hoskins, B. and Slingo, J. (2007b) Convectively coupled equatorial waves. Part III: Synthesis structures and extratropical forcing. *Journal of the Atmospheric Sciences*, 64, 3438–3451.
- Yang, G.-Y., Hoskins, B.J. and Slingo, J.M. (2007c) Convectively coupled equatorial waves. Part I: Horizontal and vertical structures. *Journal of the Atmospheric Sciences*, 64, 3406–3423.
- Yang, G.-Y., Methven, J., Woolnough, S.J., Hodges, K.I. and Hoskins, B.J. (2018) Linking African easterly wave activity with equatorial waves and the influence of Rossby waves from the Southern Hemisphere. *Journal of the Atmospheric Sciences*, 75, 1783–1809.
- Yang, G.-Y., Slingo, J.M. and Hoskins, B.J. (2009) Convectively coupled equatorial waves in high resolution Hadley Centre climate models. *Journal of Climate*, 22, 1897–1919.
- Yasunaga, K. and Mapes, B.E. (2012a) Differences between more divergent and more rotational types of convectively coupled equatorial waves. Part I: Space–time spectral analyses. *Journal of the Atmospheric Sciences*, 69, 3–16.
- Yasunaga, K. and Mapes, B.E. (2012b) Differences between more divergent and more rotational types of convectively coupled equatorial waves. Part II: Composite analysis based on space–time filtering. *Journal of the Atmospheric Sciences*, 69, 17–34.
- Yu, X. and McPhaden, M.J. (1999) Seasonal variability in the equatorial Pacific. *Journal of Physical Oceanography*, 29, 925–947.
- Žagar, N. (2004) Assimilation of equatorial waves by line of sight wind observations. *Journal of the Atmospheric Sciences*, 61, 1877–1893.
- Žagar, N. (2017) A global perspective of the limits of prediction skill of NWP models. *Tellus A: Dynamic Meteorology and Oceanography*, 69, 1317573
- Žagar, N., Andersson, E. and Fisher, M. (2005a) Balanced tropical data assimilation based on a study of equatorial waves in ECMWF

- short-range forecast errors. *Quarterly Journal of the Royal Meteorological Society*, 131, 987–1011.
- Žagar, N., Andersson, E. and Fisher, M. (2005b) Balanced tropical data assimilation based on a study of equatorial waves in ECMWF short-range forecast errors. *Quarterly Journal of the Royal Meteorological Society*, 131, 987–1011.
- Žagar, N., Blaauw, M., Jesenko, B. and Magnusson, L. (2016) Diagnosing model performance in the Tropics. *ECMWF Newsletter*, 26–33.
- Žagar, N., Gustafsson, N. and Källén, E. (2004) Dynamical response of equatorial waves in four-dimensional variational data assimilation. *Tellus*, 56A, 29–46.
- Žagar, N., Kasahara, A., Terasaki, K., Tribbia, J. and Tanaka, H. (2015) Normal-mode function representation of global 3-D data sets: Open-access software for the atmospheric research community. *Geoscientific Model Development*, 8, 1169–1195.
- Žagar, N., Lunkeit, F., Sielmann, F. and Xiao, W. (2022) Three-dimensional structure of the equatorial Kelvin wave: Vertical structure functions, equivalent depths, and frequency and wavenumber spectra. *Journal of Climate*, 35, 2209–2230.
- Žagar, N. and Tribbia, J. (Eds.) (2020) *Modal view of atmospheric variability: Applications of normal-mode function decomposition in weather and climate research*. Cham, Switzerland: Springer Nature.
- Žagar, N., Tribbia, J., Anderson, J.L. and Raeder, K. (2009a) Uncertainties of estimates of inertio-gravity energy in the atmosphere. Part I: Intercomparison of four analysis datasets. *Monthly Weather Review*, 137, 3837–3857. Corrigendum, *Monthly Weather Review*, 138, 2476–2477
- Žagar, N., Tribbia, J., Anderson, J.L. and Raeder, K. (2009b) Uncertainties of estimates of inertio-gravity energy in the atmosphere. Part II: Large-scale equatorial waves. *Monthly Weather Review*, 137, 3858–3873. Corrigendum, *Monthly Weather Review*, 138, 2476–2477
- Žagar, N., Tribbia, J., Anderson, J.L., Raeder, K. and Kleist, D.T. (2010) Diagnosis of systematic analysis increments by using normal modes. *Quarterly Journal of the Royal Meteorological Society*, 136, 61–76.
- Zaplotnik, Ž., Žagar, N. and Gustafsson, N. (2018) An intermediate-complexity model for four-dimensional variational data assimilation including moist processes. *Quarterly Journal of the Royal Meteorological Society*, 144, 1772–1787.
- Zhang, C. (2013) Madden–Julian Oscillation: Bridging weather and climate. *Bulletin of the American Meteorological Society*, 94, 1849–1870.
- Zhang, C., Adames, Á.F., Khouider, B., Wang, B. and Yang, D. (2020) Four theories of the Madden–Julian Oscillation. *Reviews of Geophysics*, 58(3), e2019RG000685. <https://doi.org/10.1029/2019RG000685>
- Zhang, C. and Webster, P.J. (1989) Effects of zonal flows on equatorially trapped waves. *Journal of the Atmospheric Sciences*, 46, 3632–3652.

**How to cite this article:** Knippertz, P., Gehne, M., Kiladis, G.N., Kikuchi, K., Rasheeda Satheesh, A., Roundy, P.E. *et al.* (2022) The intricacies of identifying equatorial waves. *Quarterly Journal of the Royal Meteorological Society*, 148(747), 2814–2852. Available from: <https://doi.org/10.1002/qj.4338>